SINGLE ECHO ACQUISITION MAGNETIC RESONANCE IMAGING

A Dissertation

by

MARY PRESTON MCDOUGALL

Submitted to the Office of Graduate Studies of
Texas A&M University
in partial fulfillment of the requirements for the degree of

DOCTOR OF PHILOSOPHY

December 2004

Major Subject: Electrical Engineering

SINGLE ECHO ACQUISITION MAGNETIC RESONANCE IMAGING

A Dissertation

by

MARY PRESTON MCDOUGALL

Submitted to Texas A&M University
in partial fulfillment of the requirements
for the degree of

DOCTOR OF PHILOSOPHY

Approved as to style and content by:

_____
Steven M. Wright
(Chair of Committee)

_____   _____
Robert Nevels   Lihong Wang
(Member)   (Member)

_____   _____
Jay Humphrey   Chanan Singh
(Member)   (Head of Department)

December 2004

Major Subject: Electrical Engineering

ABSTRACT

Single Echo Acquisition Magnetic Resonance Imaging. (December 2004)

Mary Preston McDougall, B.S., Texas A&M University;

M.S.E., Johns Hopkins University

Chair of Advisory Committee: Dr. Steven Wright

The dramatic improvement in magnetic resonance imaging (MRI) scan time over the past fifteen years through gradient-based methods that sample k-space more efficiently and quickly cannot be sustained, as thresholds regarding hardware and safety limitations are already being approached. Parallel imaging methods (using multiple receiver coils to partially encode k-space) have offered some relief in the efforts and are rapidly becoming the focus of current endeavors to decrease scan time. Ideally, for some applications, phase encoding would be eliminated completely, replaced with array coil encoding instead, and the entire image formed in a single echo.

The primary objective of this work was to explore that acceleration limit – to implement and investigate the methodology of single echo acquisition magnetic resonance imaging (SEA MRI). The initial evaluation of promising array coil designs is described, based on parameters determined by the ability to enable the imaging method. The analyses of field patterns, decoupling, and signal-to-noise ratio (SNR) that led to the final 64-channel array coil design are presented, and the fabrication and testing of coils designed for 4.7T and 1.5T are described. A detailed description of the obtainment of the first SEA images – $64 \times N_{readout}$ images, acquired in a single echo – is provided with an evaluation of those images and highly accelerated images (through parallel imaging techniques) based on SNR and artifact power. Finally, the development of methodologies for various MR applications is described: applications that would particularly benefit from the speed of the imaging method, or those to which the method or the tool (array coil) lends itself. These applications include, but are not limited to, 3D imaging (phase encode in the slice select direction), resolution-enhanced imaging, large-scale (field-of-view) microscopy, and conformal surface imaging. Finally, using the primary enablement of the method – the ability to obtain complete MR images at speeds limited only by the time it takes to acquire a single echo – is presented with a discussion of extremely high frame rate imaging.

The contribution to the field of medical imaging is the first implementation, characterization, and demonstration of applications for the acquisition of MR images in a single echo.

Throughout this process, these efforts have been made with those in mind who might one day benefit from them.

ACKNOWLEDGMENTS

Waiting until the work was complete in the hope for inspiration for this brief statement has not been a successful tactic. While not overvaluing the importance of being mentioned on this page, I do hope sincerely that everyone who reads it understands that so many unnamed people have contributed in one way or another by aiding with the work itself, by entertaining children in the process of it, by helping me to gain and/or keep perspective during it, and by prayers and thoughts of which I am not aware.

I acknowledge Jeff, who handled fatherhood becoming more intense and husband-hood becoming less fun with grace. Thanks for always being a supporter of big ideas, true companion. To my wonderful children, Clare, Katherine, Will, David, and John: no matter how long the day had been, you always had a huge hug that came with an equally sized dose of perspective. Mom and Dad, you have given me countless opportunities, a strong work ethic, and a strong faith. You taught all four of us to evaluate situations with our conscience and heart as well as our mind, and you gave us a love of fun. You are, without a doubt, the best parents a girl could have. Irene, Liz, and Pete, you have all contributed in ways you know and in ways you can't know. Thanks for all the company, laughs, and love. To all my Many folks, and especially Papa, our weekends there are magic. I am so lucky to have a place like that and people like you in my and my kids' lives. Nancy and Mike, your son makes a good partner. Thank you for all your support in so many ways over the years. To all our family, not all of whom I could name, I thank you for all you have given us – fun memories for our children and lots of love. I also acknowledge – with a raised glass – all dear friends who find it possible to make even the middle of the week fun.

Thanks to my lab-mates and committee members, some of whom have given valuable input for nearly a decade, and thanks especially to my advisor, Dr. Steve Wright. You have never let me succumb to doubts, offering instead a project full of excitement and leaps across boundaries. Here's to many years of collaboration, working for the "betterment of humankind."

TABLE OF CONTENTS

ix

LIST OF TABLES

TABLE   Page

3.1   Comparison of Field Sensitivity Pattern Widths of a Loop and Planar Pair
      Element 18

3.2   Compilation of Capacitance and Microstrip Line Data for Various Substrates 20

3.3   Measured S-Parameter Data for 16-Channel Planar Pair Array 31

3.4   Measured Coupling Data for 1.5T Planar Pair Array With Various Decoupling
      Implementations 34

5.1   Summary of Signal Loss at Different Slice Offsets Due to Compromise Choice of
      Compensation Gradient 63

5.2   Modeled Leg Currents on the Three Legs of a Planar Pair at 200MHz 68

5.3   Modeled Leg Currents on the Three Legs of a Planar Pair at 2MHz 70

LIST OF FIGURES

CHAPTER I

INTRODUCTION

The capability that came with x-ray technology to see inside the body non-invasively was possibly one of the most important turning points in modern medicine. Magnetic resonance imaging (MRI) is the most complex and arguably the most revealing of the current imaging modalities, and, in turn, one of the slowest and most expensive. The dramatic rate of improvement in scan time over the past 15 years due to fast pulse sequences (gradient-based methods to sample k-space more efficiently and quickly) cannot be sustained, as thresholds regarding hardware and safety limitations are already being approached. Partially parallel imaging methods (using multiple receiver coils to partially encode k-space) have offered some relief in the efforts and, now that multiple receivers are common on most clinical scanners, are rapidly becoming the focus of current endeavors to decrease scan time. This work is dedicated to the exploration of a new fast imaging method – completely parallel MRI – primarily in an effort to offer the powerful imaging modality to new applications, but also to strengthen its possibilities in those it already serves.

I.1 Fast MR Imaging and Current Limitations

For many years, the unique capabilities of MRI as a medical imaging tool were limited by the uncomfortable and costly length of time necessary to acquire an image. Initial efforts to decrease scan time focused primarily on developing methods to sample k-space in the most efficient manner. Sequences such FLASH, EPI and Spiral scanning have significantly improved the acquisition efficiency to the point where physiology, as well as anatomy, is now accessible to scrutiny by MRI (1). Thus the clinical role of the modality has exploded to include "ultra-fast" MRI, "dynamic" MRI, and "real-time" MRI applications. Broadly categorized, fast MR imaging has allowed for the observation of diagnostic processes such as dynamic contrast enhancement (DCE) agent uptake for oncological studies, joint motion and other non-periodic activity, cardiac imaging without the artifacts caused by gating, MR-guided surgeries, catheter tracking and stent placement, and, when scan times reached the tenth of a second range, even neural activity (2-16).

This dissertation follows the style and format of *Magnetic Resonance in Medicine*.

Real-time MR imaging to rival the user interaction that ultrasound imaging allows is a largely discussed research topic, surfacing in many areas including hardware, image reconstruction, parallel imaging, and vascular interventions (17). The effectiveness of fast pulse sequences has, to a large extent, followed the development of the gradient hardware capabilities, as this directly controls the speed at which k-space can be traversed for any given sequence. At this point, however, it has become widely accepted that further advances in detection limits in MRI by improvements in rates of k-space traversal are going to be extremely costly in terms of hardware design (18).

In addition, image quality is oftentimes sacrificed for speed in fast imaging sequences. The most common considerations/complaints mentioned are the reduced SNR associated with low flip angle and single shot images, the blurring due to T2 decay in single shot images, and the loss of inherent tissue contrast, and even distorted contrast, due to short TR sequences (19-22). Another difficulty arises in the fact that many fast imaging sequences rely on acquiring as few as 50% phase encoding steps and interleaving updated k-space data with existing k-space data or reconstructing based on symmetry arguments. While this significantly shortens imaging time, it increases processing time, reduces SNR by a square root of two, increases the risk of blurring, and incurs the inherent risks due to phase errors (23,24).

The greatest limiting factors of gradient-based methods simply relate to human safety. Most of the factors benefiting fast MR imaging are in turn unfavorable to specific absorption rate (SAR) limitations. Since SAR relates to the energy deposited in tissue, high field strengths, a high gradient duty cycle, and multiple RF pulses applied quickly in succession are undesirable and are all characteristic of fast imaging (25). There is rapidly growing interest in using dynamic MRI to perform MR guided interventional procedures, including guided biopsies, monitoring of thermal ablations, radiation seed placement, and guiding and monitoring balloon angioplasty and stent placement. Conventional dynamic MR sequences, however, result in dangerously-high localized heating with the in-vivo placement of long conductive wires and electric components within a field of rapidly varying magnetic and electric fields. Previous work has confirmed substantial heating with straight copper wires, tracking catheters, and guidewires in place (11,26-28). Additionally, more rapid traversal of k-space can lead to peripheral nerve stimulation, particularly a problem in whole-body MRI (29-32). By the late 1990's, fast gradient based imaging techniques were rapidly approaching the FDA imposed safety limits, and parallel imaging methods that had been introduced in the late eighties began to be investigated with renewed interest.

I.2 Parallel Imaging with RF Coil Arrays

One could say that the phased array began to be seriously regarded in the world of NMR after P.B. Roemer published "The NMR Phased Array" in 1990. The thirty-four page work presented the array and its associated issues with the primary benefit being understood to be the ability to image a large field-of-view with the higher signal-to-noise-ratio and resolution available from a small surface coil (33); however, an equally, if not more, important capability of using multiple receiver coils had already been under scrutiny for several years – the ability to reduce scan time through the parallel or partially parallel acquisition of k-space data. The time-consuming aspect of the Fourier-based MR imaging is the number of phase encoding steps necessary to acquire to fully characterize k-space. It can be intuitively expected that adding multiple, well-characterized, independent (decoupled) receiver coils can add information about the spatial localization of the NMR signal received, and therefore eliminate or reduce phase encoding steps. The implementations of this can, as expected, be carried out in the image domain or in the k-space domain. Both methodologies were examined when the idea of using multiple coils was formally introduced in 1987 nearly simultaneously by J.W. Carlson and by Hutchinson and Raff (34,35). The introduction from Hutchinson and Raff was completely theoretical, taking an intuitive, but [thus far] least practical form of the problem: eliminate phase encoding entirely and acquire an $NxN_{readout}$ full image in one echo by placing N closely spaced, small receive coils around the sample. This "inverse source" problem in the image domain was further described by Kwiat et al. in 1990 (36), but already the problem was being viewed from similar, but more reasonable approaches, in which phase encoding was not eliminated, but reduced. In 1989, Kelton, Magin, and Wright introduced the concept of "sub-encoding and reconstruction" (37), to be followed in more detail by Ra and Rim in a 1994 publication describing the acquisition of an aliased image and the subsequent "unwrapping" of the data in the image domain with a description of the sensitivity matrix of the coils (38). The method almost precisely describes the imaging technique called SENSitivity Encoding (SENSE) introduced in 1999 by Pruessman et al. (39). Partially parallel Imaging with Localized Sensitivities (PILS) and others were introduced in 2000 as other image domain reconstruction techniques in which it is not necessary to characterize coil sensitivity beyond the FOV width and center (40). Using this knowledge, then, the reconstruction of the image can be restricted to the pertinent region of the image, reduced phase encoded k-space can be acquired, and aliasing will not occur. Another method to reconstruct from reduced phase encode acquisition is within the raw k-space data prior to the 2D-FFT and was first explored briefly in Carlson's 1987 communication, but fully by Carlson

and Minemura in 1993 (41). These methods include the popular SiMultaneous Acquisition of Spatial Harmonics (SMASH) introduced in 1997 and Sensitivity PRofiles from an Array of Coils for Encoding and Reconstruction In Parallel (SPACE RIP) introduced in 2000 (42,43). These techniques reconstruct the missing phase encode lines from the reduced number of acquired lines and coil sensitivity information, and then perform standard 2D-FFT image reconstruction.

Currently, factors of image acceleration of two to four are common clinically, and as manufacturers make systems with more receivers available, that number will continue to rise. The clear area of interest is the unexplored (one dimensional) limit: eliminate gradient switching and perform completely parallel MRI, with an $NxN_{readout}$ image obtained in a single echo using N well decoupled coils, each responsible for a strip of information directly above it.

I.3 Dissertation Objective and Organization

The primary objective of this work is to explore that limit – to implement and investigate the methodology of what has been termed Single Echo Acquisition Magnetic Resonance Imaging (SEA MRI). Four specific aims were outlined to obtain the objective:

Aim 1: Build prototype 64 channel RF coil arrays for 4.7T and 1.5T.

Aim 2: Demonstrate Single Echo Acquisition Magnetic Resonance Imaging.

Aim 3: Characterize the performance of 64 element array coils for single echo imaging.

Aim 4: Explore alternative array configurations and applications for single echo imaging.

Following an introduction to the subject matter, the aims translate clearly into chapter divisions. Chapter I of this dissertation has introduced this research with a brief description of the significance of fast MR imaging in the medical world and how it is limited in its current gradient-based implementations. A description of the progression of (partially) parallel imaging techniques to decrease scan time led to the objective of this dissertation: to explore a new dynamic MR imaging technique which can be characterized as completely parallel MRI. A description of the organization of this work now follows.

Chapter II provides the necessary technical background regarding the MR experiment, an explanation and discussion of k-space and parallel imaging theory, and a starting point for this work. The three chapters following document the completion of the aims outlined above.

Chapter III discusses the fulfillment of the first aim, the array coil design for single echo acquisition imaging. The evaluation and selection of an appropriate element design based on quasi-static modeling is discussed, followed by a description of the construction of prototype arrays for 4.7T and 1.5T, including decoupling procedures. Measurements of coil decoupling,

penetration depth and signal-to-noise ratio (SNR), and field patterns are included to characterize the array elements from an electromagnetic point of view.

Chapter IV very broadly covers the implementation of Single Echo Acquisition (SEA) imaging, subsuming the second and the third aims listed above. The use of the array coil to perform unprecedented rates of acceleration in MR imaging is described, including the establishment of appropriate nomenclature for such acceleration factors. The acquisition of the first Single Echo Acquisition images, obtained in one echo with no phase-encoding repetitions, is discussed in-depth, including the modeling that was necessary to understand, predict, and implement the phase compensation pulse that it was found must be used in the SEA pulse sequence. The SNR and artifact power of SEA images as well as highly accelerated (using partially parallel imaging techniques) is reported and discussed.

Chapter V completes the bulk of the dissertation in fulfillment of aim four above, describing methodologies for selected applications particularly suited to benefit from SEA imaging and the SEA array coil. The two main areas that limit the applications of SEA imaging are first discussed: the penetration depth and the resolution. The considerations when SEA imaging at increasing depths, specifically those regarding compensation gradient strength and artifact avoidance, are described in conjunction with resolution enhancement techniques that lend themselves well to the method. Preliminary studies are presented regarding the implementation of one of the more promising dedicated applications for the SEA array coil, large-scale field-of-view (FOV) microscopy. The methodology for SEA imaging of non-planar surfaces by conforming a flexible array is examined, and finally, the simple, unapproachable speed of the MR imaging technique is discussed and demonstrated by performing SEA imaging at 125 frames/second.

Chapter VI briefly recapitulates the contribution and spirit of the work and describes possibilities for future work in array coil design and in single echo acquisition imaging.

CHAPTER II

BACKGROUND

Since its inception in 1972 (44), magnetic resonance imaging (MRI) has gradually become a powerful clinical tool, offering high-resolution anatomical and physiological information oftentimes unavailable through any other imaging modality. The history of MRI, the physics involved, and detailed descriptions and derivations of the MR signal and the pulse sequences used to control it for various applications are readily available in many books and articles (45-49). In order to contextualize the significance of this work, however, it is necessary only to briefly introduce MR physics, the source of the MR signal, and gradient encoding – the time consuming portion of the imaging modality. It is then understandable how parallel imaging techniques contribute to a decrease in scanning time and how this work found it possible to reduce imaging time by an order of magnitude.

II.1 The MR Signal, Gradient Encoding, and K-Space

The frequency of interest in a nuclear magnetic resonance (NMR) experiment is related to the strength of the static magnetic field by the Larmor equation:

$$f = \frac{\gamma B_0}{2\pi} \qquad \text{or, alternatively} \qquad \omega = \gamma B_0 \qquad [2.1]$$

where B_0 is the static magnetic field, assumed to be z directed, and γ is the gyromagnetic ratio, or Larmor ratio. While it is possible to detect an NMR signal from approximately two-thirds of all stable nuclei (those with an odd number of protons, neutrons, or both), the hydrogen proton is primarily used in MRI because of its abundance in the soft tissues of the human body. The gyromagnetic ratio for the hydrogen nucleus is $2\pi \cdot 42.5759$ radians/tesla, putting, for example, standard 1.5T clinical scanners at a frequency of 63.85MHz and the 4.7T scanner in the Magnetic Resonance Systems Lab (MRSL) at 200.237MHz. A receive coil, then, detects a bulk NMR signal at the Larmor frequency from the sample. The "I" in MRI was made possible by Lauterbur's groundbreaking work published in *Nature*, which dealt with the spatial localization of that signal using magnetic field gradients (G_x, G_y, and G_z) and a backprojection technique similar to CT. In 1975, Richard Ernst proposed the use of gradients for the phase and frequency encoding technique that is now used and in 1980, Edelstein and coworkers implemented the technique (50,51). A simple and common gradient-echo sequence is shown in Figure 2.1. It
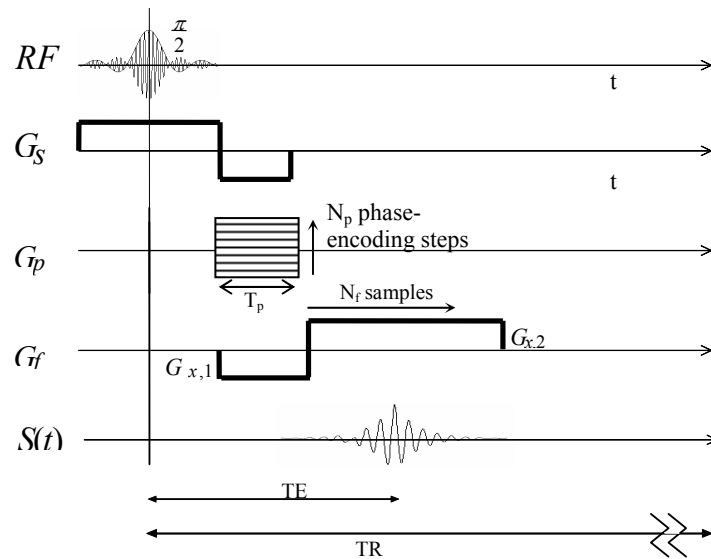
Fig 2.1 A common gradient echo pulse sequence for MR imaging showing the use of a frequency encoding gradient, G_f, and a phase encoding gradient table, G_p. In order to form an $N_p x N_f$ image, the echo is sampled N_f times while G_f is on and the entire MR experiment must be repeated N_p times, once for each gradient strength in the phase encoding table.

depicts the standard method to create an $N_p x N_f$ pixel image: The RF pulse excites the spins at the appropriate Larmor frequency, "tipping" them 90 degrees. During the excitation, a gradient in the z-direction, G_s ("slice-select" gradient), is turned on in order to select a desired slice location and thickness along z. A phase encoding gradient, G_p, is pulsed for a time, T_p, imparting a phase across the sample in order to provide one out of N_p "views" of the sample. Simultaneously, the spins are dephased using the frequency encoding gradient, G_f, and while the echo is "read-out" by sampling N_f times, G_f is turned on to put a spatially dependent frequency distribution across the sample. The echo peaks at TE (echo time) and the entire experiment is repeated N_p times, once for each phase encoding line. The time to acquire one phase encoding line is denoted by TR (repetition time), so the total imaging time is $N_p \cdot TR$. The critical path towards reducing imaging time, then, is to reduce N_p – the objective of parallel imaging techniques later described.

The expression for the signal received, *S(t)*, contains the desired image information modulated by the frequency and phase information crucial to the spatial localization of the signal. The image information contained in the received signal is a function of the field patterns of the transmit and receive coils, the relaxation times of the sample, and the available transverse magnetization. For convenience, this is denoted by *I(x,y)* , where *I(x,y)* is the image – the signal obtained from the object in the selected plane. Assuming that frequency encoding occurs along

the x axis and phase encoding along the y, the frequency of the signal received from a given x location can be expressed to include the frequency encoding gradient as follows:

$$\omega(x) = \gamma(B_0 + G_x x) = \omega_0 + \gamma G_x x \qquad [2.2]$$

The phase imparted during the duration of the phase-encoding gradient is

$$\phi(y) = \gamma G_y T_p y \qquad [2.3]$$

The signal, then, can be expressed in the following notation:

$$S(t) = \iint_{slice} I(x,y) e^{+j(\omega_0 t + \gamma G_x x t - \omega_{mix} t + \gamma G_y T_p y)} dx dy \qquad [2.4]$$

The expression can be simplified to become a familiar 2D-Fourier transform of the image information in a few steps: In the process of demodulation the mixing frequency $\omega_{mix} = \omega_0$. Secondly, the concept of "k-space" is introduced in which

$$k_x = \gamma G_x t \quad \text{and} \quad k_y = \gamma G_y T_p \qquad [2.5]\ [2.6]$$

It is worth noting that t is equivalent to the frequency encoding time denoted t_f in Figure 2.1. The signal expression then becomes

$$S(k_x, k_y) = \iint_{slice} I(x,y) e^{+jk_x x} e^{+jk_y y} dx dy \qquad [2.7]$$

From this expression, it is readily apparent that each line acquired fills one line in the 2D-Fourier transform of the object and that the image, $I(x,y)$ can be obtained by inverse Fourier transform after suitably sampling k-space. In a more graphical description, Figure 2.2 below shows a full
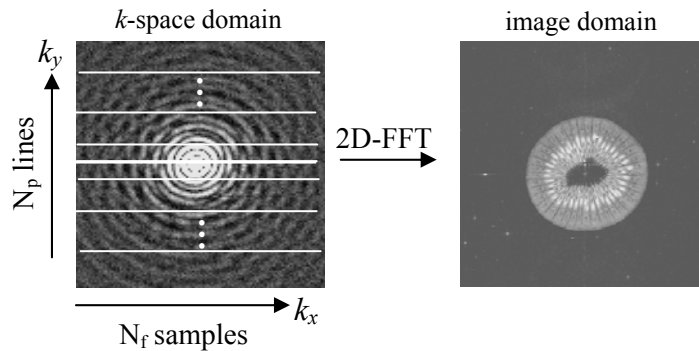
Fig 2.2 A full k-space data set and the resulting image after the 2D-Fourier transform. N_f samples of the echo (signal) are collected in the frequency encoding direction during each of the N_p repetitions of the experiment necessary to "fill" k-space. As expected, the majority of k-space data is low frequency, gathered in the center – the "bulk" image data. The edges of k-space contain high-frequency resolution information.

k-space data set for a slice of kiwi and the resulting image.

II.2 Parallel Imaging

Initial efforts to decrease scan time focused almost exclusively on the faster traversal of *k*-space using stronger gradients and faster rise times on the pulses. As was discussed in the previous chapter, hardware limitations and bioeffects have together slowed further growth in that direction. Partially parallel imaging techniques, often shortened to the less accurate "parallel imaging" (pMRI), have provided the largest gain in imaging speed since then and continue to be a growing area of research. As mentioned above, the imaging time necessary to fully acquire *k*-space is N_p*TR, where N_p is the number of phase encoding steps and TR is the repetition time. Parallel imaging techniques decrease the imaging time by using arrays of multiple coils and reducing the number of phase encoding lines acquired. This undersamples *k*-space in the phase encoding direction and causes aliasing in the resulting image when the *k*-space data is Fourier transformed, as Figure 2.3 depicts.
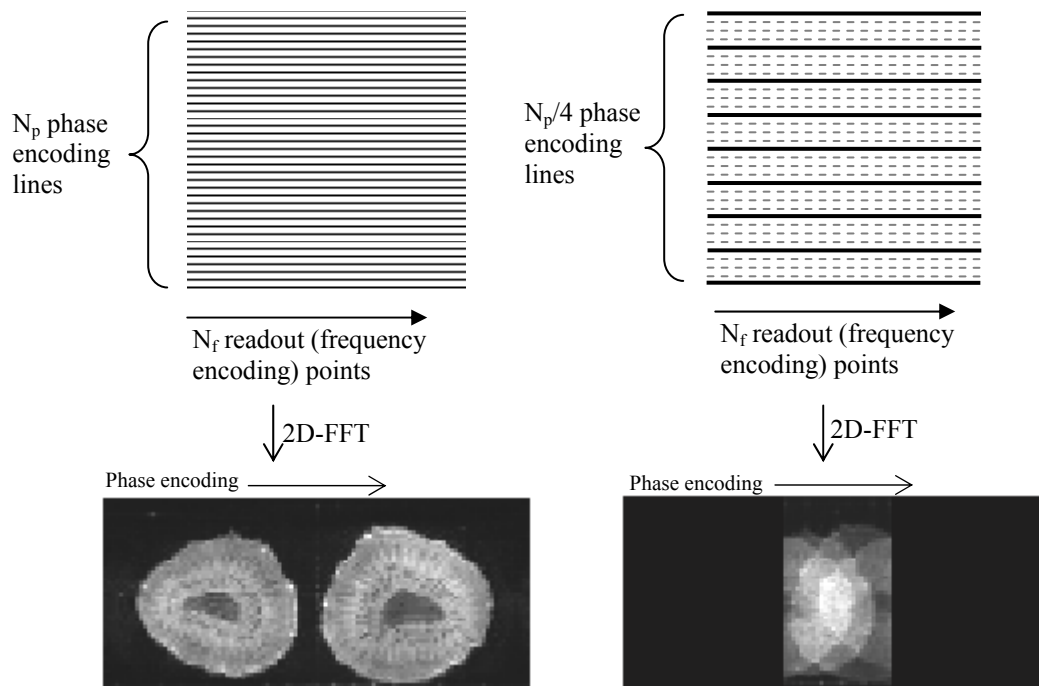
Fig 2.3 Graphical depiction of fully acquired *k*-space data set and resulting image (left) and *k*-space data set undersampled by a factor of four and the resulting aliased image (right). While undersampling decreases imaging time, information is lost, resulting in aliasing.

The aliasing is caused by the loss of information due to the undersampling of k-space. In essence, too few independent "views" of the object have been obtained. Parallel imaging uses the information provided by the unique sensitivity patterns of an array of coils to replace the lost information. Each coil provides a new "view" of the object. In principle, then, using an N_c element coil array can compensate for a factor of N_c decrease in the number of phase encoding lines.

The reconstruction of a full image can, as expected, be implemented in the *k*-space domain (synthesizing the skipped *k*-space lines) or in the image domain (unfolding the aliased image). References for each of these approaches are found in Chapter I. Brief discussions of the two methodologies are below.

II.2.1 K-Space Reconstruction

It is apparent from the signal equation (Eqn. 2.7) that each *k*-space line basically imposes a phase ramp at a respective spatial frequency across the spins according to $e^{+j\Delta k_y y}$, where Δk_y is the incremental phase added between lines. Figure 2.4 below graphically depicts this. Therefore, skipped *k*-space lines can be synthesized by using the field sensitivity patterns of the elements in the array coil to emulate the phase ramp imparted with the phase encoding gradient. The process is described mathematically and graphically below.
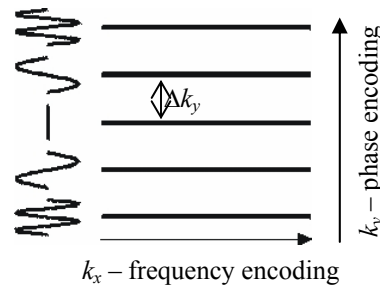
Fig. 2.4 Depiction of the modulation of the image data with each line of *k*-space collected. It is possible to synthesize skipped lines with array coil patterns.

If there are N_c coils in an array, each with a field sensitivity pattern, B_{1t}, the received signal can be written as a weighted (by w_n) sum of the signal from each coil:

$$S(k_x, k_y) = \sum_{n=1}^{n=N_c} w_n \iint_{slice} I(x,y) B_{1t,n}(x,y) e^{+jk_x x} e^{+jk_y y} dxdy \qquad [2.8]$$

Equivalently,

$$S(k_x, k_y) = \iint_{slice} I(x,y) \left\{ \sum_{n=1}^{n=N_c} w_n B_{1t,n}(x,y) \right\} e^{+jk_x x} e^{+jk_y y} dxdy \qquad [2.9]$$

The bracketed term containing a sum of the weighted coil patterns can then be used to synthesize a skipped k-space line, as Fig. 2.5 shows (52).
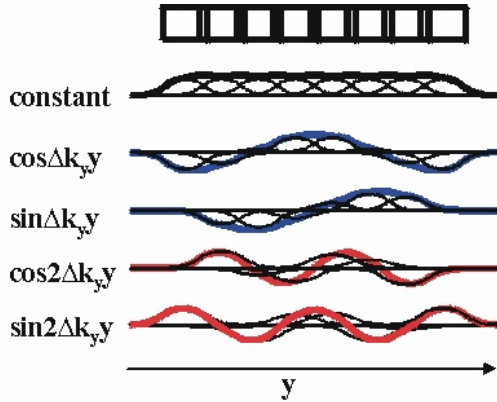
Fig 2.5   Summing the appropriately weighted field sensitivity patterns of an eight-coil array to synthesize the phase ramp of the omitted *k*-space lines.

II.2.2 Image Domain Reconstruction

The same *a-priori* knowledge of the coil patterns that allows for the synthesis of *k*-space lines is equally useful in the image domain to "unwrap" the aliased image obtained after undersampling. The clearest explanation of unwrapping in the image domain is with an example. Consider two independent coils receiving signals from two pixels, *a* and *b*. At pixel *a*, the image information is given by *I(a)* and the coil sensitivities from the two coils are $B_1(a)$ and $B_2(a)$. In a fully encoded image, the respective signal received in the two coils would be

$$S_1(a)=B_1(a)I(a) \qquad \text{and} \qquad S_2(a)=B_2(a)I(a) \qquad\qquad [2.10][2.11]$$

Similarly, at pixel *b*, the detected signals would be

$$S_1(b)=B_1(b)I(b) \qquad \text{and} \qquad S_2(b)=B_2(b)I(b) \qquad\qquad [2.12][2.13]$$

Now assume that we do a factor of two acceleration and that pixel *a* and pixel *b* overlap each other in the Fourier reconstructed images that we make from each coil. Now the signal received at each coil from the aliased pixel contains information from pixel *a* and from pixel *b*, but weighted differently from the coil sensitivities at their respective locations:

$$S_{1,aliased}(aliased\ pixel\ \text{-}\ a\ or\ b) = S_1(a) + S_1(b) = B_1(a)I(a) + B_1(b)I(b) \qquad\qquad [2.14]$$

$$S_{2,\ aliased}(aliased\ pixel\ \text{--}\ a\ or\ b) = S_2(a) + S_2(b) = B_2(a)I(a) + B_2(b)I(b) \qquad\qquad [2.15]$$

In matrix form, from above equations 2.14 and 2.15

$$\begin{bmatrix} S_{1,\,aliased} \\ S_{2,\,aliased} \end{bmatrix} = \begin{bmatrix} B_1(a) & B_1(b) \\ B_2(a) & B_2(b) \end{bmatrix} \begin{bmatrix} I(a) \\ I(b) \end{bmatrix}$$

[2.16]

which makes it clear that the unaliased image information at each pixel can be obtained by inverting the coil sensitivity matrix and multiplying the received aliased signals by it.

$$\begin{bmatrix} I(a) \\ I(b) \end{bmatrix} = \begin{bmatrix} B_1(a) & B_1(b) \\ B_2(a) & B_2(b) \end{bmatrix}^{-1} \begin{bmatrix} S_{1,\,aliased} \\ S_{2,\,aliased} \end{bmatrix}$$

[2.17]

II.2.3 Notable Considerations: SNR and Decoupling

It is worth emphasizing that parallel imaging can only be accomplished if independent views of the sample are provided by the coils in the array. Otherwise, the synthesis of missing *k*-space lines is not possible and/or the unwrapping matrix is ill-conditioned and the inversion in unstable. The spatial localization of coils cannot replace the spatial localization provided by phase encoding lines unless each coil has a unique "view". Meeting this requirement becomes particularly challenging when taking parallel imaging to its limit by completely eliminating phase encoding with N_p coils, as this work discusses.

The reduction in imaging time made possible by using arrays comes at a price of course. Macovski published a work straightforwardly deriving that in an MR experiment, the signal-to-noise ratio (SNR) for a given object is proportional to the square root of the signal acquisition time (53). Since then, supporting work has been published specifically regarding the SNR of the parallel imaging experiment (39,54). When decreasing scan time by reducing the number of acquisitions, there is an unavoidable SNR penalty proportional to a square root of the acceleration factor.

It is notable that not all parallel imaging methods fall clearly into one approach or the other, and that significant work has been published generalizing parallel imaging reconstructions such that distinguishing between the two approaches, while the most intuitive viewpoint, is sometimes unnecessary (55-57).

CHAPTER III

ARRAY COIL DESIGN FOR SINGLE ECHO ACQUISITION IMAGING

Within the past several years, partially parallel MR imaging methods have moved into the clinic. Using arrays of four to eight coils, techniques such as SMASH and SENSE have made acceleration factors of two to four now common clinically, and research sites routinely exceed this. The number of coils used in arrays has tracked (and pushed) the number of receivers available. Sixteen channel head coil work was presented as early as 1998 and as recently as 2004 (58,59), and 32-channel surface coil work has recently been presented (17). Our group built a 64-channel prototype portable receiver to enable the use of 64-element arrays and potentially corresponding acceleration factors (60). The primary goal, however, was to investigate a new imaging technique in which an image ($64xN_f$ in this case) is acquired in a single echo using completely parallel MRI: phase encoding eliminated, replaced by the spatial localization of 64 long and very narrow coils. This requires a high degree of independence in the B_1 patterns of the array elements, a condition that is met parallel to and relatively near to the array (61), where Single Echo Acquisition (SEA) imaging has been implemented.

The nature of the intended use for the coils dictated a clear but non-standard set of design parameters where SNR, Q factor, penetration depth and other characteristics, while all desirable, were not the highest priorities or defining features. While decoupling array coils is always a significant issue, in this case it was of particular consequence due to the fact that space and expense considerations led to the use of standard, 50ohm chip preamplifiers (Agilent INA-01170 Low Noise MMIC Amplifier, noise figure 1.7 dB) instead of isolation preamplifiers (33,62). This consideration, combined with the large number of elements and the intention to use the array to completely perform the localization in the phase encoding direction, defined the crucial design characteristics: The complexity, size, and expense inherent to 64-channels needed to be minimized, and the elements needed to be long and narrow, parallel, closely-spaced, and decoupled with highly localized field patterns.

This chapter describes the construction and analysis of the first 64-channel array coils for MR imaging, built to enable SEA imaging. The following topics highlight the defining steps and their order of discussion:

- the choice of element design in the array
- the quasi-static model developed to analyze the coils
- preliminary array coil testing and material decisions

- the first prototype 64-channel array constructed for 4.7T

- the modified design from which the majority of data in this work was obtained

- the construction of a scaled 64-channel array for 1.5T clinical imaging

- evaluation of losses in the design

- quantification of the coupling of the arrays and necessary decoupling procedures

- measurement of field patterns and SNR vs. penetration depth for the coils

III.1 Element Design and Modeling

The two most reasonable designs for the array elements, considering the requirements, were a conventional loop and a planar pair (see Figure 3.1) (63).   The SNR of the two designs is generally considered comparable near the surface, hence the use of planar pairs in quadrature pair coils (64). The nature of SEA ensured that imaging would occur almost exclusively near the surface, thus the two designs were evaluated primarily based on their element-to-element coupling characteristics and coil sensitivity pattern localization.   Two programs were used to analyze the designs: to verify that the SNR was comparable between the two and to compare their field sensitivity pattern widths, a quasi-static program was written in Matlab to implement Biot-Savart Law using the assumed (ideal) currents labeled in Fig. 3.1. It is worth noting at this point that what is commonly called the "field" of a coil in the MR literature and is notated as "B" is actually a flux density. Conforming with common practice, B will typically be referred to as a field throughout this work. When the coil is turned "on end" – diagrammed in Fig. 3.2 – the field at a point can be expressed analytically by summing the fields from each of the three wires, given ideal current distribution and wire spacing.   Example calculations for the planar pair
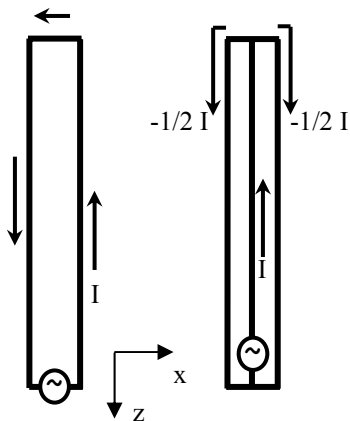
Fig. 3.1 Two coil designs considered for use as elements in the 64-channel array: a standard loop (left) and a planar pair (right). Coils are oriented with the long axis aligned with the static magnetic field (along z). Current distribution is as shown. The feed point is indicated by the voltage source. Axes are labeled for use in orienting field plots below.
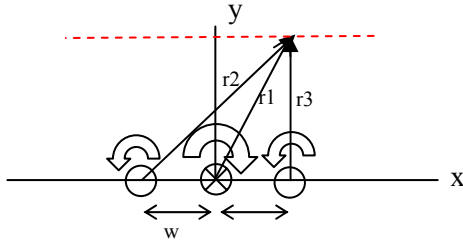
Fig. 3.2 "On end" view of planar pair design to visualize calculating the field across the coil. The field at any point (r,ϕ) is a sum of contributions from the three wires. Wire spacing and field directions are labeled.

design are shown below.

The Biot-Savart expression for a field at a point, *r*, due to a wire of length, *L*, carrying current, *I*, can be expressed as follows:

$$\vec{B}_{wire} = \frac{\mu_0 \cdot I \cdot L}{2\pi r \sqrt{L^2 + r^2}} \hat{a}_\phi \qquad [3.1]$$

In this case, *L>>r* and the expression simplifies to

$$\vec{B}_{wire} = \frac{\mu_0 \cdot I}{2\pi r} \hat{a}_\phi \qquad [3.2]$$

To simplify the application of the expression to the planar pair design, the currents on the respective wires are numbered such that $I_1 = I$ and $I_2 = I_3 = (-1/2)I$, and the cylindrical coordinate expressions for the *(r ,ϕ)* point under consideration are transformed to Cartesian coordinates. Figure 3.3 diagrams the variables in use and clarifies the transformation of the field to *x* and *y* components. Equation 3.3 is the expression for the fields of a planar pair (with distance *w* between wires) at a point *(x,y,z)* that can be easily integrated over a slice thickness, *y*, and observed as a function of *x* across the coil.
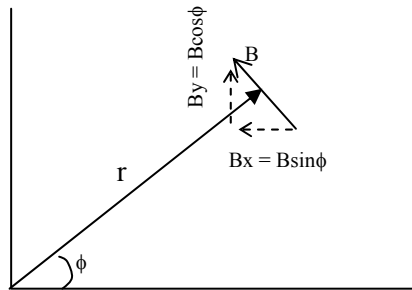
Fig. 3.3 Diagram clarifying the calculation of the field components at a point (r,ϕ).

$$B(x,y,z) = \frac{\mu_0 I}{2\pi}\left(\left(\frac{\sin\phi}{\sqrt{x^2+y^2+z^2}} - \frac{\frac{1}{2}\sin\phi_2}{\sqrt{(x+w)^2+y^2+z^2}} - \frac{\frac{1}{2}\sin\phi_3}{\sqrt{(x-w)^2+y^2+z^2}}\right)\hat{a}_x + \right.$$

$$\left.\left(\frac{\cos\phi}{\sqrt{x^2+y^2+z^2}} - \frac{\frac{1}{2}\cos\phi_2}{\sqrt{(x+w)^2+y^2+z^2}} - \frac{\frac{1}{2}\cos\phi_3}{\sqrt{(x-w)^2+y^2+z^2}}\right)\hat{a}_y\right)$$

[3.3]

where

x1=x
x2=x+w
x3=x-w

y1=y2=y3=y (infinitely thin coronal slice)
z1=z2=z3=z (infinitely thin axial slice)

$$\phi = \tan^{-1}\frac{y}{x}$$

$$\phi_2 = \tan^{-1}\frac{y}{x2} = \tan^{-1}\frac{y}{x+w}$$

$$\phi_3 = \tan^{-1}\frac{y}{x3} = \tan^{-1}\frac{y}{x-w}$$

For SNR calculations, the signal was taken to be proportional to the calculated fields and the noise was assumed to be white, proportional to the resistive losses of the respective coils, $\sqrt{R_{loop}}$ and $\sqrt{R_{planarpair}}$, where $R_{planar\ pair} = 0.75\ R_{loop}$ based on standard electromagnetic power dissipation arguments. To study the coupling characteristics of the two designs, including the capacitive characteristics between adjacent elements, a model was needed that included phase effects and electric field effects; therefore, a full-wave program previously developed in-house was used (65).

The relative field patterns, coupling characteristics, and signal-to-noise ratios of the two coils are compared in Fig. 3.4a-c. It is commonly accepted that the most useful region of sensitivity for a coil exists within approximately one coil width above it. The field sensitivity patterns shown in Fig. 3.4a were modeled at a height equal to a coil width above the coil, and at that height, the loop coil has a 38% broader pattern measured at the point where the field falls to half intensity. Calculations for additional heights are summarized in Table 3.1. For SEA imaging, where each coil is responsible for the strip of the final image directly above it, the broader pattern of the loop coil is undesirable. Figure 3.4b compares the element-to-element coupling between two loops and two planar-pairs as a function of separation distance. Coupling
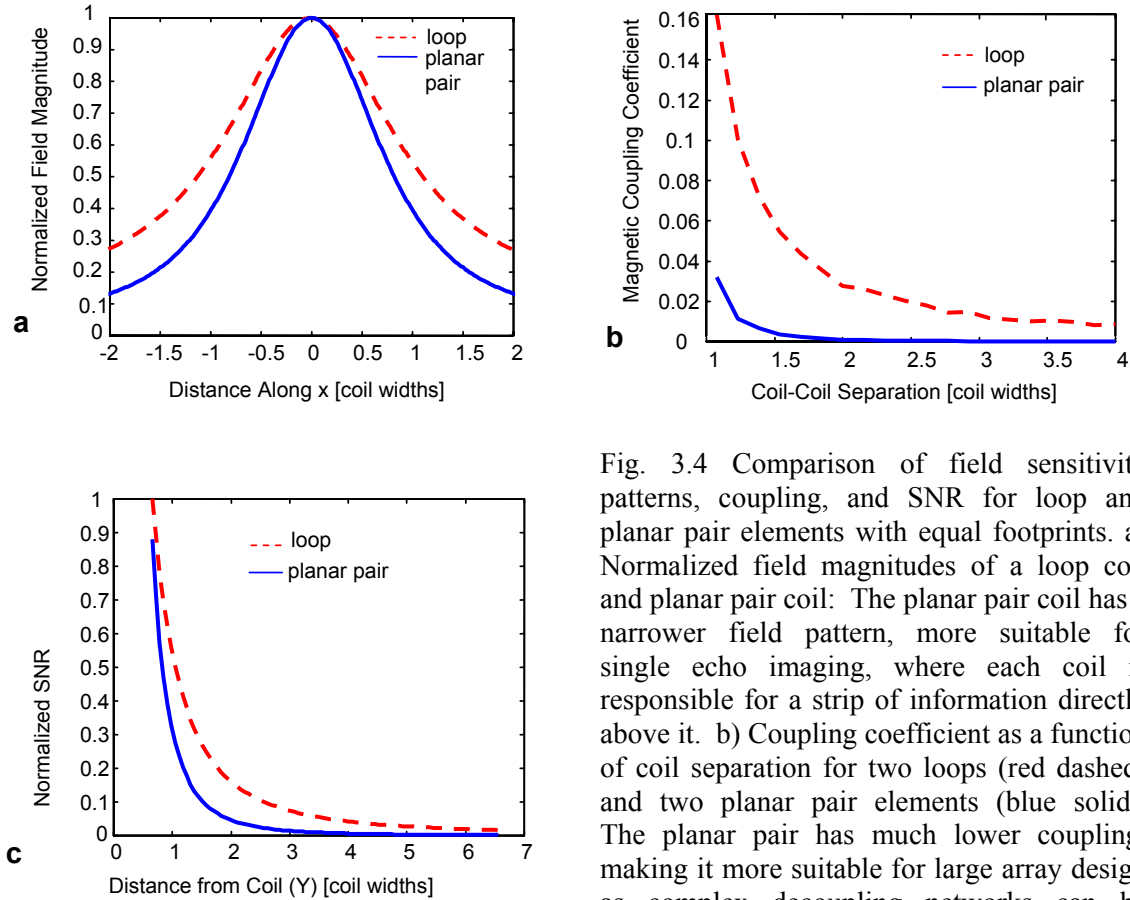
Fig. 3.4 Comparison of field sensitivity patterns, coupling, and SNR for loop and planar pair elements with equal footprints. a) Normalized field magnitudes of a loop coil and planar pair coil: The planar pair coil has a narrower field pattern, more suitable for single echo imaging, where each coil is responsible for a strip of information directly above it. b) Coupling coefficient as a function of coil separation for two loops (red dashed) and two planar pair elements (blue solid). The planar pair has much lower coupling, making it more suitable for large array design as complex decoupling networks can be avoided. c) SNR comparison between a loop and a planar pair as a function of distance from the coil (along the y-axis). While there is an SNR penalty when using planar pairs, the advantages mentioned in a) and b) outweigh it.

was quantified using the magnetic coupling coefficient as defined by Roemer (33). The loop coils exhibited far stronger coupling than the planar pair elements, with a coupling coefficient more than four times greater at a distance corresponding to the "nearest neighbor" separation. While it is possible to recover independence between field patterns in the presence of coupling (66), matching and tuning manipulations on coupled elements are very complex, requiring many iterations. For an array with 64 coils, the inherent decoupling of the planar pair was a critical design decision point.

Figure 3.4c shows the SNR of the two designs as a function of distance from the coil (equivalent to imaging depth). At a coil width away from the array, there is a 41% penalty associated with using the planar pair design. Avoiding the complexity of 64 decoupling

networks, being mindful of the need for the narrowest possible field pattern, and bearing in mind that the main overall goal was to make a tool to investigate a new imaging method made the planar pair design the clear choice for the *prototype* SEA array construction, knowing that the SNR benefits offered by the loop made it worth investigating in future work.

Table 3.1 Comparison of Field Sensitivity Pattern Widths of
a Loop and Planar Pair Element

HEIGHT ABOVE COIL [COIL WIDTHS]	LOOP FIELD PATTERN WIDTH, W_L [NORMALIZED TO *]	PLANAR PAIR FIELD PATTERN WIDTH, W_{PP} [NORMALIZED TO *]	PERCENT DIFFERENCE $\left. \left| W_{PP} - W_L \right| \middle/ W_{PP} \right. \times 100\%$
1	1.379	1*	37.9%
1.5	1.854	1.387	33.7%
2	2.372	1.788	32.7%
2.5	2.905	2.204	31.8%
3	3.453	2.628	31.3%

III.2 Array Construction

The progression toward the construction of the 64-channel array currently used for SEA imaging applications is documented in the following sections. Preliminary test designs, various efforts to match and tune, and the simple logistics of fitting 64 coils in the available space are briefly discussed., and the final coil design is described in some detail. Unless otherwise noted, the boards were all mechanically etched in the Magnetic Resonance Systems Lab (MRSL) using a C30 PC Board Prototyper (LPKF, Wilsonville OR) and all bench measurements were performed using an HP 4195A Network Analyzer.

III.2.1 Preliminary Array Coil Testing

    A four-channel test array of large planar pair elements (shown in Fig. 3.5) was initially constructed to test the basic ability to match, tune, and decouple the elements, as well as the localization of the field patterns. Everything performed suitably and the effort progressed to a 16-channel array, populated with lumped elements, the board layout of which is shown in Fig. 3.6. It was possible to address many initial questions at this point: Because the receive-only array had to fit inside the homogenous region of a transmit volume coil inside an 18-cm i.d.
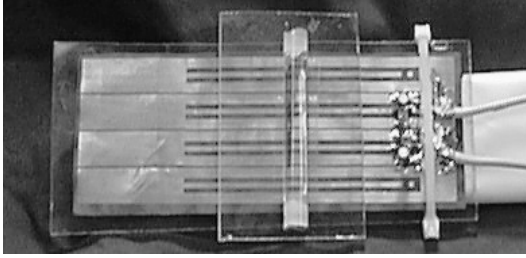
Fig. 3.5 A prototype four element planar pair array. Only the two center elements are matched and tuned. A test tube of water is placed across the coil for testing the localization of signals. Individual sensors are 10.5-mm wide by 64-mm long.

Accustar S-180 gradient coil, it was assumed that fitting lumped elements for the matching and tuning of 64 coils into the space would be prohibitive. It was anticipated that because the elements were all identical, the values required to match and tune them would be very similar and a simple fabrication technique involving printing small distributed capacitance pads could be possible. In addition, with no solder joints on the coil itself, potential applications requiring conforming the array were not eliminated. It was also anticipated that it would be necessary to run some length of 50Ω-microstrip line on the coil in order to connect the coils to transmission lines. Therefore, various substrates were investigated with regard to their ability to provide adequate capacitance with a small pad area and have a thin trace width for 50Ω lines. The results of the investigation are shown in Table 3.2. Rogers manufactures all of the substrates investigated unless otherwise noted.

To achieve distributed capacitance, efforts were made to use a "pressure fit" or an adhesive connection between the substrate and coils. These were initially unsuccessful because of an inability to achieve stable mechanical connections. Etching on dual sided thin substrates, such as the Pyralux, was not possible using the mechanical etching techniques of the LPKF, so
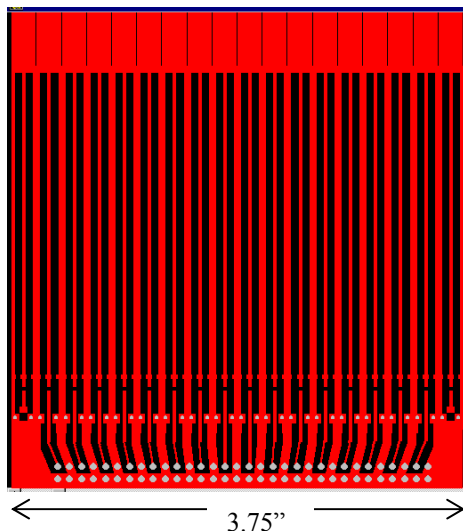
Fig. 3.6 Board layout for 16-element surface coil tuned with lumped elements developed for feasibility studies. Note the presence of two outer 'dummy' coil elements which remain unconnected. These elements force cause the input impedance of the 16 active elements to remain essentially the same for ease of tuning.

3.75"

Table 3.2 Compilation of Capacitance and Microstrip Line Data for Various Substrates

MATERIAL	ϵ_R	THICKNESS	OTHER AVAILABLE THICKNESSES	PAD SIZE FOR 10PF (MIL^2)	50Ω TRACE WIDTH
RT/duroid 6006	6.5	10mil	25,50,75,100	261 x 261	14mil
RT/duroid 6010	10.2	5mil	10,25,50,100	147x147	4.69
RT/duroid 6010	10.2	10mil	5,25,50,100	208x208	10
TMM4	4.5	15mil	20,25,30…	385x385	28
TMM6	6.0	15mil	20,25,30…	333x333	22
TMM10	9.2	15mil	20,25,30…	269x269	15
TMM10i	9.8	15mil	20,25,30…	260x260	14.6
RO3006	6.5	10mil	10,25,50	260x260	14
RO3010	10.2	10mil	25,50	208x208	9.3
RO3010	10.2	25mil	10,50	330x330	23
Dupont Pyralux	3.4	1mil		114x114	2.3

methods to enable chemical etching of fine traces on thin boards were investigated. Iron-on toner transfer systems did not reliably achieve smooth or very fine traces. Direct laser printing onto the copper did not deposit enough toner to mask the copper reliably. Several commercial sources were contacted for outsourcing the boards but these companies were unable to etch on such thin boards with such fine traces. Finally, the values of capacitance necessary to tune the coils were not as close between coils as expected, meaning that using distributed capacitance would involve a complex design that somehow allowed for "tuning" by increasing the pad size with a solder connection to optional nearby pad/pads. Thus, the possibility of using distributed capacitance on the 64-channel array was abandoned in favor of moving lumped tuning elements away from the coil by an integer multiple of a half wavelength of the operating frequency.

III.2.2 Prototype Version of 64-Channel Array Coil for 4.7T

The board layout for the "first version" 64-channel array is shown in Fig. 3.7. The overall array dimension was 13 x 8.1 cm, with each of the 64 coils having only a 2mm x 8.1 cm footprint. Ten-mil conductor traces formed the coils with 20-mil gaps between them and 10 mils between each element. The coils were etched on 10-mil thick RO3010, which has an ε_r of 10.2. The substrate was chosen because of its flexibility (again – potential for applications that require conforming the array) and so that the 10-mil coil conductor width matched the width of a 50Ω microstrip line.   The segment of microstrip transmission line served as a transition from the
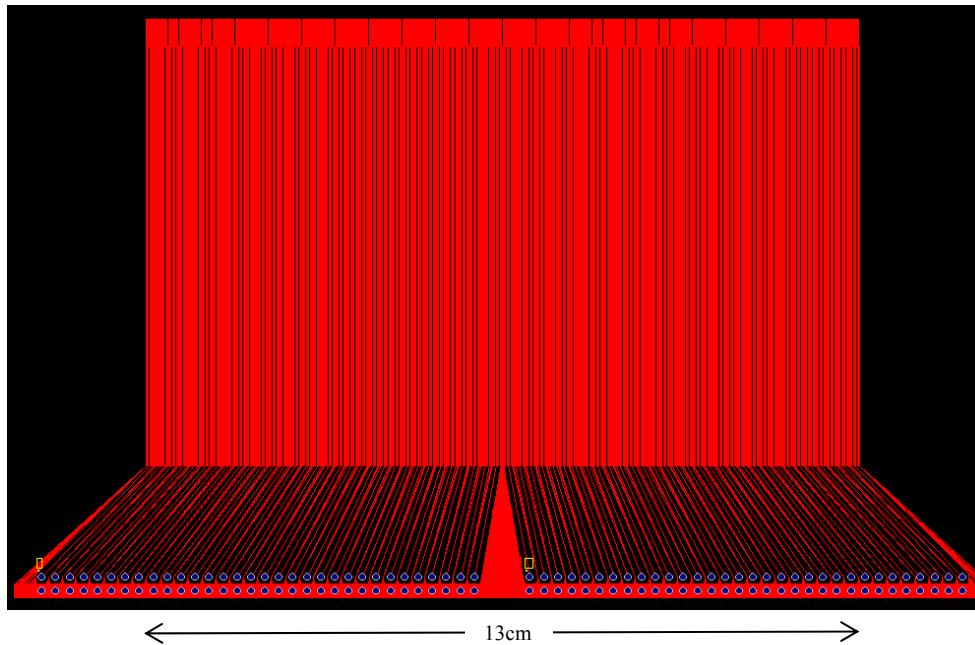
Fig. 3.7 Board layout for "first version" 64-channel array for 4.7T. The imaging portion of the array is connected to the two 32-channel Gore connectors by 50Ω microstrip transmission line trace widths (10mil traces on 10-mil thick RO3010).

array elements to the connection point for 32-channel near-coax performance ribbon cable from W.L. Gore (Newark, DE) that carried the signals out of the bore of the magnet.

A block diagram of the system – array plus matching components and tuning components – is shown on the following page in Fig. 3.8. Moving the lumped matching and tuning elements N·λ/2 wavelengths away from the coil, as was discussed above, was limited by the lossy nature (0.3 dB/ft at 500MHz) of the ribbon cable being used. Therefore, the tuning point for the array (that which affects the quality factor, Q, of the coil discussed further in III.2.5) was placed only one half-wave away from the coil though the length of cable did not reach outside the bore (72cm). The relative dielectric constant of the Gore cable is 1.52, and a half-wave at 200.237MHz results in a 60-cm length of cable. When tested with capacitors, the same degree of control over the match and tune was exhibited as when the capacitors were on the coil itself. Instead of capacitors, dual common-cathode varactors diodes (varactors, MACOMM MA4ST230CK) in a standard SOT-23 package were used for tuning for several reasons: one, the planar pair elements needed to be tuned in a balanced configuration – the same changes in capacitance across each loop of the planar pair simultaneously; two, the tuning mechanism needed to be small, as it was still in the bore; three, the desire to be able to tune all 64
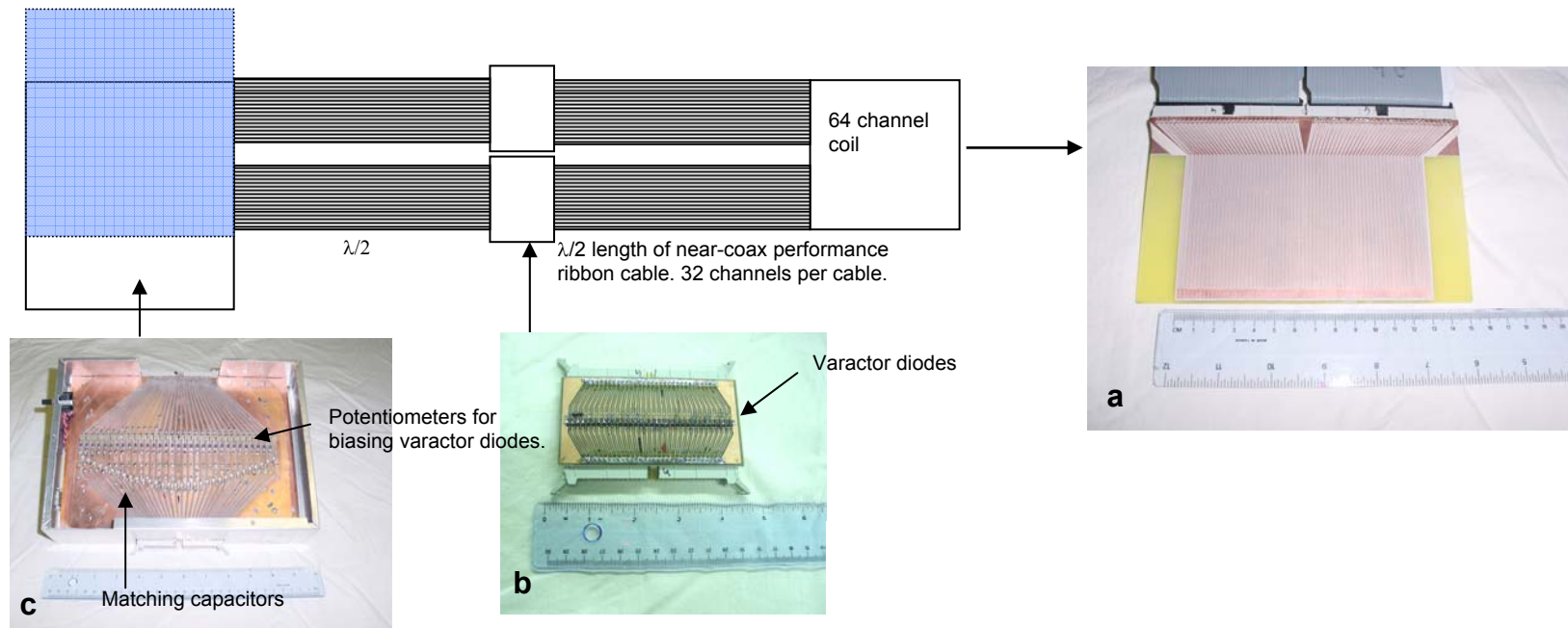
Fig. 3.8 Prototype 64-channel array coil system for 4.7T. a) 64-channel array coil for 4.7T, as described in text. b) "Tuning Board" located a half-wave away from the coil containing dual-sided varactor diodes. c) "Bias Box" containing potentiometers for individually controlling the bias voltage to each coil and variable matching capacitors.

simultaneously - in "bulk" – by controlling a central voltage source. Modeling confirmed that the .7-8pF range of the varactors was sufficient. The varactors' package was magnetic, but the fact that they were a half-wave from the coil fortuitously prevented the possibility of susceptibility artifacts.

The DC bias for the varactors was inserted over the RF lines, another half-wave away (outside the bore), with a potentiometer on each line to individually control the voltage for each coil. The matching capacitor was placed on the other side of the bias insertion (farther from the coil) so as not to act as a DC block. As can be seen in the photograph of the "bias box" in Fig. 3.8, the matching capacitors are "fanned" to compensate for differences in line length to that point. When the final system was complete, Q bench measurements (discussed further in III.2.5) showed a factor of three decrease from a coil that was matched and tuned with capacitors on the coil itself (67).

III.2.3 Operative Version of 64-Channel Array Coil for 4.7T

Time and use combined with coupling measurements (discussed in III.3) and images (discussed in IV.2) taken with the prototype array made two problems apparent. First, the Gore cable proved to be unwieldy coming out of the bore, exhibiting unpredictable behavior regarding signal strength when bent. Second, pick-up probes placed in the bias box indicated that there was significant coupling, presumably between the wound potentiometers in the bias box, as RF was on the line at that point. A modified version of the array was designed and constructed to eliminate the need to manipulate Gore cable coming out of the bore and to better isolate the DC and RF by eliminating the bias box and removing the RF from the potentiometers. In addition, it
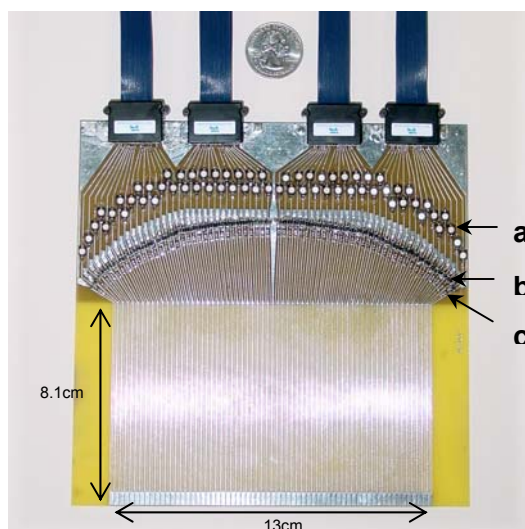
Fig. 3.9 64-channel array coil for Single Echo Acquisition (SEA) imaging at 4.7T. Individual planar pair element footprints are 2mmx8.1cm. Components on the coil include (a) 64 variable matching capacitors, with a 10kΩ resistor underneath, staggered due to space considerations, (b) 128 single-sided varactor diodes for tuning, and (c) 64 1000pF DC blocking capacitors.

was decided to sacrifice flexibility for an SNR increase and move the match and tune onto the coil. The modified array is pictured in Fig. 3.9 (68). The portion of the coil to be used for imaging was designed exactly as the prototype to have an overall coil dimension of 13 x 8.1 cm, yielding individual element footprints of only 2 mm (80 mil) x 8.1 cm. The conductor traces were 10 mils wide with 20-mil gaps between them and 10 mils between each coil. To realize as much space as possible for matching and tuning the 2-mm coils, the array fanned out to 16 cm, completely filling the transmit volume coil. This transition from the array elements and the matching and tuning networks were fabricated over a ground plane in an attempt to keep the active area of the array limited to the linear portion of the elements. The magnetic dual-sided varactors used to tune the prototype coil were replaced with two single-sided varactors (one for each loop) in a non-magnetic SOD-323 package (Infineon BB639). The decision to use varactors to tune was based on the same factors that influenced the decision to use them on the prototype design: the coil needed to be tuned in a balanced configuration across the paired loops; the tuning mechanism needed to be very small; the desire to be able to tune all 64 at least partially simultaneously - in "bulk". The varactors were biased over the RF lines by placing a $10k\Omega$ resistor under the matching capacitor, as there was not enough space to put it in parallel, preventing the matching capacitor from acting as a DC block. The two 32-channel Gore ribbon cables were replaced with four 1.5-m ultrasound cables, each containing twenty 50Ω coaxial lines (Precision Interconnect "Blue Ribbon", Wilsonville OR). The flexible cables connected the coil to two 32-channel "bias insertion boards" located outside the bore. The cables were pre-assembled with low-profile header connectors, and matching surface-mount receptacles (Samtec QSE/QTE series) were installed on the array and bias insertion boards. The bias insertion boards contained the DC block and conversion to the pre-amp lines and also connected to high

Blue Ribbon Cable:
20 50Ω lines per strip

"Bias-insertion" board:
DC Block and
conversion to preamp
line

Potentiometer Board
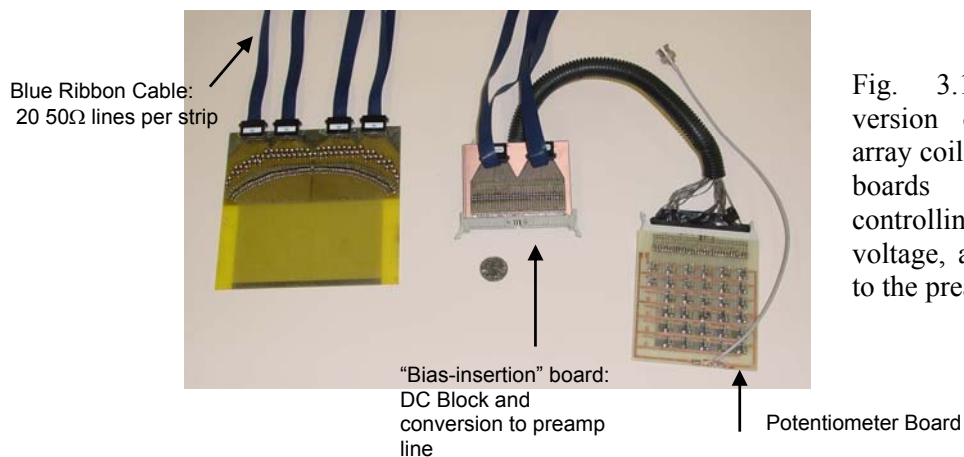
Fig. 3.10 Operative version of 64-channel array coil and associated boards for tuning, controlling the bias voltage, and connecting to the preamplifier.

2 x 32-channel potentiometer board for DC varactor bias with high resistance carbon wire connection.

2 x 32-channel preamplifier box

64-element array coil

4x20-channel ultrasound coaxial cables (Precision Interconnect, "Blue Ribbon") – Samtec connectors

2 x 32-channel "Bias Insertion" board

2 x 32-channel Gore near-coax ribbon cable

Calibration point 2: input to coils.

Calibration point 1: input to entire system.

Fig. 3.11 Layout of entire coil/preamplifier system, consisting of the coil, bias-insertion boards, preamplifers, and appropriate interconnections. The two calibration points used to evaluate coupling mechanisms are labeled for future discussion in III.3.

resistance carbon wire lines (to stop the RF signal) leading to the potentiometer boards that were used for individually controlling the bias voltages. The layout of the entire system is pictured in Fig. 3.10 and for clarity is diagrammed in Fig. 3.11. The boards were all mechanically etched in the Magnetic Resonance Systems Lab (MRSL) using a C30 PC board prototyper (LPKF, Wilsonville OR) and the final coil was outsourced for etching (PCB Express, Mulino OR). As mentioned in III.2.1, such printed circuit board suppliers will not etch on flexible substrates - only on industry standard 0.062" laminate FR-4. The presence of so many components and solder joints on the array already prevented the array from potentially conforming to a curved surface, so losing the flexibility of the substrate for the accuracy of professional etching of such a complex board was an easy decision.

After some time and use, one final set of modifications was made to the system to increase the SNR and the ease of use.   The bias-insertion boards and potentiometer boards were all mounted on a large acrylic plate and attached to the magnet-bore-side of the flange plate of the magnet so that the blue ribbon cables were all inside the bore.   The insulation of the Gore cables that connected the bias-insertion boards to the preamplifiers was removed over a small section and the grounding shield on the cables was connected to the flange plate with copper tape and conductive epoxy. Having the cables grounded coming into the bore prevented a TEM mode, which has no low frequency cut-off, from propagating in the bore (with the bore as the outer

5760 mils

675 mils

7875 mils
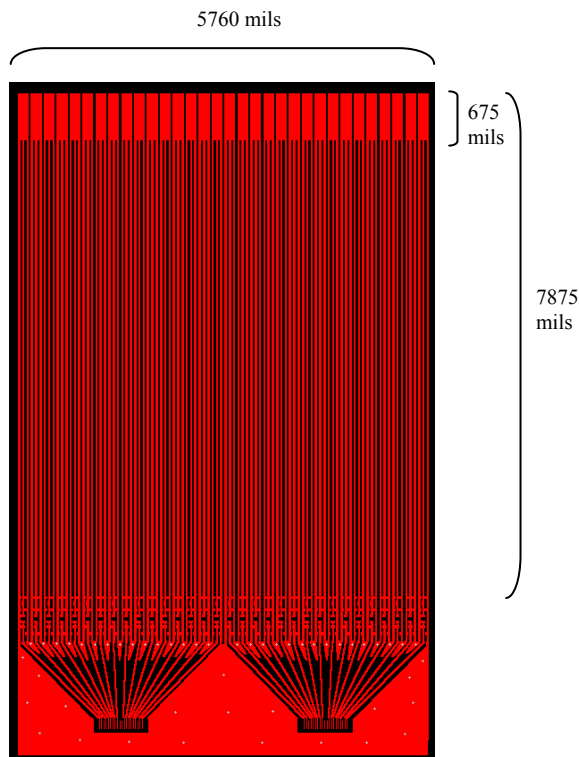
Fig. 3.12 Board layout of one 32-channel section of array for 1.5T.
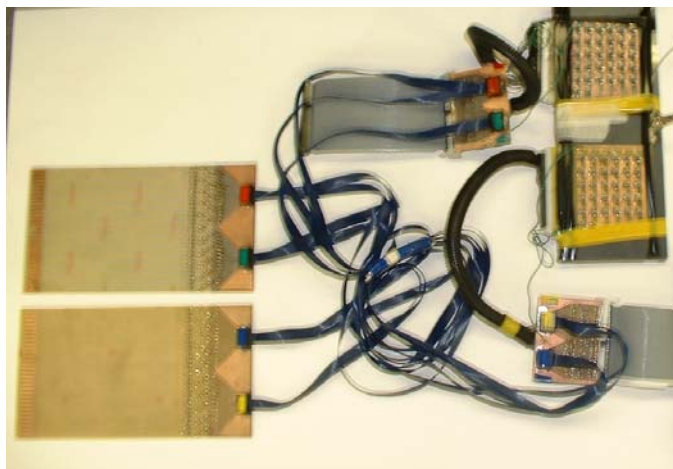
Fig. 3.13
64-channel array coil
(2x32 channel) system
for imaging at 1.5T.
The ultrasound cables,
"bias-insertion"
boards, and
potentiometer boards
are all the same design
as used at 4.7T.

conductor and the cables as the inner conductors).

III.2.4 Operative Version of 64-Channel Array Coil Scaled for 1.5T

The planar pair array was scaled to a larger version for 1.5T clinical applications, where the bore size (and volume "body" coil size) is 60cm diameter and the frequency is lower. The board layout for a 32-channel set is shown in Fig. 3.12, with dimensions labeled. The portion of the coil to be used for imaging was designed to have an overall coil dimension of 30cm x 20cm (7875mils) , yielding individual element footprints of 4.57mm (180 mil) x 20 cm. The conductor traces were 20 mils wide with 40-mil gaps between them and 40 mils between each coil. In anticipation of "stacking" the coils to do volume imaging, the array was separated into two sets of 32-channels. The ends of the planar pairs were extended in anticipation of using distributed capacitance for decoupling. The same matching and tuning components, blue ribbon cables, bias-insertion boards, and potentiometer boards were used when operating the array coil at 63.85MHz as when operating at 200MHz. The system is pictured in Fig. 3.13.

III.2.5 Evaluation of Losses

In preparation for the first use of the array on a clinical system, a "test array" was fabricated with planar pair coils in three different configurations to assess the effect of the ultrasound cables and varactors on the SNR. The first set of coils was tuned with capacitors instead of varactors and connected to the conversion board by standard RG-174 coaxial cable instead of the ultrasound cable. The second configuration was intended to test the effect of the varactors and was thus connected to the conversion board by standard coax but was tuned with varactors instead of capacitors. The third set was designed in the final 64-channel array scheme – tuned with varactors and connection to the conversion board with the ultrasound cable – in order to

Fig. 3.14 "Test array" for 1.5T to assess the effect of the ultrasound cable and varactors on SNR.

"Dummy" coil – capacitively tuned
Varactor tuned, Samtec – blue ribbon cable
Varactor tuned, BNC connection
Capacitively tuned, BNC connection
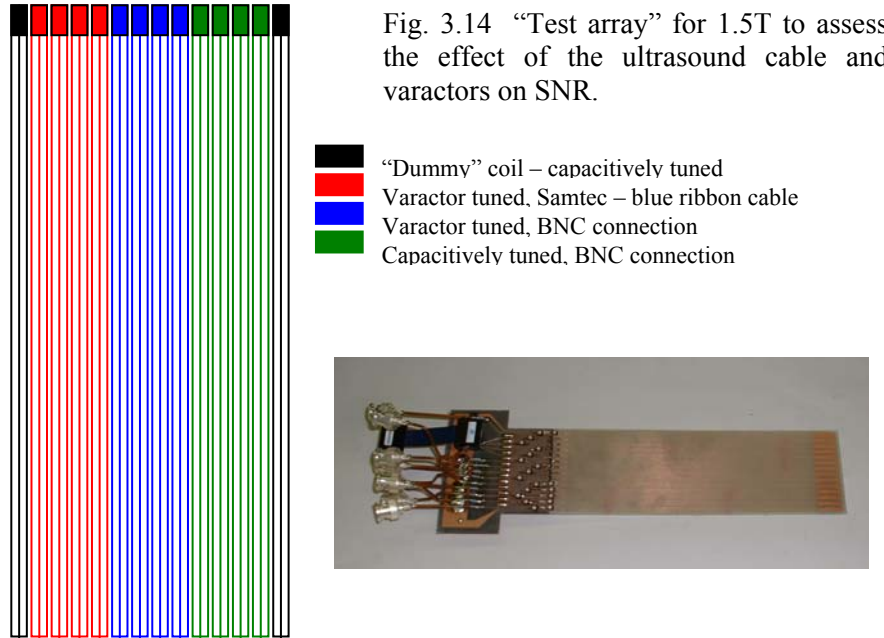
have a comparison of the overall system to the "ideal" as well assess the effect of the cabling. The test coil is diagrammed and pictured in Fig. 3.14. Measurements were made on the bench of the VSWR 2:1 bandwidth of the coils in the three different configurations and Q was calculated according to $Q = \dfrac{\omega_0}{2\Delta\omega}$, where $\Delta\omega$ is the full bandwidth between points where the voltage response falls to .707 of its peak value, corresponding to the point where the VSWR reaches 2:1(69). The relative SNR was then calculated as $\sqrt{Q}$. This is generally considered a valid assumption for a fixed coil design with inductance, L, that produces an effective flux density, B_1, defined in Eqn. 3.4,

$$B_1 = \frac{\vec{B}_1}{I_1} \cdot \hat{a}_p \qquad [3.4]$$

where $\vec{B}_1$ is the flux density produced by the coil and division by I_1, the input current, normalizes the value to make it per unit amp. The polarization vector is $\hat{a}_p = \dfrac{\hat{a}_x - j\hat{a}_y}{\sqrt{2}}$. Very general equations for *SNR* and *Q* are below, where *R* is the copper resistance of the coil:
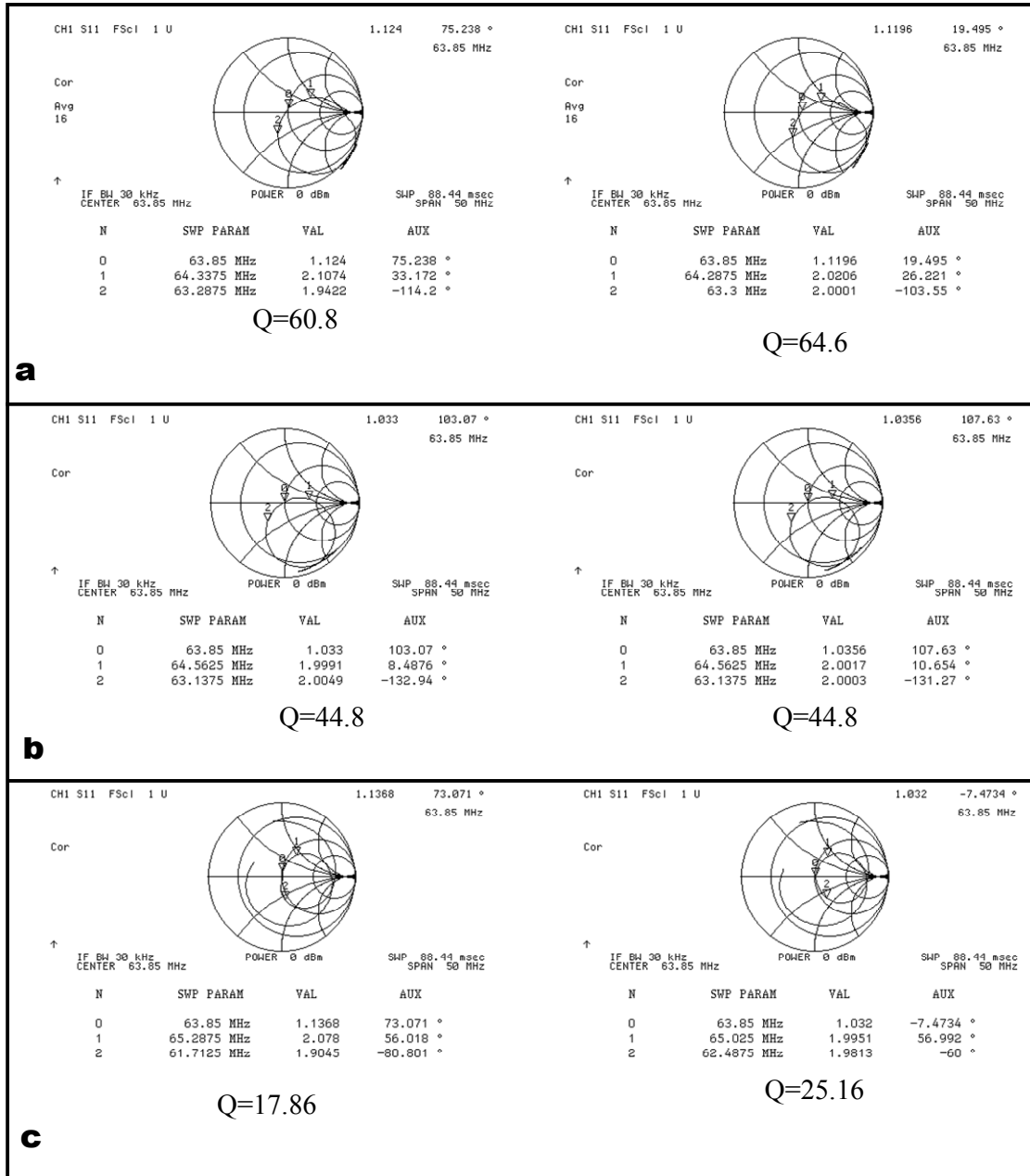
Fig. 3.15 Sample Q measurements from two coils per configuration on the test array.
   a)   Capacitor-tuned, RG-174 coaxial cable connections
   b)   Varactor-tuned, RG-174 coaxial cable connections
   c)   Varactor-tuned, ultrasound blue-ribbon cable connections

$$SNR \propto \frac{B_1}{\sqrt{R}} \qquad\qquad [3.5]$$

$$Q = \frac{\omega L}{R} \qquad\qquad [3.6]$$

It becomes apparent, then, that as long as the coil design is fixed, B_1 and L are constant, leading to the common statement that the *SNR* is proportional to the square root of *Q*.

Sample bench measurements are shown in Fig. 3.15. Measurements from multiple coils were acquired and averaged for drawing the final conclusions: The system as designed and operated, using varactors and the blue ribbon cable, showed a 41% decrease in SNR from the "ideal" capacitively-tuned-coax-connected case, with the ultrasound cable responsible for a 26% decrease and the varactors for the remaining 15%.

III.3 Decoupling

It was observed during the initial array testing that adding a capacitor between the elements acted as an effective decoupling method. The full-wave program that was used to evaluate the coupling coefficient between two planar pairs as a function of distance between them (discussed in Section III.1) was used to evaluate the coupling between two planar pairs when capacitance was added across the gap between them. Theoretically, this cancels the mutual inductance (typical source of coupling) between the coils. Figure 3.16 (70) illustrates the success of the method as a mode split in the return-loss (S_{11}) value, which indicates coupling, is closed to a single resonance by the addition of distributed capacitance between the coils – a novel implementation made possible by the coil design. In the case of the planar pair, the fields of the
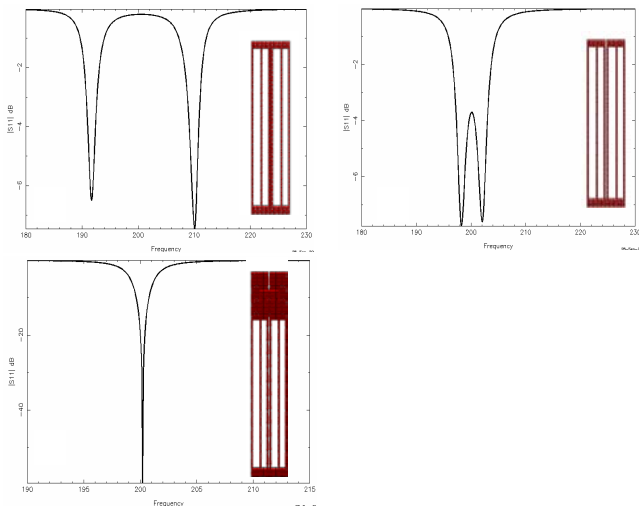
Fig 3.16   Plots of modeled S_{11} vs. frequency for the three coil pairs. (a). Two planar pairs connected along a common element (b) Two planar pairs with a gap, and (c) two planar pairs with a gap and a capacititive decoupling pad. The "mode split" indicating coupling between the coils is most severe in (a), is reduced by the gap in (b), and is eliminated by adding a printed capacitor in configuration (c).

Table 3.3 Measured S-Parameter Data for 16-Channel Planar Pair Array

Coil #	1	2	3	4	5	6	7	8	9	10	11	12	13	14	15	16
1	-34	--	--	--	--	--	--	--	--	--	--	--	--	--	--	--
2	-26	-24	--	--	--	--	--	--	--	--	--	--	--	--	--	--
3	-28	-25	-35	--	--	--	--	--	--	--	--	--	--	--	--	--
4	-27	-30	-24	-31	--	--	--	--	--	--	--	--	--	--	--	--
5	-29	-28	-31	-21	-23	--	--	--	--	--	--	--	--	--	--	--
6	-30	-29	-28	-29	-28	-24	--	--	--	--	--	--	--	--	--	--
7	-32	-31	-30	-30	-29	-30	-27	--	--	--	--	--	--	--	--	--
8	-34	-32	-32	-31	-29	-31	-33	-26	--	--	--	--	--	--	--	--
9	-35	-34	-33	-32	-31	-31	-31	-35	-27	--	--	--	--	--	--	--
10	-37	-35	-35	-34	-32	-32	-31	-31	-32	-29	--	--	--	--	--	--
11	-38	-36	-36	-35	-33	-33	-32	-31	-32	-27	-27	--	--	--	--	--
12	-39	-38	-38	-37	-35	-35	-34	-33	-31	-33	-26	-25	--	--	--	--
13	-41	-39	-39	-38	-36	-36	-35	-34	-32	-31	-28	-28	-25	--	--	--
14	-41	-40	-39	-38	-37	-36	-35	-34	-32	-31	-29	-29	-29	-24	--	--
15	-41	-40	-40	-39	-37	-37	-36	-35	-33	-32	-28	-28	-28	-28	-42	--
16	-41	-40	-41	-39	-38	-38	-36	-36	-34	-32	-28	-28	-26	-26	-31	-24

elements are well-localized over the element itself due to the fact that the ground return run on either side of the main conductor works to contain the spurious fields (see Fig. 3.4a). It is possible, then, to decouple with only a single capacitor between nearest neighbor elements, massively decreasing the typical complexity of decoupling networks (71-73).

Decoupling the planar pair coils in this manner was first tested on the 16-element array shown in Fig. 3.6 using 1-5pF variable capacitors between the coils. This data appears in Table 3.3 and shows a well-matched, well-decoupled array. The on-diagonal numbers in the table were obtained using S_{11} or S_{22} mode and indicate the degree (Return Loss in dB) to which each element is impedance matched to 50 ohms. The off-diagonal numbers in the chart were obtained using S_{21} mode and are a measure of isolation [dB] between elements in the array. An element is usually considered matched and tuned and/or isolated when the respective S_{11}, S_{22}, or S_{21} value reaches -20dB. The four-element array in Fig. 3.5 was successfully decoupled using a fixed capacitor value of 3.3pF, a value easily implemented using distributed capacitance, and design of the prototype 64-channel array for 4.7T (section III.2.2) proceeded as described above, with the expectation of decoupling in the same manner.

The coils on the prototype array were impedance matched to 50 ohms and S_{21} values between nearest neighbors in the central section of the 64-channel prototype array were measured in a range of -11.9dB to -14.1dB, with an average value over the 12 center elements of -13.1dB. 20dB of isolation was typically not reached until third neighbor. An effort was made to put decoupling capacitance between the elements, but had no effect on the coupling

measurements. To explain the unresponsiveness of the coils to decoupling capacitance, it was assumed that the coupling was occurring primarily on the cables and in the bias boxes. Pick-up probes detected strong fields at 200MHz in the bias boxes, confirming the assumption, and design and construction of the modified (operative) 4.7T 64-channel coil (section III.2.3) ensued. Despite the coupling on the prototype array, the coils tuned relatively independently and all initial SEA imaging described in the following chapter was implemented using the array.

For coupling measurements on the modified operative version of the 64-channel coil, the calibration and measurement point was the input of the system, the bias-insertion board. In order to verify that the S_{21} measurement was not significantly affected by cable coupling or coupling on the insertion board, several S_{21} measurements were also made after calibrating though the entire system to the input of the array using calibration standards specially fabricated for the Samtec connectors (see Fig. 3.17). Measurements at the two calibration points, labeled in Figure 3.11, indicated a variation of less than 1.5dB. Average nearest neighbor S_{21} values on the array were -16.8dB and always fell to better than -20dB by third neighbor, indicating that a significant portion of the coupling on the prototype array had indeed been eliminated with the bias box; however, capacitance placed between the elements still had no effect on the coupling. Full-wave modeling showed that the mutual impedance between coils of that dimension (only a 10 mil gap between them) was capacitive, with a value of $Z_{21} = -0.09-j0.15$, requiring an inductor to cancel it. The coils tuned easily and independently and the array was used to obtain publication-worthy SEA images; therefore, these coupling values were deemed adequate for future SEA imaging applications at 4.7T without redesigning another array.

When scaling the array design for clinical imaging at 1.5T, inductive coupling increased with the larger coils, thicker traces, and higher Q, and putting capacitance between the elements had the expected significant (positive) effect on the coupling. To test using distributed
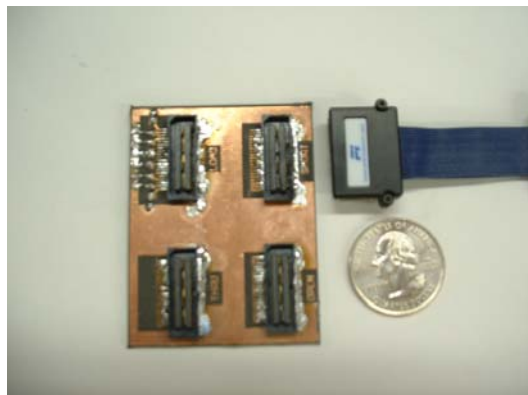
Fig. 3.17 Calibration standards fabricated for a Samtec connector, enabling calibration through the blue ribbon ultrasound cable to the coil.
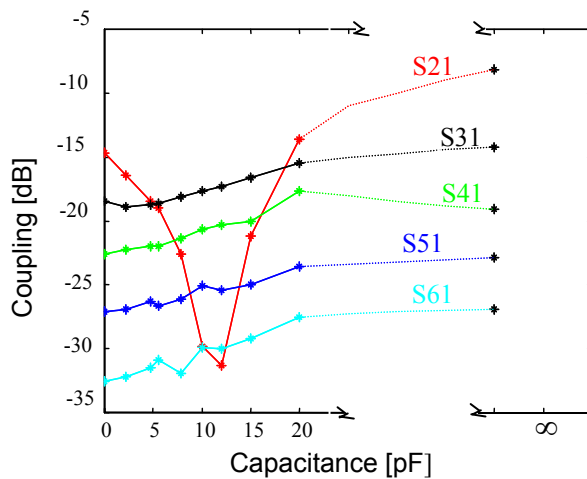
Fig. 3.18 Coupling between array elements for different values of capacitance from 2.2 to 20 pF, as well as open- and short-circuited (no gap). Optimal value for nearest neighbor decoupling is not necessarily the optimal value for best overall decoupling.

capacitance on the 1.5T design, decoupling was measured between six central elements in the array. Eight different fixed values of decoupling capacitors were tested on the 1.5T coil, ranging from 2.2 to 20 pF.   In addition, all capacitance was removed and all coils were shorted to obtain the two extreme conditions. With each value, the coils were impedance matched to 50 ohms and the coupling measured as S_{21} using the network analyzer. The results of the measurements are summarized in Fig. 3.18, showing the measured coupling between elements on the 1.5T array as a function of capacitor value.   While no single value provided simultaneous optimization of all couplings,   a value between 5 and 8 pF provided isolation of nearly -20 dB on all elements, most notably improving nearest neighbor coupling.   After determining an optimal value of decoupling capacitor, calculations for distributed capacitance using various dielectrics were made using the
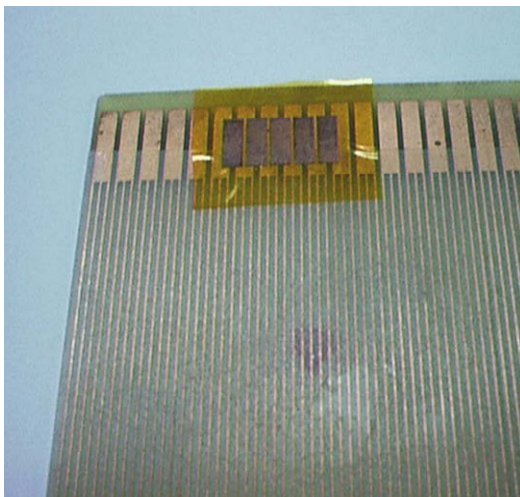
Fig. 3.19 Distributed capacitive pads fabricated on 1-mil thick Dupont Pyralux for decoupling over five of the elements (for illustration) in the 1.5T 64-channel array .

Table 3.4 Measured Coupling Data for 1.5T Planar Pair Array with Various Decoupling Implementations

[dB]	S_{21}	S_{31}	S_{41}	S_{51}	S_{61}
No decoupling capacitance	-14.7	-18.5	-22.6	-27.1	-32.5
7.8pF lumped element	-22.6	-18.1	-21.4	-26.1	-31.9
Distributed capacitive pad between elements	-20.9	-17.7	-20.7	-24.9	.28.9

standard static equation for capacitance, $C = \dfrac{\varepsilon_0 \varepsilon_r A}{d}$, where ε_0 is the dielectric constant of free space, ε_r is the relative dielectric constant of the material, A is the pad area, and d is the dielectric thickness. Printed capacitor pads were fabricated on 1-mil thick Dupont Pyralux with relative dielectric constant of 3.4. The ends of the planar pairs had been extended for the integration of the pads over the gap between the coils. Ideally, the printed capacitor would be fabricated with the coil using two-sided etching, but due to limitations of mechanical etching on thin substrates discussed in III.2.1, spray adhesive was used to attach the pads. Five pads integrated with the coil are shown in Fig. 3.19 for illustrative purposes. Table 3.4 summarizes a comparison of the coupling between the center six planar pair coils of the array with and without decoupling capacitance between coils, showing that implementation with distributed capacitance provided equivalent performance. In the table measurements, S_{21} represents a coupling measurement to
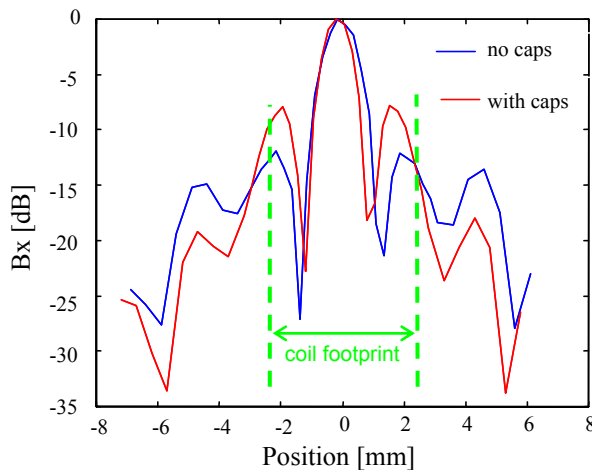
Fig. 3.20 Pattern plot of the planar pair coil element at approximately the coil element width above the array. A linear pickup coil was used, resulting in pattern nulls where the field is orthogonal to the pickup coil.   The decoupling capacitors   diminish   the   field intensity   outside   of   the   coil footprint. The first lobe is reduced without the decoupling capacitors due   to   interference   from   the adjacent coils.

nearest neighbor. S_{31} is a coupling measurement to next-nearest neighbor, etc. To quantify the effect of decoupling on the field patterns of the coils, field pattern plots were obtained using a micropositioner and a linear pickup coil. The plots are shown in Fig. 3.20, verifying the improvement in the measured field pattern when the coils are decoupled. When properly decoupled, the fields outside of the coil footprint decrease and the fields inside the coil footprint narrow and increase due to lack of cancellation from coupled neighbors.

III.4 Field Patterns and Signal-to-Noise Ratio vs. Penetration Depth

With modeling and bench measurements in agreement that the array was suitable for Single Echo Acquisition, the remaining verification was to image in the coronal and axial planes to quantify the field patterns of the coil. From coronal images, agreement with the modeled pattern profiles in Fig. 3.4a were expected to be obtained, confirming the contained field patterns of the planar pair. The axial images were intended to view the SNR versus penetration depth modeled in Fig. 3.4c.

III.4.1 Field Patterns

A set of profiles from seven adjacent coils on the prototype 4.7T array are shown in Fig. 3.21. Similarly, coronal images from four adjacent coils on the operative version of the 4.7T array and a plot of their profiles are shown in Fig. 3.22. The phantom used was a 13cm diameter round dish with spiraled compartments containing resolution structures and alternatingly filled with distilled water, 0.5g/L $CuSO_4$, and 1g/L $CuSO_4$. The images show well-contained "strips"
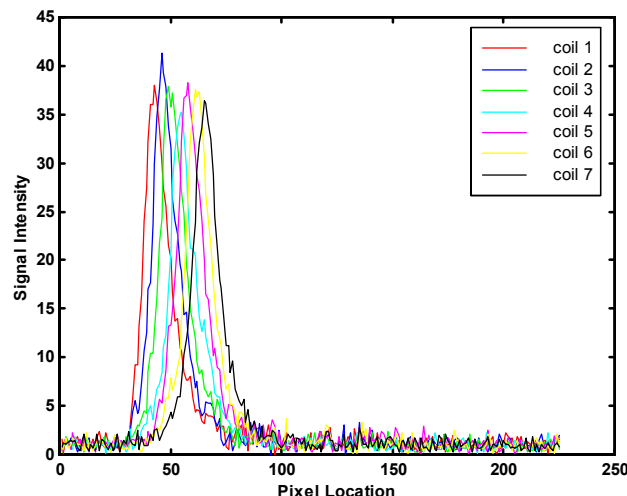
Fig. 3.21 Coil profiles from seven adjacent coils on the prototype 4.7T 64-channel array, showing the pattern separation that made initial SEA imaging possible.
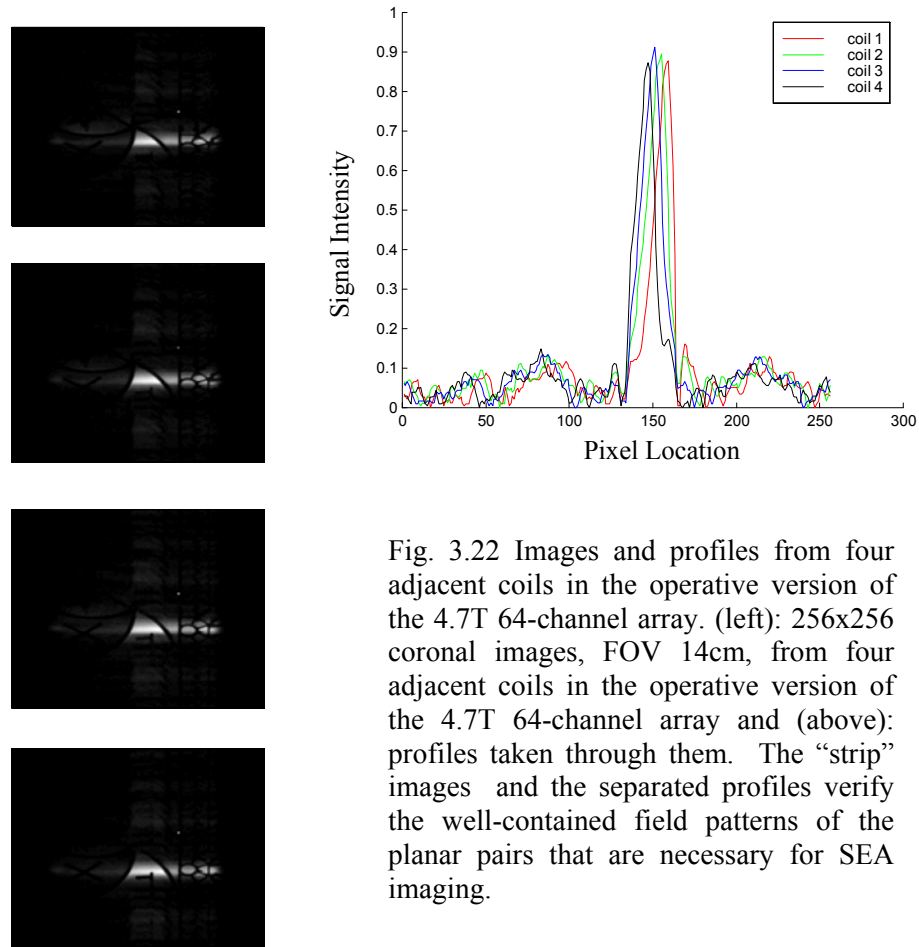
Fig. 3.22 Images and profiles from four adjacent coils in the operative version of the 4.7T 64-channel array. (left): 256x256 coronal images, FOV 14cm, from four adjacent coils in the operative version of the 4.7T 64-channel array and (above): profiles taken through them. The "strip" images and the separated profiles verify the well-contained field patterns of the planar pairs that are necessary for SEA imaging.

that are well-suited for SEA imaging where each coil will be responsible for a strip of information directly above it. The profiles confirm reasonable separation of the field patterns, as is necessary for SEA. Variations seen in the gain (different peak heights) between coils are adjusted during reconstruction.

Single-coil field pattern data was obtained at 4.7T and 1.5T by running the output of one coilin the respective array through the Omega receiver in the MRSL (4.7T) or the GE receiver (1.5T) at M.D. Anderson Cancer Center in Houston, TX. A coronal image taken with the 4.7T operative array and a "zoomed" profile is shown in Fig. 3.23 in order to more easily compare to modeled field patterns, such as those shown in Fig. 3.4a. The phantom used was the spiral dish described above. Images from the 1.5T coil and similar plots are shown in Fig. 3.24. The phantom used at M.D.A. was a rectangular dish with no structures, but again with compartments filled with alternating concentrations of copper sulfate. A notable difference between the modeled and measured patterns in the two figures is in the x-axis: The x-axis of the models is in
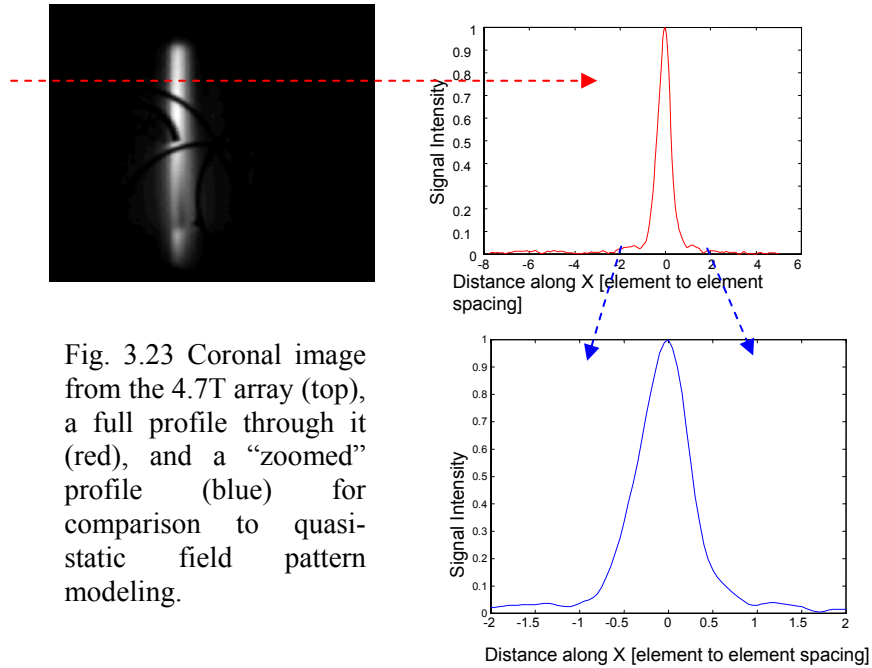
Fig. 3.23 Coronal image from the 4.7T array (top), a full profile through it (red), and a "zoomed" profile (blue) for comparison to quasi-static field pattern modeling.
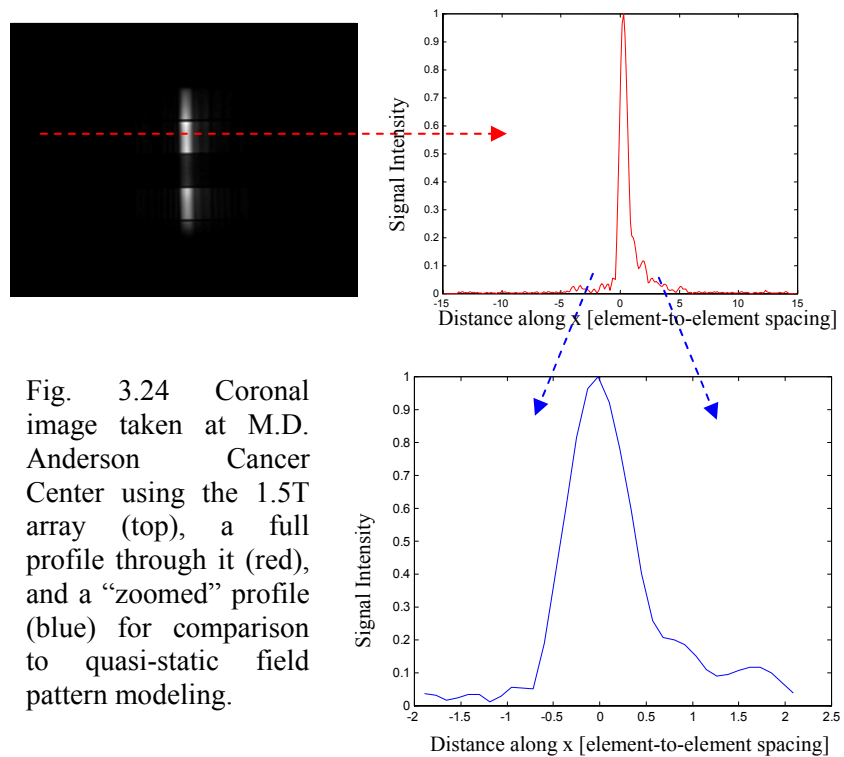
Fig. 3.24 Coronal image taken at M.D. Anderson Cancer Center using the 1.5T array (top), a full profile through it (red), and a "zoomed" profile (blue) for comparison to quasi-static field pattern modeling.

"coil-widths" and, since the measured data is acquired in an array environment, its axis is in element-to- element spacing, which includes the gap between the coils. This has the effect of making the pattern appear narrower in the measured data. After taking this into account, as well as the fact that coupling was present (also because the coils were in an array environment), the modeled and measured patterns agree relatively well at this height above the array. In particular, in the case of the imaging session at M.D.A., four adjacent coils were tuned, no decoupling used, and the image above was taken with an edge coil, leading to "one-sided" coupling in the profile.

III.4.2 Signal-to-Noise Ratio vs. Penetration Depth

The standard procedure for measuring SNR in an MR image is simple division of the signal at a point of interest by a large, averaged, region of noise in the image. More rigorous standards to characterize coils have been defined, however, primarily for pre-market approval purposes. NEMA MS 6: *Characterization of Special Purpose Coils for Diagnostic Magnetic Resonance Images* contains criteria for mapping of the coil sensitivity region in terms of SNR (according to NEMA MS 1 method) and field uniformity (according to NEMA MS 3 method). NEMA MS 9: *Characterization of Phased Array Coils for Diagnostic Magnetic Resonance Images* contains guidance criteria for SNR and image uniformity (according to NEMA MS 6 methods) of images obtained with arrays. Due to the fact that the work presented in this dissertation was partially funded by an agency interested in commercialization, an effort was made to characterize the SNR of the coils using NEMA standards. Our array is comprised of "specialty coils" (as opposed to coils which are uniform over the region of interest) and Matlab code for image SNR evaluation was therefore written in accordance with NEMA MS 6.
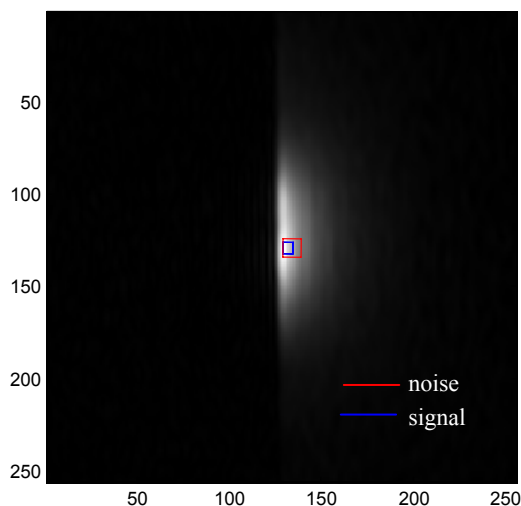
Fig. 3.25
Coil pattern with the appropriate signal and noise calculation areas marked for SNR evaluation in accordance with NEMA MS 6.

The 1.5T 64-channel array was used to perform the imaging experiments at the University of Würzburg in Würzburg, Germany. All experiments were performed in the method appropriate to evaluate SNR in accordance with the NEMA MS 6 standard: Two images were acquired using a standard sequence within a time period not exceeding five minutes. The signal was calculated as the mean of a 7x7 pixel area in the center of the region of interest (ROI) in one of the images. The noise was calculated by subtracting the first image from the second, taking an 11x11 pixel region surrounding and including the signal region, testing the pixels for adequate signal level, taking the standard deviation in the region and dividing by $\sqrt{2}$. Figure 3.25 shows a zoomed image of a single 180-mil (4.6mm)-coil pattern obtained at 1.5T during the imaging experiments in Würzburg, Germany with the signal and noise calculation areas marked. The coil patterns were "zoomed" by sinc-interpolation of 128x256 images to 1024x1024, and then the central 256x256 region surrounding the coil pattern extracted for evaluation. This was an unanticipated but necessary step once the NEMA evaluations were implemented. The efficacy of the method requires a 7x7 pixel region of homogenous signal - not a trivial requirement in coils designed to
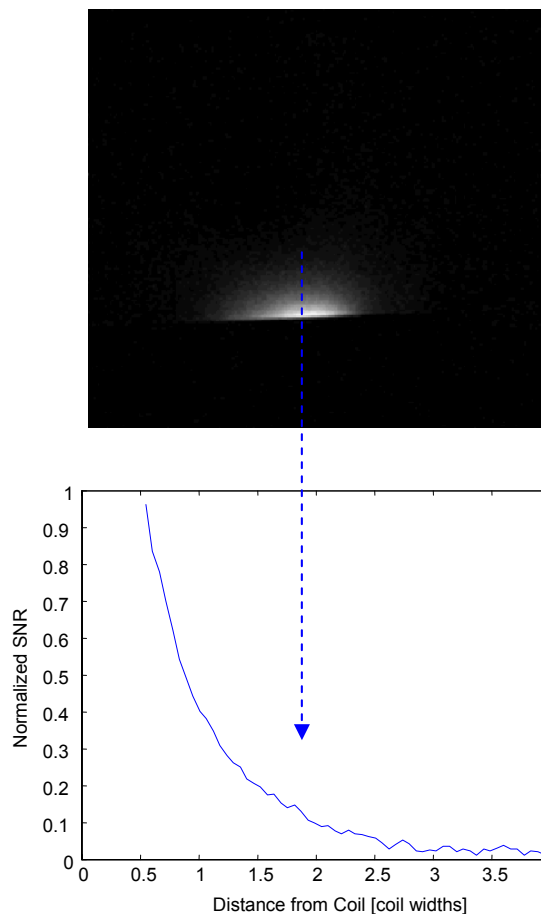
Fig. 3.26 3cmx3cm FOV, NA=8 axial image made with the 4.7T array coil (top) and profile giving normalized SNR vs. penetration depth (bottom). Unnormalized SNR peaked at 68.9. The expected shallow penetration depth is seen. The field fall-off occurs even more quickly than in the models, caused by an artifact discussed further in Chapter V.

be of pixel dimensions. Therefore, extremely high resolution, small FOV imaging would need to be performed in order to properly implement the NEMA SNR measurements.

Because the NEMA method is not readily suitable for SNR analysis on coils of this size, the SNR in the images shown in the following figures was taken using the standard procedure, which, once normalized (for comparison to the quasi-static modeling), is essentially the coil sensitivity pattern profile from an axial image. The true unnormalized SNR in the 4.7T image shown in Fig. 3.26 peaked at 68.9 and the true unnormalized SNR in the 1.5T image shown in Fig. 3.27 peaked at 64.9. The 4.7T images were acquired in the MRSL and the 1.5T images were acquired at M.D. Anderson Cancer Center during the same imaging session as the field pattern profiles shown in Fig. 3.24.

As mentioned before, the useful imaging region of a surface coil is generally considered to be within a coil-width above it, and, when the modeled and measured SNR data is compared, it can be seen that the field falls off even more quickly than expected. Whereas the modeled data is at 40% of peak value at a coil width away from the coil, the measured data has fallen to less than 10% by that point. This phenomenon is caused by a full-wave artifact discussed in-depth in
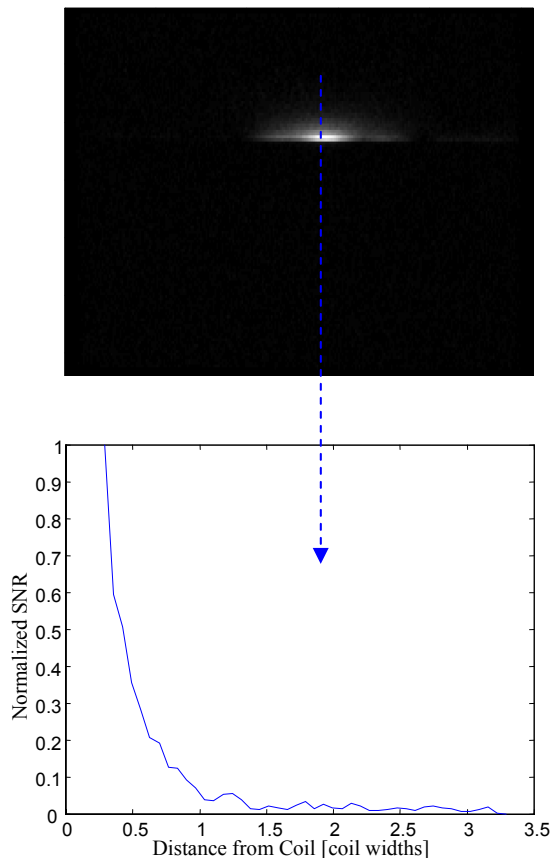
Fig. 3.27 1.5T, 4cmx4cm FOV, NA=8 axial image (top) and profile giving normalized SNR vs. penetration depth (bottom). Unnormalized SNR peaked at 64.9. The expected shallow penetration depth is seen. The field fall-off occurs even more quickly than in the models, caused by an artifact discussed further in Chapter V.

Chapter IV. It can be broadly stated, then, that a characteristic inherent to the array and SEA imaging is a shallow penetration depth. This was to be expected as the penetration depth of coils small enough to effectively replace a pixel in the phase encoding direction (and maintain a standard degree of resolution) could understandably never be more than a few millimeters at best. In this case, however, any initial uncertainty regarding the clinical utility of the array or the method was outweighed by the excitement of the pure demonstration and exploration of a new imaging technique, one which offered the possibility of imaging at rates approaching 1000 frames per second. In addition, there is undoubtedly a need for extremely rapid, shallow MR imaging, as will be discussed in Chapter V. First, however, SEA imaging – with its capabilities and its limitations – is discussed in detail in the following chapter, as the methodology is developed and explored.

CHAPTER IV

IMPLEMENTATION OF SINGLE ECHO ACQUISITION (SEA) IMAGING

The basic premise behind the Single Echo Acquisition (SEA) imaging method is the acquisition of a fully encoded (N_pxN_f) MR image by simultaneously receiving a single echo (sampled N_f times) from each of N_p coils that are well-localized in the direction normally used for phase encoding. The previous chapter described the design and construction of the appropriate application-specific array coils to implement the method, and this chapter discusses the Single Echo Acquisition method itself: In the first section, a detailed description of SEA is provided. Section 2 contains a chronological presentation of SEA images obtained over the past several years, concluding with a fleshing-out of 64-channel capabilities with highly accelerated imaging. Until this point in the research, SEA images had been simulated from single k-space lines selected from a fully encoded data set. This was motivated by an effort to study the fact that the SNR of the SEA image formed and its sensitivity to various spatial frequencies were very dependent on the k-space line selected. When forming an image truly using a single RF excitation, the k-space line must be pre-selected and thus began a study of the necessity to use a "phase compensation gradient" which is presented in the third section. The last section summarizes the capabilities and limitations of SEA imaging.

IV.1 Basic Methodology of Single Echo Acquisition MR Imaging

To form a conventionally encoded N_pxN_f (*number of phase encoding steps* x *number of frequency encoding samples*) MR image normally , appropriate RF excitations and gradients are applied, an echo is "read-out" by sampling it N_f times, and the entire experiment is repeated N_p times – once for each phase encoding gradient strength. In Single Echo Acquisition (SEA), slice selection and frequency encoding are performed using standard gradient methods, with the frequency encoding along the long axis of the array elements and slice selection in the coronal plane, parallel to the array. The phase encoding repetitions are eliminated, however, and replaced by the spatial localization provided by N_p long and narrow, parallel and closely-spaced elements of a receive array coil, described in Chapter III (see Fig.4.1). Using the prototype 64-channel receiver constructed in the MRSL (60), the signal from each of the 64 coils is simultaneously received after RF excitation. As described in (74), the signals are then mixed to an intermediate frequency of 0.5 MHz where they are digitized with 16-bit resolution at a 2.5 MHz sample rate.
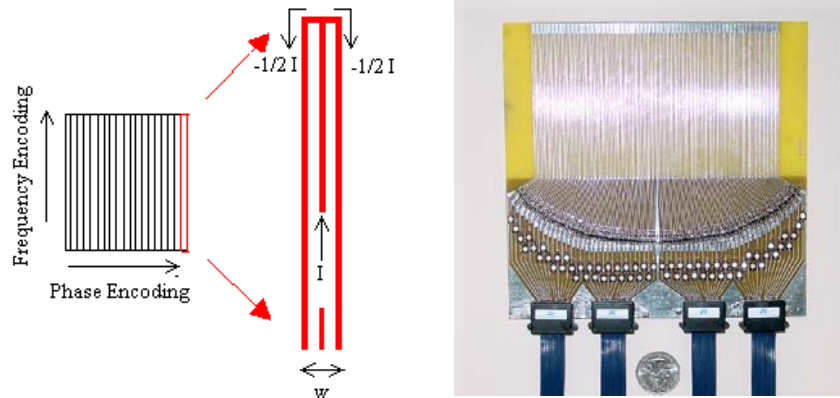
Fig. 4.1 Depiction of phase encoding replaced with coil information. In SEA imaging, frequency encoding is performed using standard gradients along the long axis of the array and the phase encoding is replaced by the spatial localization provided by long and narrow, parallel and closely spaced coils.

All 64 channels are digitized simultaneously. Digital I/Q demodulation of the sampled signals is performed using in-house software following all data acquisition. For SEA imaging reconstruction, a 1-D FFT is performed on the echo received from each coil, the resulting 64 images stacked into a $64 \times N_f$ matrix, and the matrix interpolated to $N_f \times N_f$ for display. The process is graphically described in Fig.4.2.

The SEA pulse sequence is a modified version of the standard spin-echo sequence on the GE

Simultaneously digitize and demodulate 1 echo from 64 coils

64 1-D FFT's

Stack in video memory and display
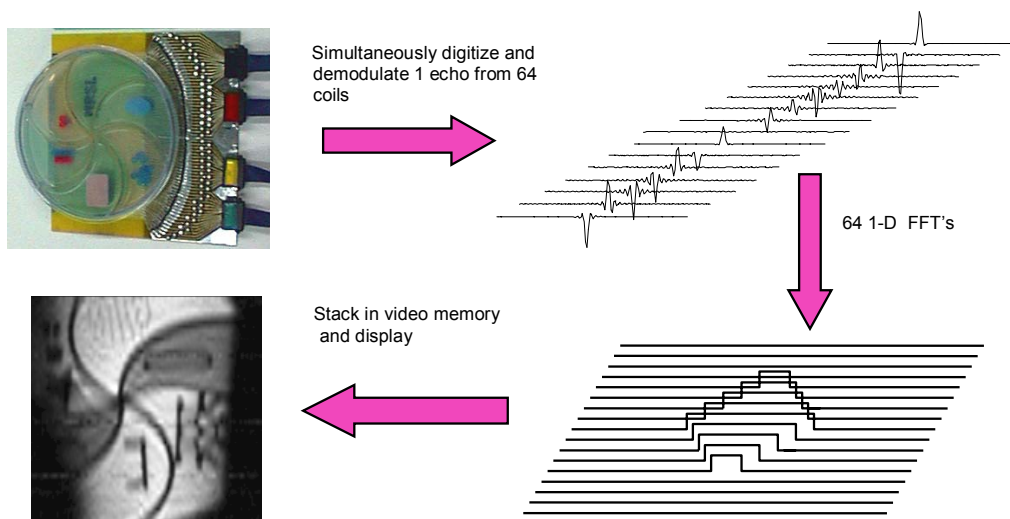
Fig. 4.2 Graphical depiction of Single Echo Acquisition. A SEA image is formed by taking 1D Fourier transforms of each of the 64 echoes and stacking them to form an image.

Omega 4.7T/33cm in the MRSL with the phase encoding table removed and replaced by a single "phase compensation gradient" pulse, discussed in Section IV.3   In an effort to study and optimize SEA images, however, most initial images were actually simulated from a single k-space line from a full data set.   Specifically, 64 fully encoded $N_p x N_f$ raw data sets were simultaneously acquired (one from each coil) by running a standard spin-echo pulse sequence. Then, N_p SEA images ($64 x N_f$) were reconstructed – one from each phase encoding line – and characteristics such as SNR and resolution in each of the images were examined. It was not necessary to actually implement SEA imaging using a single RF excitation with the pre-selection of a single k-space line until initial studies of the images and procedure were well-understood and optimized well enough to begin implementation of SEA applications, such as fast-frame-rate acquisitions. Chronologically presented example images and discussion of imaging specifics are given in the following section.

IV.2 Single Echo Acquisition Procedure Specifics and Images

Initial testing of SEA was implemented with 32 of 64 channels of the prototype array built for 4.7T imaging. Figure 4.3 is an illustration of the phantom used for the initial results using the 32 element array.   It consists of a square dish, filled with 1g/L copper sulfate, and a section of perforated board and a capillary tube for structure.   All images were obtained using a gradient echo pulse sequence using a 7 msec echo time and a 250 msec repetition time. Figures 4.4a-b
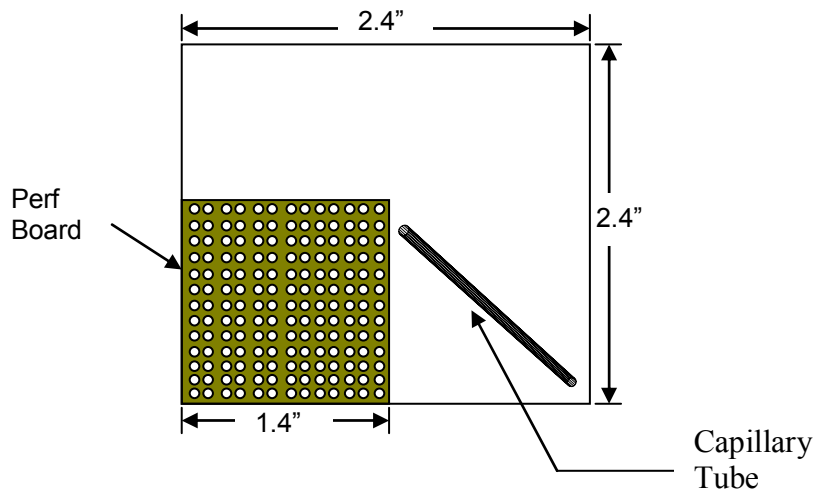
Fig. 4.3 Phantom used for initial testing of 32 channel SEA imaging. Corresponding images are in Figure 4.4a-b. Perf board has 0.050" holes on a 0.1"x0.1" grid. Capillary tube has a 0.03" diameter.
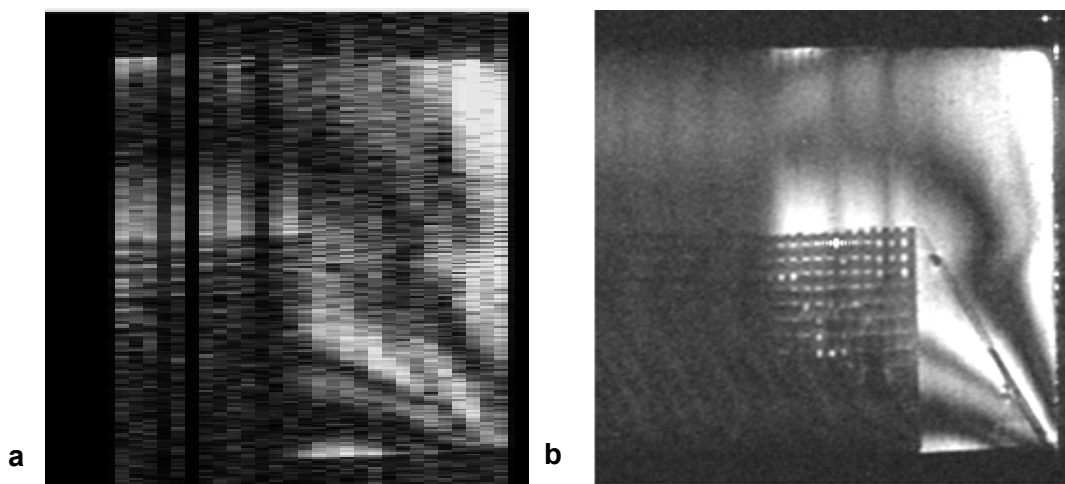
Fig. 4.4 Initial SEA image and sum of squares comparison. a: An initial SEA image, formed from a single echo received by 32 coils, total acquisition time 12 msec. b: Fully encoded, sum-of-squares image made with the same array, acquisition time 32 seconds.

demonstrate initial results obtained with the prototype 64 element array. Figure 4.4a is the SEA image obtained using no phase encoding – only a single echo received simultaneously from each of 32 coils. To separate which vitiations are products of SEA and which are inherent to the image itself, a 128x256 sum-of-squares image from the coils is shown in Fig. 4.4b, obtained by summing the fully encoded images from each of the elements. The dark shadings seen across both images were caused by shim inhomogeneities in the static field, a problem which improved when new gradient coils were later installed in the magnet. At the time, a 25cm unshielded Oxford shim/gradient set was being used in order to fit a transmit coil in the bore large enough to hold the 64-channel array. It is generally considered difficult to create a homogenous field in a large volume coil at 4.7T, and some of the shadings might also have been due to inhomogeneities in the RF transmit field, a problem which improved when a new transmit coil of a different design was later built. While gradient echo pulse sequences are generally considered to be a common approach to fast imaging, they are also much more affected by inhomogeneities than spin echo sequences, and when quality over speed was later being investigated, spin-echo sequences were used. Variations in signal strength between coils in the SEA image were due to several reasons: the varactors were not functioning on several coils and the pre-amplifiers and receiver channels had varying gains as well. The coils would be repaired and other variations adjusted during reconstruction in later SEA images. The expected loss of resolution inherent to the SEA method is seen, as the resolution in the phase encoding direction is determined by the coil footprint (2mm in this case) and in the frequency encoding direction by the FOV/N_f. On the

other hand, acquisition times were 32 seconds for the fully encoded image,   and approximately 12 msec for the SEA image. In this case, image acquisition time in the single shot images was recorded as the length of time from the RF pulse to the end of the acquisition window, as the repetition time is not a factor in SEA images. Figure 4.5 shows another SEA image and sum-of-squares using the same imaging parameters but a different phantom and a repaired and re-tuned coil. Structure is clearly evident where the SNR is adequate. Signal drop-out is again due to shim inhomogeneities.

Figure 4.6 shows the first 64x256 image acquired using SEA and a comparison sum-of-squares image using all 64 channels. Variations between channels is, as before, due to
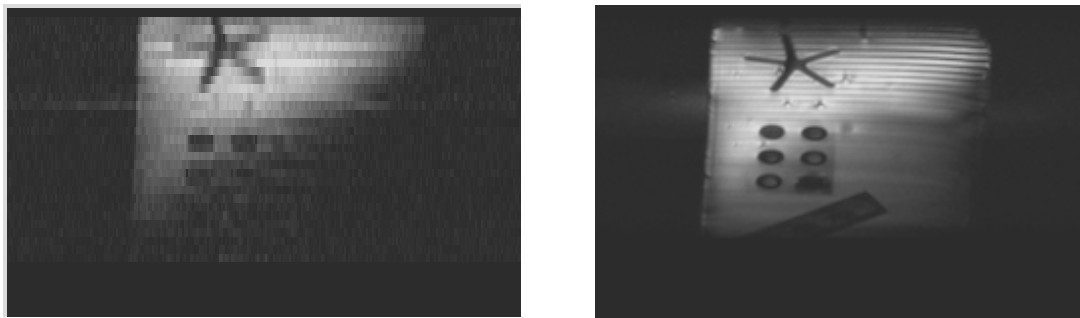
Fig. 4.5 32-channel SEA image (left) showing clear structures and signal drop-off due to static field shim and a 128x256 sum-of-squares image (right) of the same phantom.
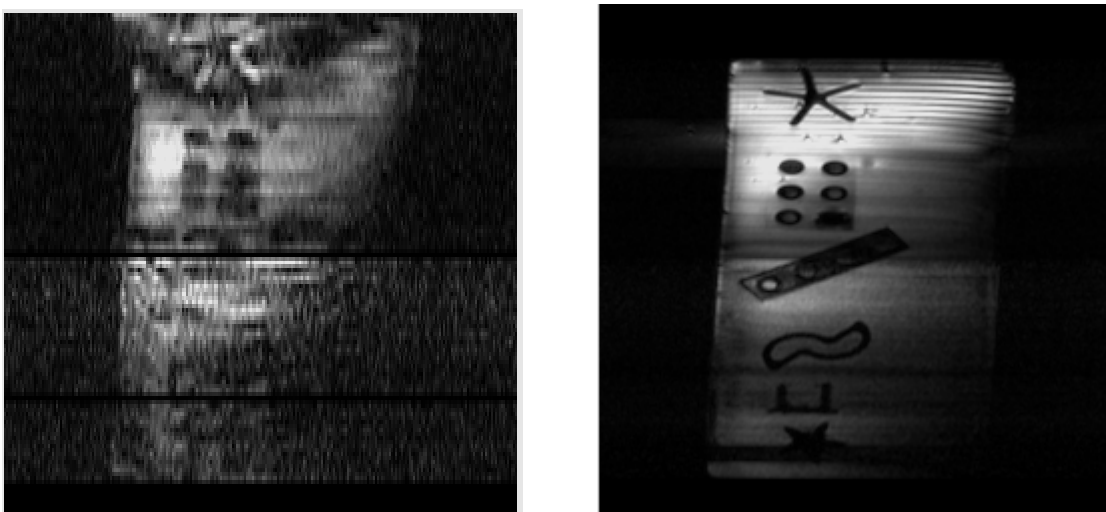
Fig. 4.6 First 64-channel SEA image (left) and a 128x256 sum-of-squares image (right) of the same phantom. Signal variations are explained in the text. Image acquisition time for the SEA image was 12msec and for the sum-of-squares image was 32 seconds.

differences in gain in the pre-amplifiers and receiver that would later be adjusted. Thirty-two of the channels have a significantly degraded SNR, a problem later discovered to be rooted in a set of preamplifiers. Finally, investigation into the phase effects of the coils was just beginning and perhaps a different choice in k-space line might have provided a better image, particularly noticeable in the area of the "inverted" star at the top.

Figure 4.7 shows the first published SEA image (74), with such improved homogeneity due to the use of a spin-echo sequence over a gradient echo sequence. The figure shows a SEA image, 64x256 (interpolated to 256x256 for display) compared to the sum-of-squares image, 128x256 (interpolated to 256x256 for display). The images are of a 12.5cm x 4.9 cm phantom filled with relaxed copper sulfate solution and various structures. Images were obtained at 128x256 resolution using a standard spin echo sequence, with a 300 msec TR and a 30 msec TE. This resulted in an image acquisition time for the conventional MR images of 38 seconds and an acquisition time for the SEA image of 30msec.

At this point, several large changes were made, not necessarily in the procedure, but in the tools used. The change was made to the operative version of the 4.7T 64-channel array coil described in III.2.3, giving an increase in SNR and a decrease in coil-to-coil coupling. The gradient coils were switched to 18-cm i.d. Accustar S-180 shielded gradient coils, smaller than the Oxfords, but offering better homogeneity in the shim, more stability, and faster switching. This led to the construction of a smaller transmit coil, the "parallel plate" coil that was also more
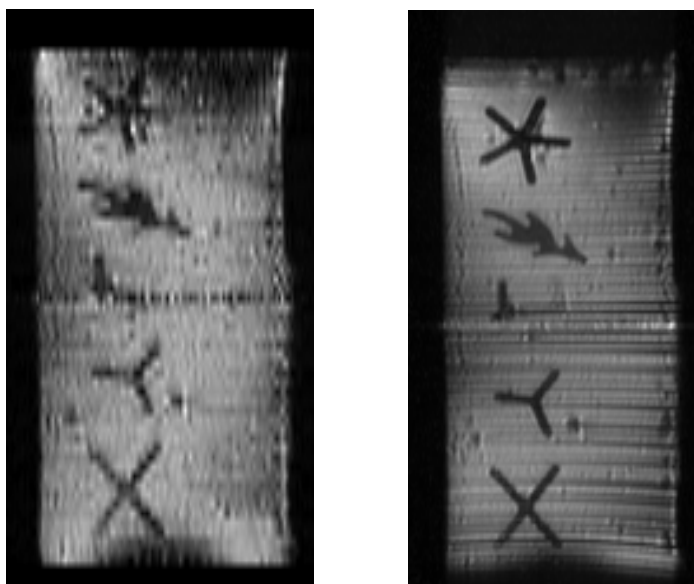
Fig.4.7 64-channel SEA image (left), obtained in 30msec and sum-of-squares combined image (right) obtained in 38seconds. Improved homogeneity over Figs. 4.4-4.6 is due to the use of a spin-echo sequence.

homogeneous with a much higher efficiency. This also resulted in better geometric decoupling between the transmit coil and the array. A larger, circular phantom was constructed that covered the entire array, resulting in a better shim as the boundary of the phantom in the static field direction was off the edge of the coil, minimizing susceptibility problems. The new phantom was constructed from a 13-cm diameter dish containing spiraled compartments filled with various objects and alternatingly filled with distilled water, 1g/L copper sulfate, and .5g/L copper sulfate. The entire operative setup for SEA imaging at 4.7T in the MRSL is shown in Fig.4.9 on the following page. Images were obtained using a standard, spin-echo pulse sequence with resolution 256x256, TR 250msec, TE 13msec, 1 average, spectral width 50kHz, FOV 14cm. Imaging was performed in the coronal plane, parallel to the plane of the array, slice thickness of 2mm, centered 4mm above the array – slightly more than a coil width. An example of the highly improved (and publicized (75)) SEA image and the sum-of-squares comparison is shown in Fig. 4.8.

Once the stability/predictability of the imaging system was under control, it was possible to explore highly accelerated imaging using partially parallel imaging techniques as well. Accelerated images were reconstructed using a method similar to PILS (40): the 64 full data sets were decimated, Fourier transformed, masked according to the coil profile to eliminate aliasing, and a sum-of-squares reconstruction implemented. Beginning from a full
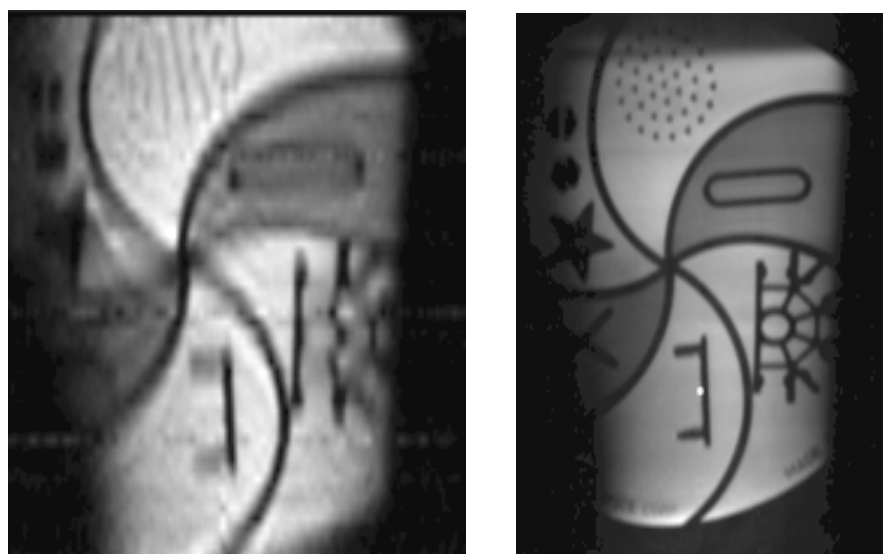
Fig. 4.8 SEA image (left) formed using the operative version of the 4.7T array coil, improved gradient coils, and an improved transmit coil. For comparison of structure, a fully encoded sum-of-squares image from the array coil is shown on the right.
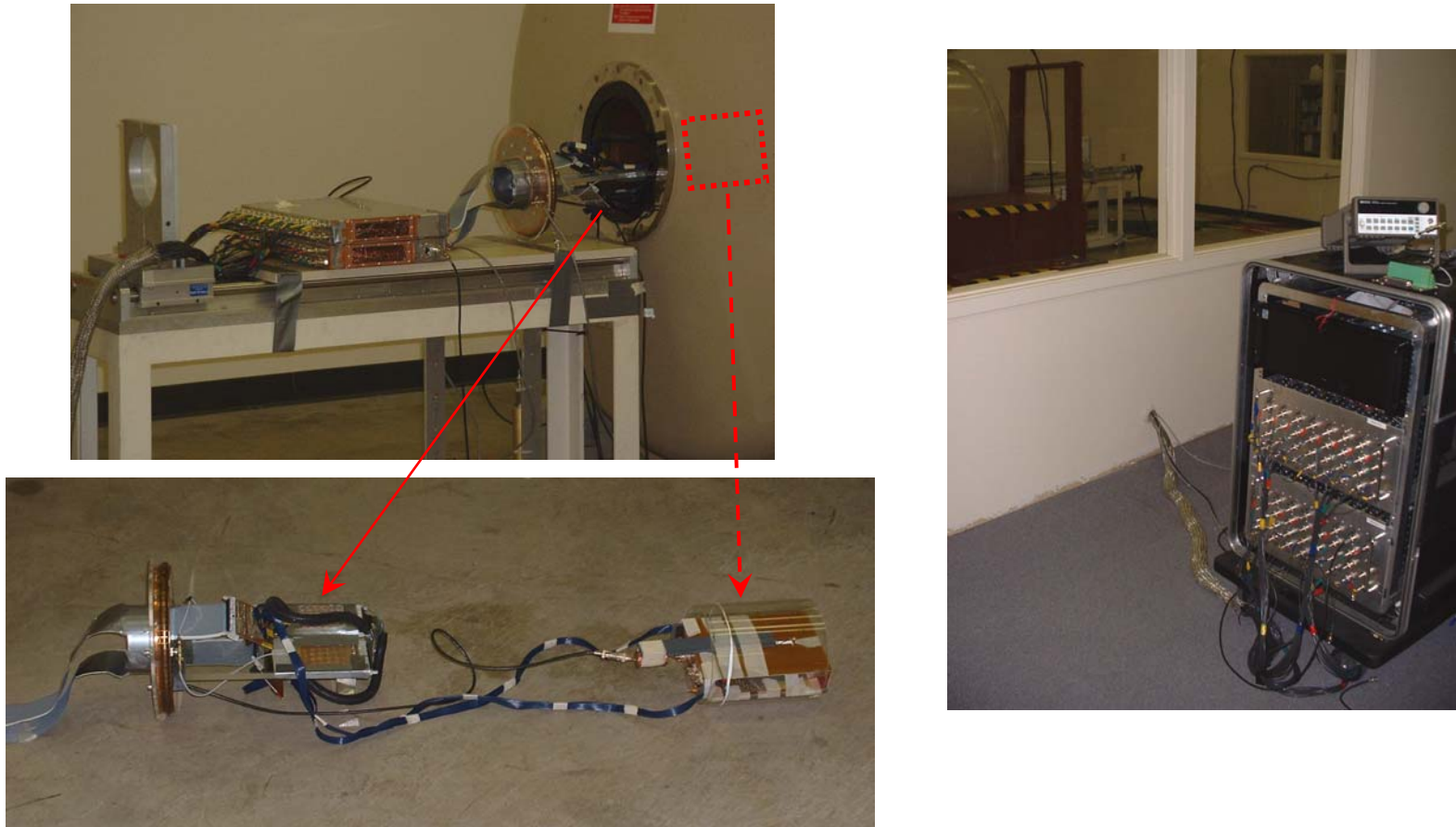
Fig. 4.9 Operative set-up for SEA imaging at 4.7T in the MRSL. Top left: Array apparatus coming out of the magnet bore connected to two stacked 32-channel preamplifer boxes by two 32-channel Gore ribbon cables. The Gore cables are grounded at the flange plate, which in turn inserts into the magnet bore opening/shield. Sixty-four RG-174 coaxial cables connect the preamps to the receiver, outside the magnet room (far right). Below: An independent view of the flange plate and coil are shown below, as the red arrows indicate. The platform off the flange plate holds the bias-insertion boards and the potentiometer boards. Ultrasound cables connect to the array coil, which is shown inside the parallel plate transmit volume coil.

256x256 data set, imaging at acceleration factors from two to 64 were simulated by using only 128,64,32,16,8, and 4 k-space lines. Images were also constructed with only two and a single k-space line (SEA imaging). While the imaging time was accelerated by factors of 128 or 256 in these images, it was appropriate and necessary at this point to distinguish acceleration due to coils and acceleration due to k-space manipulation, a point of discussion in the field of parallel imaging. While both resulted in SNR loss according to the square root of the acceleration factor, as discussed in II.2.3, each had a different effect on resolution (discussed below) and it was therefore necessary to distinguish between the two. Therefore, coil acceleration was notated as L_c, strictly k-space acceleration as L_k, and total acceleration in the standard notation L. The results of the accelerated imaging are shown in Fig. 4.10. The SNR actually increased by $\sqrt{2}$ with the first acceleration, although the number of k-space lines used for reconstruction was decreased by a factor of two. This is due to a phase effect of the voxel-sized coils discussed in the following section which forces all the data into half of k-space. Therefore, eliminating the half of k-space with no signal left the signal essentially unaltered, but decreased the noise by a factor of two, increasing the SNR by the square root of two. Following the first acceleration, however, the SNR followed the $\sqrt{L}$ loss expected. Artifact power (AP) is a number used to quantify the image degradation due to acceleration and increased as expected with acceleration factor (76). It is generally defined to be the ratio of the power in the difference between an "ideal" unaccelerated image, $I_0(x,y)$, and the accelerated image, $I_L(x,y)$, to the power of the unaccelerated image:

$$AP(\%) = \frac{\sum_{x,y} \left| I_L(x,y) - I_0(x,y) \right|^2}{\sum_{x,y} \left| I_0(x,y) \right|^2} \cdot 100 \qquad [4.1]$$

The resolution did not begin to significantly degrade until only two lines of k-space were used for reconstruction. This was due to the fact that there was an overlap in the coil patterns and it required at least four lines of k-space (corresponding to L_c=64) to effectively separate these spatially – i.e. to avoid aliasing into the masked region of another coil. Once the acceleration factor exceeded the number of coils, as was the case when two lines of k-space were used for reconstruction (corresponding to L_c=64, L_k=2), then the information lost in the acceleration was unrecoverable and the resolution suffered notably. It is worth noting that the intuitive loss of resolution expected in any 64x256 image and seen in the blurring of smaller features in the SEA image (Fig. 4.8) is of a visually and physically different type than the aliasing-based loss of resolution seen in the PILS highly accelerated images. The width of the coil pattern is
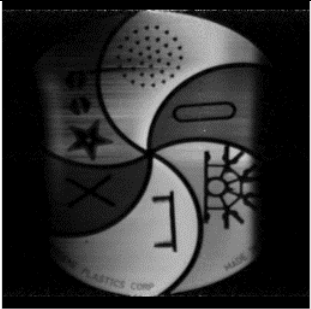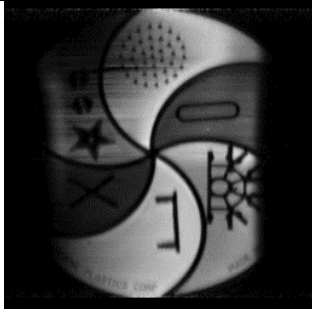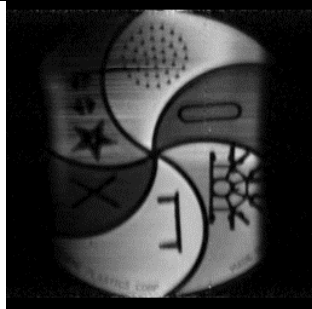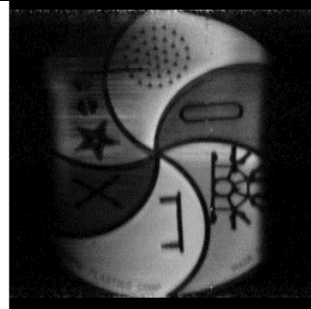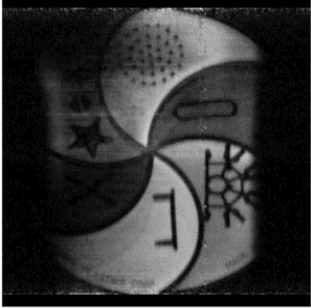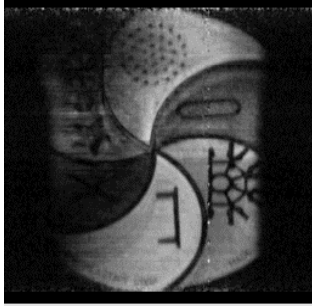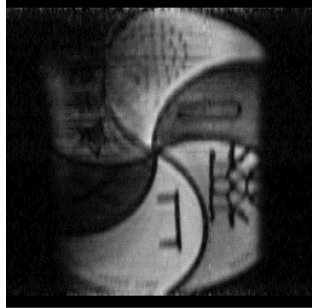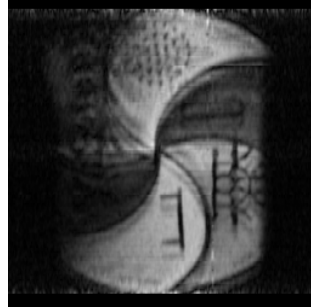
256 lines, L_c = 1 SNR 55, AP 0	128 lines, L_c = 2 SNR 71 (half-k), AP 0.4	64 lines, L_c = 4 SNR 51, AP .45	32 lines, L_c = 8 SNR 35.6, AP .84
16 lines, L_c = 16 SNR 26.2, AP 1.75	8 lines, L_c = 32 SNR 20.5, AP 2.97	4 lines, L_c = 64 SNR 28.5, AP 3.00	2 lines, L_c=64, L_k = 2 SNR 30.4, AP 5.79

Fig. 4.10 Accelerated images made using the 64-channel array coil. Following the first acceleration by a factor of 2 (in which SNR increases due to reasons explained in the text), the SNR falls by $\sqrt{L}$ as expected and artifact power (AP) increases. Resolution is maintained through an acceleration factor of 64, the maximum coil-based acceleration (L_c) possible from a 64-element array using conventional reconstruction techniques. Reductions in imaging time by factors greater than the number of coils can be obtained by further reducing the amount of k-space data obtained, but as this information is not replaced by coil pattern information, resolution degrades accordingly. This is evident in the lower right image, where a total reduction of 128 is obtained from a factor of 64 coil acceleration (L_c = 64) and a factor of 2 k-space reduction (L_k = 2).

Fig. 4.11 Set up for imaging at 1.5T in Würzburg, Germany. Inside the magnet room (left) showing the coil and phantom on the patient table and the preamplifiers in the foreground; outside the magnet room (right) showing 64 cables run through the scan room door, creating an unshielded environment, connected the 64-channel receiver.

responsible for both, but because of the differences in the reconstruction methods, the overlap manifests itself as two different vitiations. In anticipation of evaluating SEA imaging with the 1.5T array coil (Section III.2.4) on animal models, travel to a site with a clinical magnet was required. Collaborators at the University of Würzburg, a principle Siemens research partner in dynamic imaging, made their Siemens Vision 1.5T scanner available for testing. One week was spent integrating the 64-channel receiver into their system (see Fig. 4.11) and acquiring the first 1.5T SEA images. The images did suffer an SNR loss due to the 64 cables coming out of the magnet room, compromising the integrity of the shielded room. (This was not a problem at 4.7 T due to the integrated shield in the magnet and the fact that all cables could be grounded as they entered the magnet bore.) A new phantom was constructed, shown on the coil in Fig. 4.12, that

Fig. 4.12 Phantom on 64-channel 1.5T array coil in Würzburg, Germany.
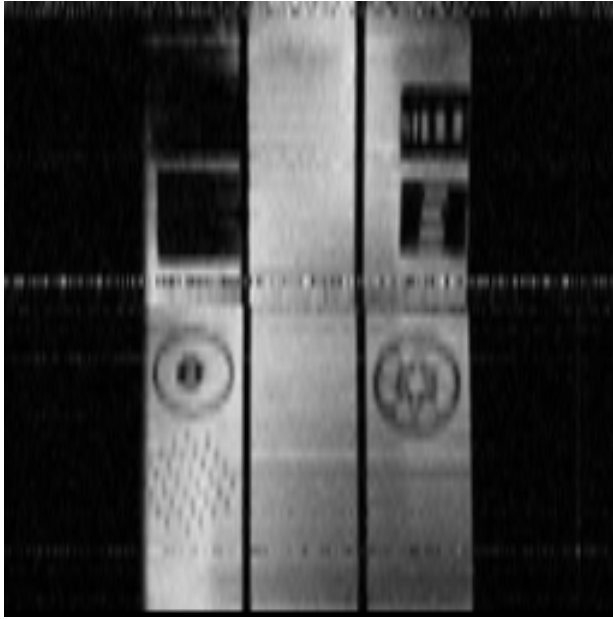
Fig. 4.13 SEA image acquired with the 1.5T 64-channel array in Würzburg, Germany. FOV was 31cm. The line of noise near the center was due to a malfunctioning preamplifier.

covered the coil and allowed for depth imaging. A representative SEA image of the phantom taken approximately 3mm off the coil is shown in Fig. 4.13. The imaging parameters were FOV 31cm, TR 500msec, TE 17msec. The line of noise in the SEA image was due to a malfunctioning preamplifier. With the larger coils, images at increasing depths were acquired, at which point an artifact similar to one observed at 4.7T was evident. This will be discussed further in the following chapter.

Once the SEA imaging procedure was disencumbered from the unrelated issues of the 4.7T system (new gradients, volume coil, and array coil), it was possible to start more clearly investigating the unusual phase effects being observed. The following section describes the effort to understand the phenomenon and the implications of it regarding applications of SEA imaging

IV.3 The Phase Compensation Gradient in Single Echo Acquisition

As previously mentioned, for all initial imaging, full data sets were collected from all 64 coils and then a single k-space line selected to form a SEA image. After it became possible to readily acquire a reliable SEA image, the first step in applying the method was to eliminate the phase encoding table and literally acquire an image with a single RF excitation and echo. Completely eliminating the phase encoding gradient, equivalent to acquiring the center (DC) line of k-space where there is typically maximum signal, resulted in very little signal received from the array however. The raw (k-space) data for a coil is simply the echo received at every phase encoding strength stacked into a 2-D matrix. Therefore, by looking at the raw data from a single coil,
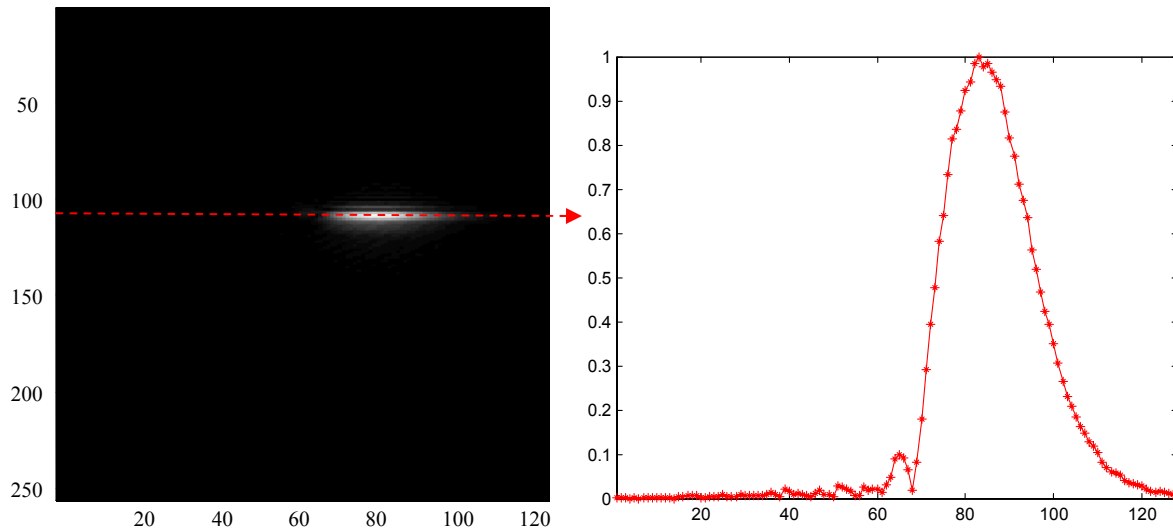
Fig. 4.14 The raw data from a single coil and the profile through it, clearly showing the signal peak offset from k=0. The 128x256 data set was obtained with image parameters FOV 14cm, TR 250msec, TE 13msec.

information regarding the signal at all phase encoding strengths can be readily observed. Figure 4.14 shows representative 128x256 raw data acquired from a single planar pair coil in the 4.7T array while imaging with a 14-cm FOV. A profile through the center of the data is also shown, indicating the signal strength at each phase encoding line. The peak signal is clearly offset from the middle of k-space, where the peak of a typical image would occur. All coils have a phase
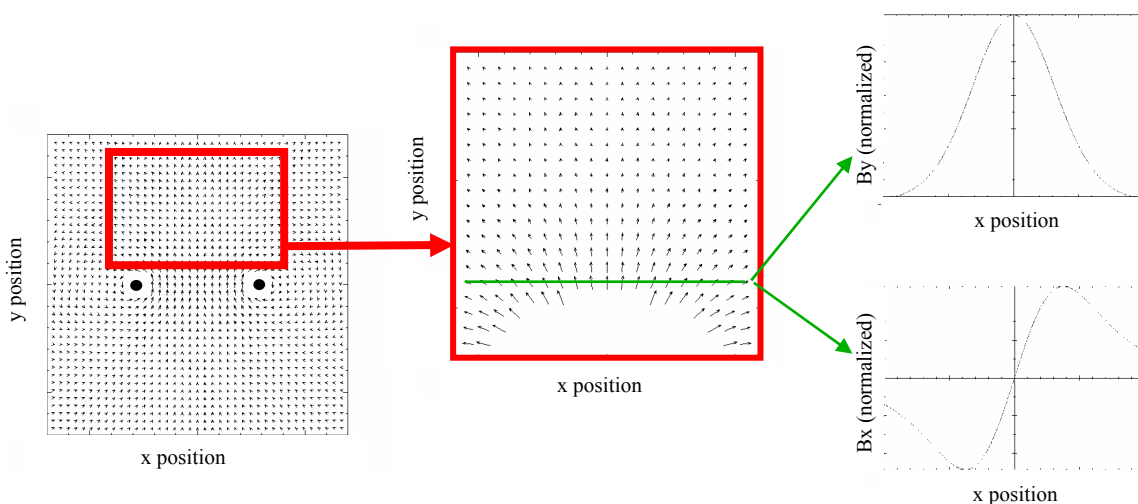
Fig. 4.15 Vector plot of the field around a loop coil (far left), enlarged in the red boxed region to clarify the magnitude (top right) and phase (bottom right) plots. When such a phase distribution occurs in a voxel, it results in signal cancellation – or an offset in k-space of the peak signal received.

across them (see Fig. 4.15 for illustration) which Jesmanowicz first observed could complicate expected signal strengths by acting as a gradient field since the phase over the sensitive region of a coil is nearly linear (77). In general, however, in the NMR experiment, the coil size is on the order of the field-of-view, with each voxel seeing essentially a uniform phase. In the case of SEA imaging, when the coil size is on the order of a voxel size, this phase variation causes signal cancellation in the voxel for which the coil is responsible (little signal at k=0) and acts as a gradient offset because of the linearity (the signal peak offset in k-space). Because of this linearity, however, the signal dephasing can be corrected by applying a predictable gradient pulse that creates an equal and opposite phase gradient across the coil. It is worth noting at this point that this need for a "phase compensation gradient" is fundamental to the SEA imaging method, resulting purely from the fact that the array coil element used, regardless of the design, must always be on the order of a voxel size and will therefore require the use of a gradient to cancel its phase.

The quasi-static Matlab model described in Section III.1 was augmented to calculate the magnitude and phase of a coil over a distance (at least six coil-widths, in general), and, given a slice offset and thickness, compute the total signal strength over that region as a function of phase compensation gradient strength. With the goal to compute and observe the compensation gradient strength that optimized the SNR for a given set of coil dimensions and FOV, the relative signal strength from the coil and a uniform phantom as a function of increasing compensation strengths was computed as the magnitude of the following equation:

$$S(\theta_{comp}) = \int_{FOV} |B_{coil}(x,y)| e^{j(\theta_{coil}(x,y)+\theta_{comp}(x))} dx dy \qquad [4.2]$$

where B_{coil} (the magnitude of the coil sensitivity) and θ_{coil} (the phase of the coil sensitivity) were calculated by the program as discussed in III.1 and the FOV for summing covered at least six coil widths. For plotting and clear notation, θ_{comp} (the phase added by the x-directed phase compensation gradient in rad/cm) was translated to its k-space line equivalent using

$$\theta_{comp} = k \cdot \Delta G_{pe} \cdot x \qquad [4.3]$$

where k ranged, for example, from –127 to 128 (just like a phase encoding table) and ΔG_{pe} was the incremental change in gradient strength per phase encoding line for a given set of sequence parameters:

$$\Delta G_{pe} = \frac{2\pi}{\gamma \cdot FOV_{pe} \cdot T_{pe}} \qquad [4.4]$$

Where gamma is the Larmor ratio, FOV_{pe} is the field-of-view in the phase encoding direction, and T_{pe} is the length [sec] of the phase encoding pulse.

To definitively compare the modeled and measured phase phenomena, sixty-four fully encoded ($256\times256=N_{phase}\times N_{freq}$) images of the 13-cm diameter spiral resolution phantom were simultaneously acquired using the 64-channel 4.7T array coil and imaging parameters TR 250msec, TE 13msec, 1 average, spectral width 50kHz, FOV 14cm. All 256 SEA images (64x256) were then reconstructed with progressing compensation gradient strengths – one from each phase encoding line. Figure 4.16 shows the excellent agreement between modeled and measured signal strength from a coil in the array at each compensation gradient strength, or k-space line. When a gradient in the same direction as the gradient impressed by the coil phase was applied (in this case, k = -127..0), there was almost total signal cancellation from dephasing in the voxel, as was seen up to point A. When a gradient opposing the direction of the coil phase was applied, the signal strength peaked and reached the optimal compensation strength (for SNR *and* resolution, discussed below), marked at point B, k=15 for this coil and sequence. Signal still existed for a time when an over-compensating pulse, such as that at point C, was applied, and, as it turns out, may provide a method to obtain high frequency resolution data, to be discussed further in the following chapter. Three of the 256 SEA images collected (corresponding to compensation strengths at points A, B, and C) with their corresponding modeled phases are shown in Fig. 4.17 (78,79). As expected, when no compensation gradient was applied, the SNR is severely degraded as the phase from each coil dephases the spins in the voxel for which it is responsible. When a gradient was applied that compensated for the phase across the coil, the optimal SEA image was obtained; and high frequency components were highlighted when an overcompensating gradient was applied.
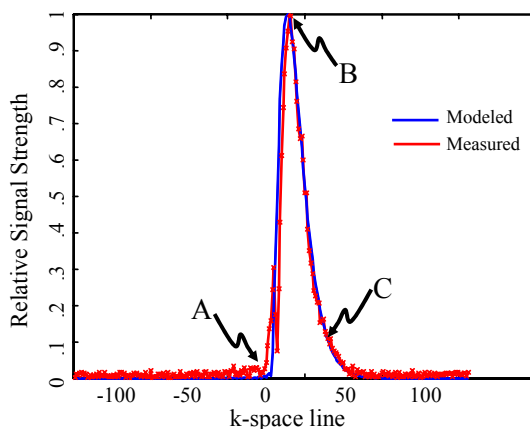
Fig. 4.16 The modeled and measured relative signal strength versus phase encoding line (k-space line), where each line represents an increase in the compensation gradient strength. Points A, B, and C correspond to the compensation strengths used to form the SEA images shown in Figure 4.17.
Reprinted with permission from (79). © 2004 IEEE
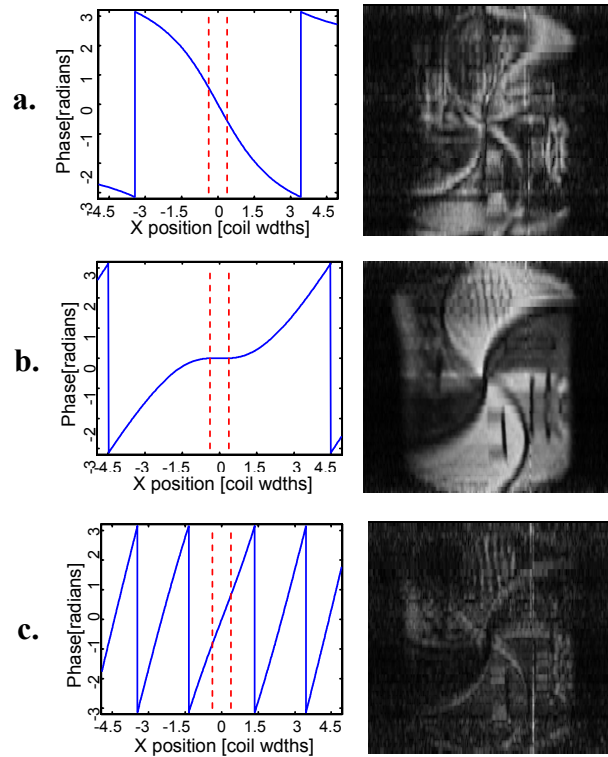
Fig. 4.17. Phase across the coil and corresponding SEA images. a) The phase across the coil (left) and a SEA image (64x256) (right) formed with k space line=0 (no compensation gradient), corresponding to point A marked in Fig. 4.16. The coil sensitivity region is marked in red. b) Phase and SEA image formed from k=15 (optimal compensation gradient applied), corresponding to point B marked in Fig. 4.16. c) Phase and SEA image with over-compensating gradient applied, highlighting the high frequency components, corresponding to point C marked in Fig. 4.16.
Reprinted with permission from (79). © 2004 IEEE

The peak point (in a plot such as that in Fig. 4.16) represents the compensation strength that produces a SEA image with optimal SNR, but not necessarily the optimal SEA image with respect also to resolution. The signal strength represents an integration of the signal over the entire sensitive region of the coil at each compensation strength. Therefore the maximum point is reached when signal is also contributed from the area surrounding the coil, which actually degrades the resolution of the SEA image. This is apparent in Fig. 4.18 where the phase of the coil with the compensation gradient that gives maximum signal is plotted (k=11 for the same imaging parameters as above). A significant portion of the signal is contributed from the area of coil sensitivity outside of the coil footprint, while there is seen to still be a phase gradient across the coil itself. With a slightly stronger gradient (k=15 discussed above), the region directly above the coil footprint is counterbalanced, simultaneously providing high SNR and resolution, as Fig. 4.17b illustrates.
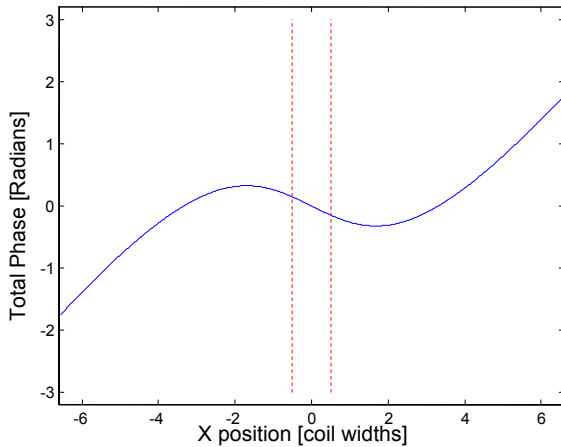
Fig. 4.18 The total phase (coil phase plus compensation gradient) across the sensitive region of the coil when the compensation gradient applied corresponds to the point of maximum signal (k=11 for this coil and sequence). A significant portion of the signal is contributed from a region outside of the coil footprint (marked in red), actually degrading the resolution of the SEA image.

The SEA sequence, then, shown in Fig. 4.19, is a modified version of a standard spin-echo or gradient-echo sequence, with the phase encoding table removed and replaced with the single phase compensation gradient pulse, specified by k-space line. In practice, a selectable option was added to the SEA sequence to allow the specification of a k-space line in order that imaging parameters could be freely changed if necessary, the echo strength observed, and the peak line selected at the console without having to re-run the modeling program. As discussed, this is not the line to form an optimal SEA image, but, when used in conjunction with modeling to predict the difference between the two lines, it does offer some flexibility to change parameters at the console.

IV.4 Summary

This chapter has presented the basic methodology of single echo acquisition imaging. This
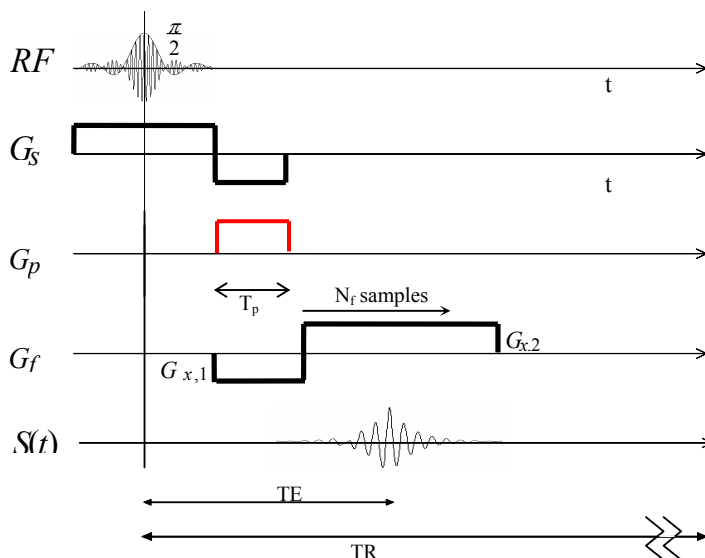
Fig 4.19 The SEA pulse sequence. A modified gradient echo sequence with the phase encoding table removed and replaced with a single "phase compensation gradient" pulse, shown in red.

was the first time that MR imaging had been performed without repeated echoes for obtaining spatial information, and represented a new imaging modality. The basic procedure/sequence, including the need for a "phase compensation" gradient, were discussed. The need for a phase compensation gradient (applied by gradients along Cartesian axes) restricts the potential of SEA imaging applications in some ways while offering unusual possibilities in other applications, a topic which will be covered in the following chapter. SEA imaging provides the potential for MR imaging at unprecedented frame rates, likely the single most important tool provided by the technique. The capability does not come without limitations, in particular the potentially confined imaging depth. Several applications of SEA imaging will be examined in the next chapter, exploring both the potential power and limits of the method.

CHAPTER V

APPLICATIONS OF SINGLE ECHO ACQUISITION IMAGING

Using arrays of parallel, narrow coils as implemented in this work, SEA imaging will be limited by a shallow penetration depth. Regardless of the element design, a coil sized comparably to a voxel dimension will never have a sensitivity suitable for SEA much more than the width of the element above it. There is a natural inclination in the field to relate clinical usefulness to the ability to image deeper in the human body – the heart, brain, etc. The coil array as it is used right now, however, is absolutely ideal for accelerating (by orders magnitude) typically very slow techniques such as large field-of-view microscopy and chemical shift imaging (or spectroscopic imaging) of surfaces, i.e. the skin, chemical sample analysis, ex-vivo tissue samples, etc. (80-84)   The method is also well-suited to simultaneous fast imaging of [moving or static] structures in small animals (multiple mouse hearts, for example, where simultaneous cardiac gating to each mouse is not possible) (85-87). Assuming, then, that there are many specific applications to which SEA could be applied, this chapter attempts to answer broad questions regarding the implementation of SEA in several application areas.

The first section discusses the first and most obvious manner in which SEA can be used – for single slice imaging, as was discussed in the previous chapter. The questions that naturally follow then, pertain to the depth to which this is a plausible application and the degree to which the resolution of the technique is limited. Two factors that will influence the effective depth for SEA imaging are examined: the variation of the coil phase gradient as well as an interesting artifact in the coil pattern. Resolution enhancement techniques that are particularly compatible with the SEA method are presented to conclude the section. Since the speed of the method is its primary unique capability, examining the more time-intensive (because of their need to acquire very large data matrices) MR applications with respect to SEA is the focus of the following two sections. The second section discusses the possibility of implementing multi-slice and/or 3D imaging using the SEA method, both of which are time-consuming due to their need to fill matrices in three dimensions.   The third section examines accelerating large field-of-view microscopy, a very promising dedicated application for the array coil.   The fourth section examines the question of whether or not SEA is restricted to being a planar method. The very interesting possibility of conforming a flexible array for SEA imaging to a surface or even around a cylinder to allow the possibility of volume and/or catheter imaging is examined, and

the final section presents perhaps the most exciting application of SEA imaging – the ability to obtain MR images at extremely high frame rates. Initial results are shown demonstrating SEA movies at 125 frames/sec., already the fastest MR images yet obtained by nearly an order of magnitude.

V.1 Single Slice SEA Imaging

The previous chapter discussed in detail this new method of MR imaging, which can be considered SEA imaging in its most basic form. An $N_c x N_f$ (number of coils x number of frequency encoding points) image is made of a slice parallel to the plane of the array in the time it takes to acquire a single echo. The basic method is a building block that can be applied to other MR techniques, as will be discussed in the rest of this chapter, but only after examining its limitations (in penetration depth and resolution) as a stand-alone tool. Until now, SEA imaging has been discussed insofar as its ability to be a feasible imaging method. To that end, the SEA images presented thus far have been acquired very close to the array, in the region known to be optimal. While imaging in this region is reasonable for certain surface imaging applications such as skin imaging, for other applications such as dynamic contrast enhanced (DCE) MRI, it will be necessary to image at deeper depths. This is complicated not only by the field fall-off of the coils (discussed in III.4.2) which results in a natural SNR and resolution loss, but also by the fact that the optimal phase compensation gradient (discussed in IV.3) changes with the distance from the coil.

V.1.1 Penetration Depth Considerations in Single Slice SEA Imaging

To study the necessary phase compensation considerations when applying SEA with various imaging parameters, the quasi-static Matlab modeling program that has been used throughout this work was modified to include the option of varying the slice thickness and slice offset from the coil (see Fig. 5.1 for illustration). The signal (for a given coil geometry) from the chosen
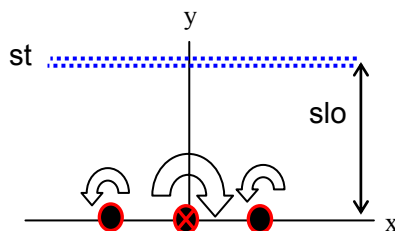
Fig. 5.1 Illustration of slice location and thickness used when implementing the quasi-static Matlab model. The field lines around the three wires of a planar pair coil are shown along with the slice-offset (slo) location and slice thickness (st) over which the signal is integrated.
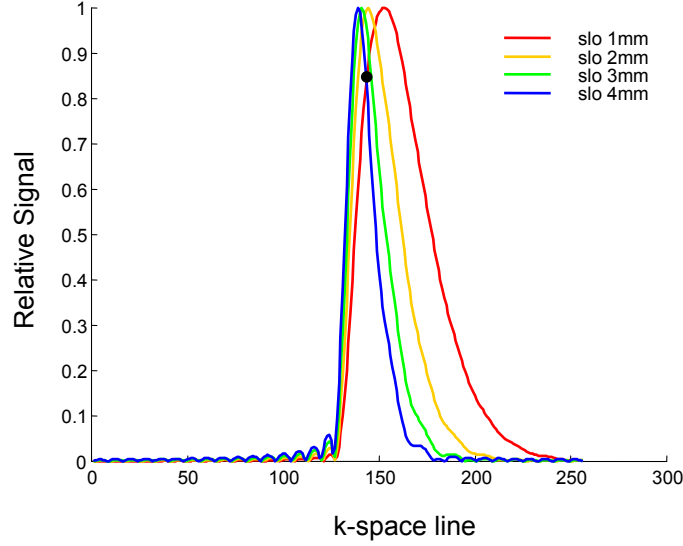
Fig. 5.2 Modeled relative signal strength acquired from a 2mm slice vs. k-space line, or compensation gradient strength, for four slices moving away from the coil. SLO=1mm corresponds to a slice offset 1mm off the coil and requires the strongest compensation gradient (peak the farthest out in k-space) and slo=4mm corresponds to a slice-offset 4mm from the coil and requires the weakest compensation. The black mark indicates a "compromise point", where the two signal lines intersect.

slice was then calculated using the following equation:

$$S(\theta_{comp}) = \int\limits_{sloFOVx}^{slo+st} \int |B_{coil}(x,y)| e^{j(\theta_{coil}(x,y)+\theta_{comp}(x))} dxdy \qquad [5.1]$$

Then, as before, the phase compensation gradient strength, $\theta_{comp,}$ was converted to its k-space line equivalent, discussed in detail in IV.3. The results of the modeling are shown in Fig. 5.2, indicating the difference in optimal k-space line for varying distances, or slice offsets, from the coil, with the slice thickness set at 2mm. As expected, when moving away from the coil, a weaker compensation gradient necessary (the peak occurred at a lower line in k-space). Over a slice offset that varied from 1mm off the coil to 4mm off the coil, the k-space line to obtain the maximum signal moved from k=153 to k=139. This implies that when imaging at various depths, the compensation gradient strength either needs to be changed for each depth (which would only be possible if a multi-slice sequence was modified) or a compromise point should be selected, as is marked at k=143 in Fig. 5.2. The "optimal" compromise point occurs where the signal curve for the slice closest to the coil intersects the signal curve for the slice furthest from the coil. Table 5.1 summarizes the penalty in signal strength at each slice offset at the "compromise point" vs. the maximum point, but also tabulates the signal loss due to the field fall-off from the coil. It is quickly apparent that the loss due to choosing a non-optimal

Table 5.1 Summary of Signal Loss at Different Slice Offsets Due to Compromise
Choice of Compensation Gradient

SLICE OFFSET FROM COIL	RELATIVE SIGNAL COMPROMISE POINT	RELATIVE SIGNAL AT MAXIMUM	TOTAL SIGNAL (COMPROMISE LOSS· FIELD STRENGTH LOSS)
1mm	0.85	1.00	0.85
2mm	0.99	0.46	0.46
3mm	0.96	0.26	0.25
4mm	0.85	0.17	0.14

compensation gradient is small compared to the loss inherent to simply moving away from the coil.

Measured data to corroborate the model was obtained from the k-space data from a single coil in the 64-channel 4.7T array at varying slice-offsets with a slice thickness of 2mm. Figure 5.3 shows the measured and modeled data, aligned vertically with a green dashed reference line to make the shift in the peak location more visible. The models and measurements agree well with the exception of the significant amount of signal that rises at the center of k-space as the distance from the coil increases.

To study the phenomenon, another set of single-coil images were made with the slice thickness set to 2mm and the slice offset varying from 1mm to 8mm. Figure 5.4a-b shows the images, the k-space data from each image, and a profile through the center of k-space (equivalent to the plots shown in Fig. 5.3) for each of the eight slices. As the offset from the coil increased, a dark strip grew over the half of the coil closest to the feed and simultaneously, spurious bands of signal became visible on either side of the dark strip. This corresponded to the signal peak rising at the center of k-space until it overwhelmed the signal peak due to the coil. Signal at the center of k-space results when there is no phase offset. Therefore, it was initially assumed that, the artifact was caused by coupling to the transmit coil in some way since a volume coil does not have a phase offset. To verify that the peak that rose at the center of k-space was signal corresponding to the two artifact bands, a Matlab program was written to allow a region of k-space to be interactively masked by the user, and a new image formed from the modified k-space data. Example results are shown in Fig. 5.5 for a slice corresponding to a 5mm slice offset. Matching intuition, when the signal peak at the center of k-space was masked, only the "correct" signal from the coil remained – the strip of signal over the end of the coil. When
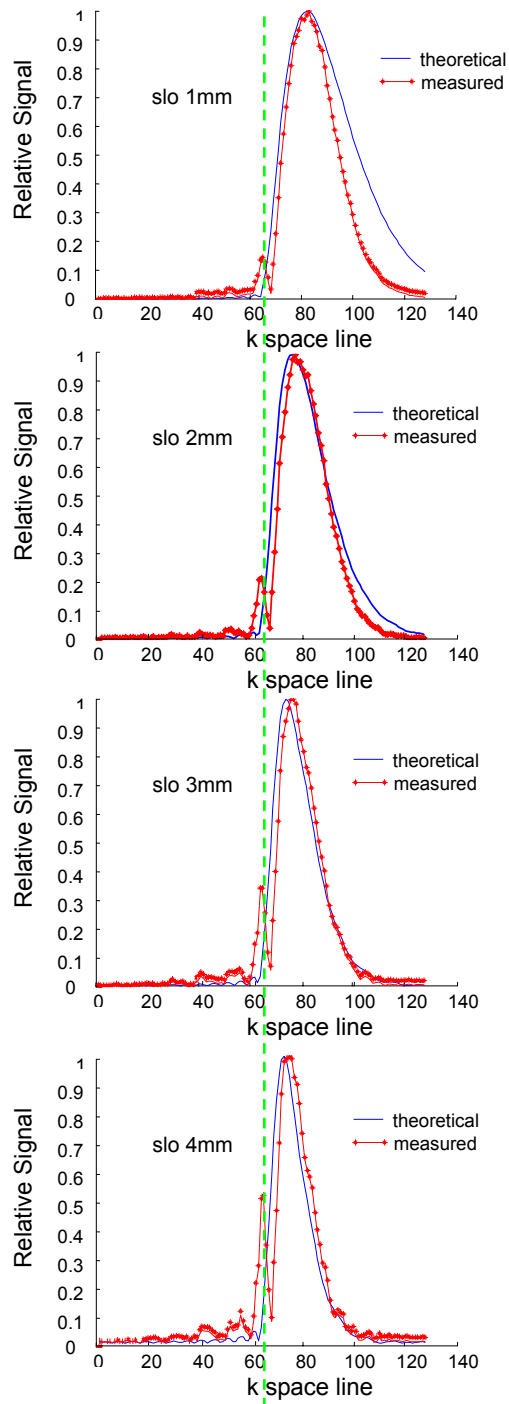
Fig. 5.3 Modeled and measured relative signal vs. k-space line for slice offsets varying from 1mm to 4mm off the coil. The figures are aligned vertically with the green dashed reference line to make the shift in the peak signal more visible. The data agree well with the exception of the significant amount of signal that rises at the center of k-space as the distance from the coil increases, discussed further in the text.

the k-space data presumably from the coil was masked, leaving only the data at the center of k-space, the two artifact bands were all that were formed in the image. The source of the artifact was still unclear, however, in particular why the artifact began at one end (the feed end) of the coil and gradually extended towards the other end as the depth was increased. Additionally perplexing was the fact that the exact same artifact was seen when using the 1.5T array on MR
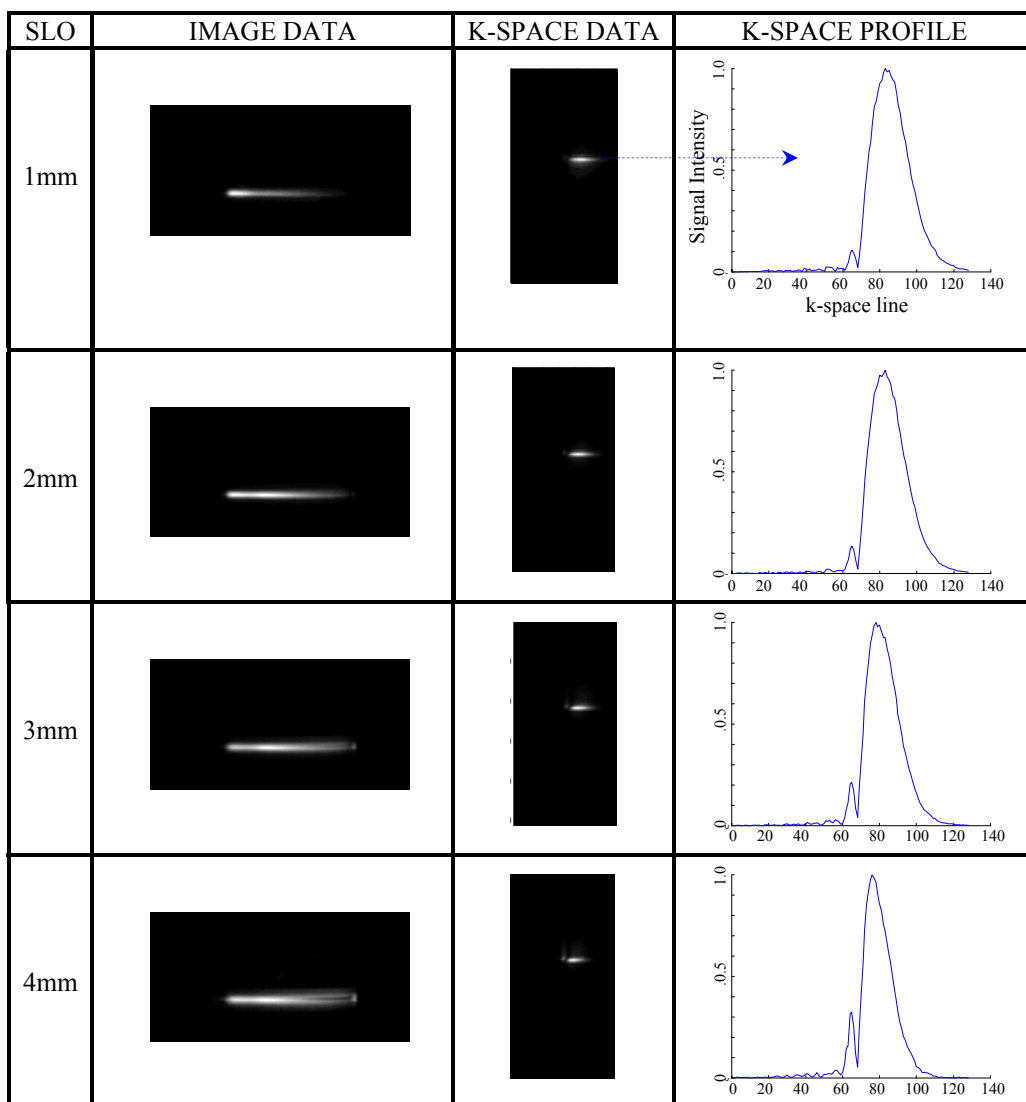
Fig. 5.4a Image data, k-space data, and profile through the k-space data from a single coil in the 64-channel 4.7T array as the slice offset from the coil is increased from 1mm to 4mm. The artifact characterized by a dark line in the center of the coil and two bands of signal on either side is accompanied by the peak rising at the center of k-space as the distance from the coil is increased.

SLO	IMAGE DATA	K-SPACE DATA	K-SPACE PROFILE
5mm			
6mm			
7mm			
8mm			
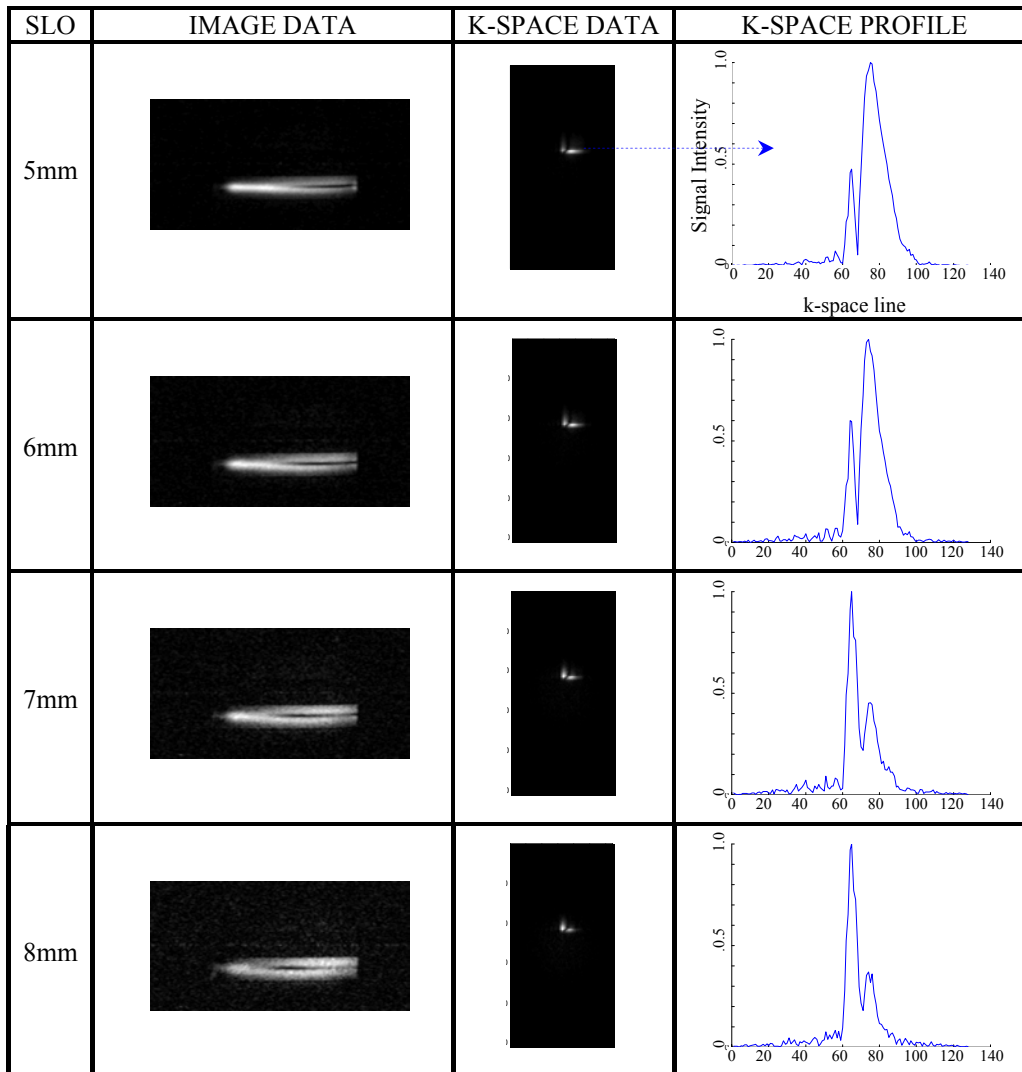
Fig. 5.4b Image data, k-space data, and profile through the k-space data from a single coil in the 64-channel 4.7T array as the slice offset from the coil is increased from 5mm to 8mm. As the depth is increased, the artifact characteristics become increasingly pronounced until the dark line covers the entire coil, the spurious bands of signal on either side of the coil extend over the entire length, and the peak at the center of k-space has overwhelmed the peak from the true coil data.

systems in Würzburg, Germany and at M.D. Anderson Cancer Center in Houston. Both of these systems use quadrature transmit coils, while the transmit coil in the MRSL is a linear coil. The fact that the artifact was seen regardless of array element footprint, transmit coil configuration, and operating frequency raised the possibility that the artifact was actually due to the currents on the coils and not system interaction. An effort was made to measure the magnitude and phase of the currents on the coil using a small magnetic field pick-up probe and an S_{21} measurement on
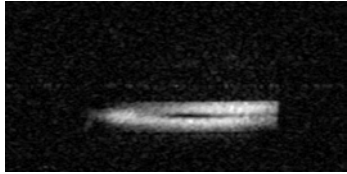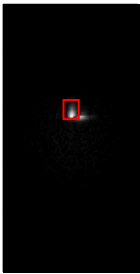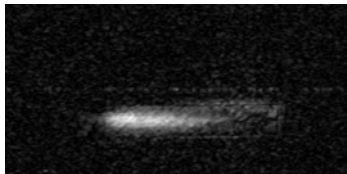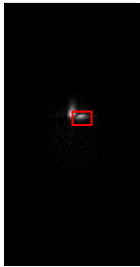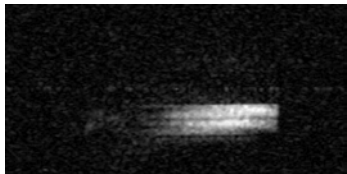
	K-SPACE DATA	RESULTING IMAGE
UNADJUSTED K-SPACE DATA		
MASKED ARTIFACT PEAK AT CENTER OF K-SPACE (IN RED)		
MASKED "CORRECT" PEAK OFFSET IN K-SPACE (IN RED)		

Fig. 5.5 Masking k-space data for SLO=5mm (see Fig.5.4b) to verify that the peak that rises in the center of k-space corresponds to the two artifact bands that appear at the feed end of the coil as the imaging depth increases. When the center peak is masked out (middle row, center column), the image that results is the expected strip of signal over the coil at the end farthest from the feed (middle row, right column). When the k-space data corresponding to expected coil signal was masked (bottom center), only the artifact remained (bottom right).

the network analyzer. Due to the necessarily small size of the probe, it was not possible to shield it, causing stray effects to make the measurement very sensitive to cable position. Therefore, while some variations in currents were seen, the measurements were small compared the change that could be induced by simply moving the cables. Since the measurements were inconclusive,

the full-wave program previously used to study coupling between coils was used to model the complex currents on the three legs of the coil and the resulting field intensity at various heights above the coil.

The coil footprint of the 4.7T array element was modeled at 200MHz over a substrate with relative dielectric constant of 4.6 (for G10) with a thin layer of plastic (ε_r=2.2) and water above it to simulate the phantom. The computed currents in the three legs at the feed end and the far end are shown in Table 5.2. There is a small but noticeable increase in the magnitude and phase of the currents from the feed end to the far end, a common sign of a standing wave effect. With these currents on the legs, the field intensity (showing the magnitude of the field) at varying heights above the coil and the phase of the field across the coil at both ends were calculated and are shown in Fig. 5.6. The intensity images showed that the artifact did indeed appear as the depth was increased, with a null forming in the center of the coil and bands of signal rising on the outsides. The phase ramp across the coil at the far end of the coil behaved as expected, decreasing with distance from the coil and remaining approximately 90 degrees directly above the coil. The phase across the coil at the feed end began to show unexpected behavior at a 5mm offset and a phase reversal at 7mm. The implications of this behavior regarding SEA imaging are affected by the fact that a compensation gradient is used during SEA imaging at a strength that counterbalances the phase at the properly behaving end of the coil. Since the phase at the feed end of the coil reverses with height, the compensation gradient actually adds to the phase of the coil instead of canceling it, causing dephasing and signal loss – already a problem because of the artifact null in the magnitude that exists. Because the bands of signal that rise on the sides of the coil at the feed end correspond to signal rising at k=0, their source must necessarily be in the region where the phase briefly flattens on either side of the coil. With a phase compensation gradient on, the signal from the bands is presumably dephased and does not have a significant effect the SEA image. SEA images ranging from depths of 1mm off the coil to 5mm off the coil are shown in Fig. 5.7. The effect of the artifact is evident by 3mm off the coil (over a coil width)

Table 5.2 Modeled Leg Currents on the Three Legs of a Planar Pair at 200MHz

LEG CURRENTS	OUTSIDE LEG 1	CENTER LEG	OUTSIDE LEG 2
Magnitude (feed end)	2.508	4.933	2.508
Phase (feed end	-88.717	91.323	-88.717
Magnitude (far end)	3.112	6.215	3.112
Phase (far end)	-89.496	90.514	-89.496

FIELD INTENSITY	PHASE ACROSS COIL AT FEED END (POINT 1)	PHASE ACROSS COIL AT FAR END (POINT 2)
SLO 3mm		
SLO 5mm		
SLO 7mm		
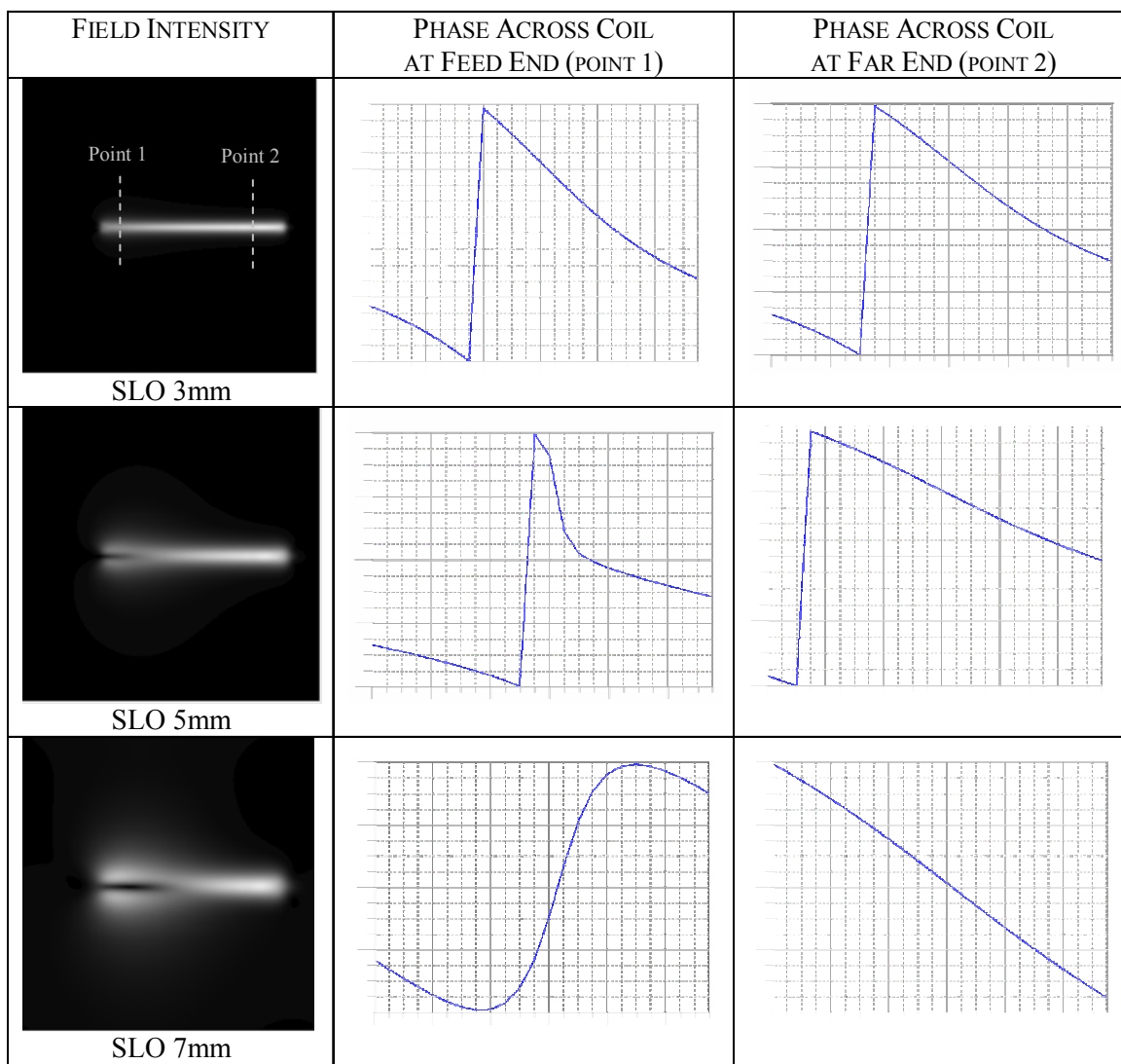
Fig. 5.6 Modeled field intensity and phase of the field across the coil at two points (labeled at top) for increasing slice offset from the coil. The artifact of interest, seen at the feed end, manifests itself as a null that grows up the center of the coil and two side bands of signal.   The corresponding phase (across point 1) reverses from the expected behavior (across point 2).

by the shading in the half of the image closest to the feed.

Upon closer examination of the current values, it was noticed that, while there was a variation from one end of the coil to the other, the relative strengths of the currents at both ends were correct – i.e. the center leg was twice the magnitude and 180 degrees out of phase from the outer legs. Therefore, to examine whether the artifact was due not to the currents, but to a propagation effect in the lossy media, the same coil footprint was modeled at 2MHz. The

| SLO 1mm | SLO 3mm | SLO 5mm | SLO7mm |
| ½ coil width | 1.5 coil widths | 2.5 coil widths | 3.5 coil widths |
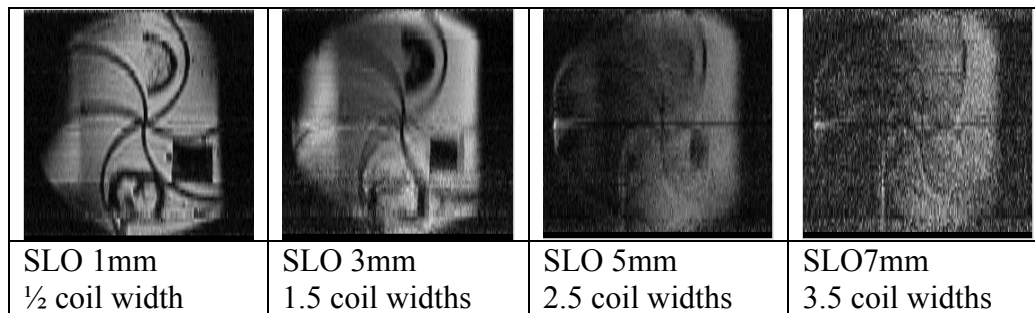
Fig. 5.7 SEA images at increasing distances from the coil. The full wave artifact discussed in the text is evident in the images formed at a distance greater than a coil width away from the shading on the left half of the images (the side closest the feed end of the coils).

modeled currents at 2MHz are shown in Table 5.3 and are seen to be highly uniform over the coil legs. The 2MHz currents propagated at 200MHz did not produce the artifact and the 200MHz currents propagated at 2MHz did produce the artifact, confirming that the undesired field pattern is due to an improper current distribution on the legs of the coil.

Thus far, the images including the artifact have been in the coronal plane. The normalization of an image in that plane perhaps makes the artifact appear more significant or dramatic than it actually is. Figure 5.8 shows an axial image through the coil at the feed end and the far end, corresponding to point 1 and point 2 labeled in Fig. 5.6. The axial images are windowed so that the null associated with the artifact is visible and it is apparent the artifact does not appear until a region of very low SNR that would not be used for most applications. The artifact is not insignificant, however, and future work will include correcting the current distribution, as will be discussed in the following chapter.

V.1.2 Resolution Enhancement in Single Slice SEA Imaging

In addition to a characteristic shallow penetration depth, SEA is also an imaging method

Table 5.3 Modeled Leg Currents on the Three Legs of a Planar Pair at 2MHz

LEG CURRENTS	OUTSIDE LEG 1	CENTER LEG	OUTSIDE LEG 2
Magnitude (feed end)	2.872	5.745	2.872
Phase (feed end)	-82.522	97.466	-82.522
Magnitude (far end)	2.872	5.745	2.872
Phase (far end)	-82.534	97.466	-82.534
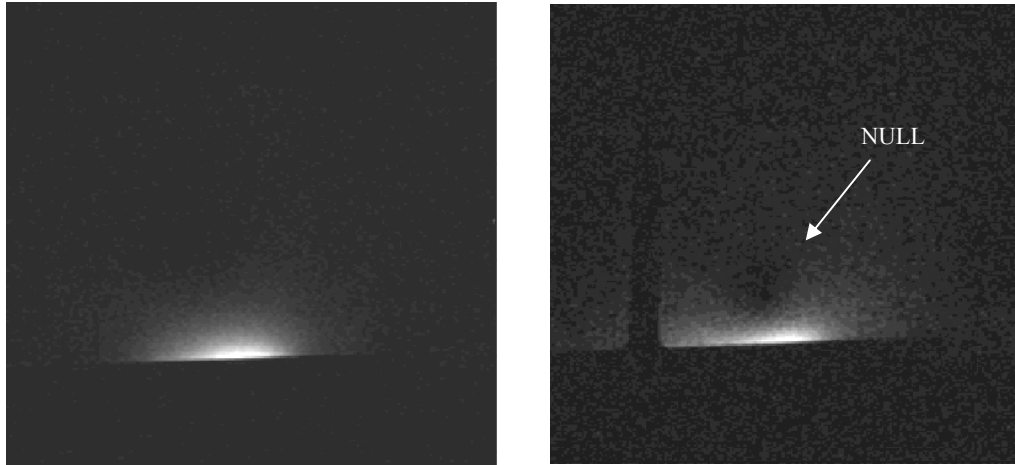
Fig. 5.8 Axial images taken across the far end (left) and the feed end (right) of a coil at 4.7T, corresponding to point 1 and point 2 labeled in Fig. 5.7. The images are windowed so that it can be seen that the artifactual null that appears in the center of the coil as the distance from the array increases is seen to exist only in a region of very low SNR. The dark line on the left of the image at the feed end is due to a feature in the phantom, not the field pattern.

whose resolution is determined by the size of the sensor used – ideal for imaging speed, but not necessarily for resolution. In common practice, the resolution of an image is often somewhat loosely specified as the field of view in a given direction divided by the number of samples in that direction. More accurately, the spatial resolution of an imaging method is defined most basically as the smallest resolvable distance between two objects. Alternatively, it can be measured as the full-width-half-maximum of the point spread function (1). A method to rigorously measure resolution has not been employed to analyze SEA images, however funding is in place to thoroughly characterize the imaging method, including with respect to resolution. Meanwhile, the resolution has been qualitatively compared to fully encoded images of varying resolutions (see Fig. 5.9), with profiles showing the ability to resolve a 1.6-mm wide null. The resolution in SEA imaging is ultimately determined by the field sensitivity of the array element used. The compensation gradient chosen does affect the resolution, but, at best (with no post-acquisition enhancement), the resolution would be expected to be equal to the coil width, comparable to that of an encoded 64x256 image over the same FOV, remembering that the SEA image was formed 64 times faster. The image comparisons in this work have been and will be typically made to 128x256 and/or 256x256 images, however, simply because those resolutions are clinically standard and useful. Therefore, while the primary capability of SEA imaging is its speed, it is appropriate to consider certain resolution enhancement techniques that can be readily applied to the SEA method while maintaining its speed.
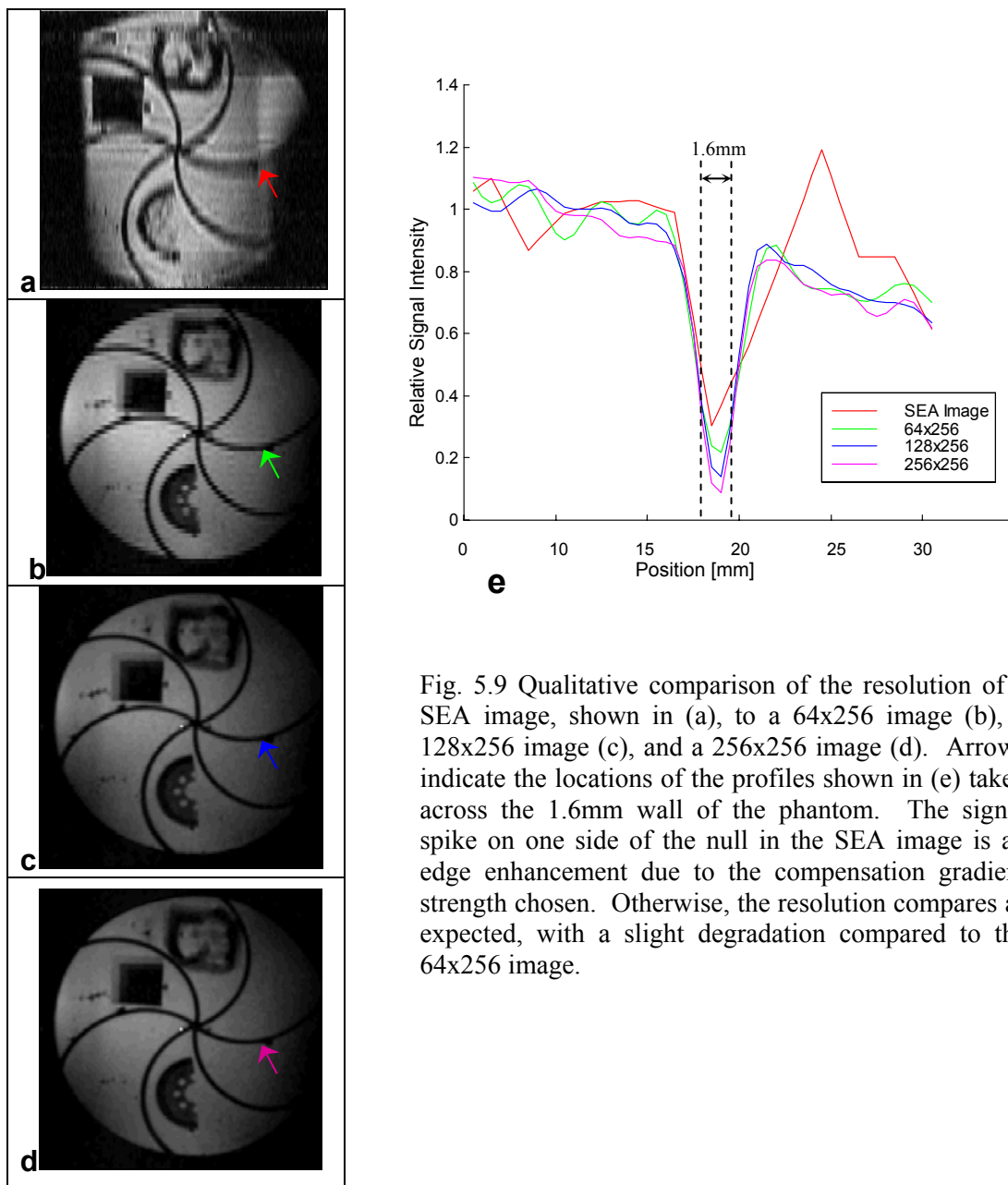
Fig. 5.9 Qualitative comparison of the resolution of a SEA image, shown in (a), to a 64x256 image (b), a 128x256 image (c), and a 256x256 image (d). Arrows indicate the locations of the profiles shown in (e) taken across the 1.6mm wall of the phantom. The signal spike on one side of the null in the SEA image is an edge enhancement due to the compensation gradient strength chosen. Otherwise, the resolution compares as expected, with a slight degradation compared to the 64x256 image.

"Segmented k-space" techniques, commonly used in dynamic MR imaging, provide high effective frame rates by acquiring only a segment of new k-space data every TR (repetition time) and presenting an updated image based on a combination of old and new k-space data (88,89). There is a temporal blurring dependent on the number of acquisitions required to fully update k-space, but spatial resolution is maintained. This "sliding window" technique is very compatible with the SEA imaging method, as echoes using two different compensation strengths (one

emphasizing signal and one emphasizing resolution – mentioned in section IV.3) can be successively acquired and combined to achieve images at a higher resolution than usual SEA images while maintaining a frame rate of one image every echo.

To test the technique and study the effects of combining various lines of k-space, sixty-four 256x256 fully encoded images, TR/TE = 250/15msec, FOV=13cm, were simultaneously acquired using the 4.7T array and the 64 channel receiver. Images combining an "even" and an "odd" echo were then analyzed with respect to artifact power and signal-to-noise ratio. The "odd" echo was always acquired with the optimal compensation gradient that canceled the phase across the coil, as was discussed in Section IV.3. The SNR and artifact power of the combined image, then, were analyzed as a function of k-space line chosen for the "even" echo. The results are shown in Fig. 5.10 (90). In this case, the optimal compensation gradient was at k=141. Therefore, As expected, the SNR dropped to approximately 70% when phase offsets producing no signal were added (k = 0 to 128). When phase offsets immediately adjacent to line 141 were used, the SNR increased up to a factor of 1.41 as the signal was approximately the same but the noise was uncorrelated. When line 141 exactly was added, there was a drop in the SNR as identical data was added. The artifact power, defined more fully in Section IV.2, describes the
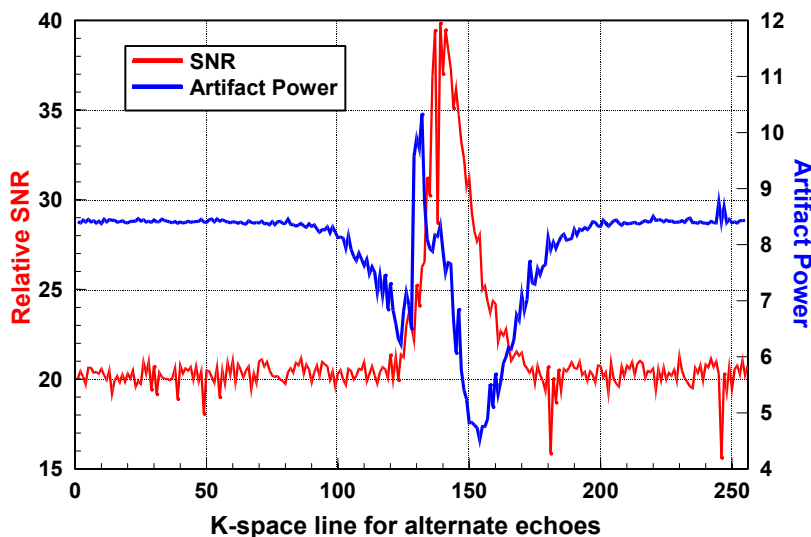
Fig. 5.10 SNR and artifact power in an image made from two echoes as a function of the k-space line selected for the second echo. The first echo was formed with the optimal gradient compensation strength, discussed in IV.3, k=141 in this case. The SNR behaves as expected, as is discussed in the text. The artifact power has two minimums: one corresponding to the phase of the coil adding resolution information and one corresponding to the selection of a k-space line that provided optimal resolution information for this particular phantom.
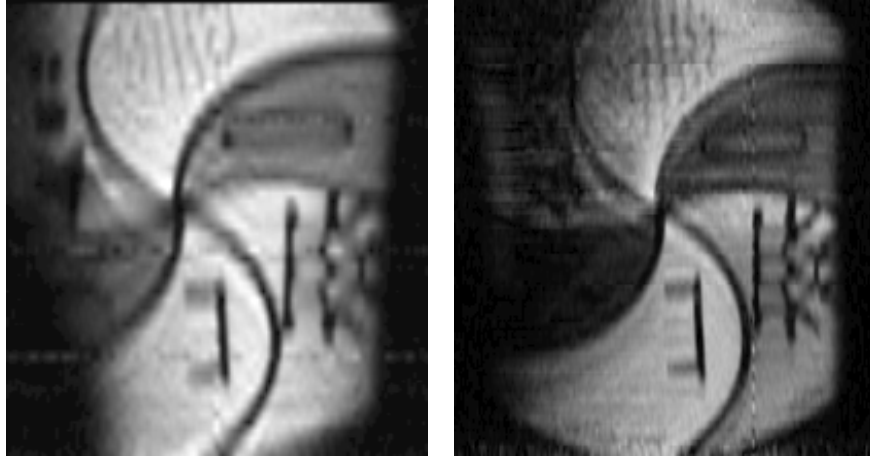
Fig. 5.11 True SEA image (left), made from a single echo at k-space line=141 and a resolution enhanced image (right), made from combining two echoes, one at line 141 and one at line 156. The pin cushion and line definitions on structures are clearly improved, and an acceleration factor of 32 over encoding a 64x256 image was obtained.

degradation of the image, with higher numbers indicating a poorer image, usually with respect to aliasing and resolution. The first minimum in the artifact power occurs at k=128 – the center line of k-space, with no phase compensation gradient. This is where resolution is maximally enhanced due to the phase across the coil – right before the compensation gradient changes directions and begins to offset the phase of the coil. The next minimum occurs at k=156 and represents the optimal k-space line to use to create a resolution-enhanced image. It represents the gradient strength that enhances the phase of the coil to the point of optimally resolving the features of the given phantom. A true SEA image (made from a single echo at k=141) and a resolution enhanced image (made from 2 echoes at line 141 and 156) are shown in Fig. 5.11. The resolution in the frequency encoding direction was basically unchanged, but the pin-cushion feature and the definition of the other three visible structures were visibly improved in the phase encoding direction by adding an echo. The extremely high frame rates associated with SEA can be maintained, then, while improving the resolution. Other resolution enhancement techniques, including deconvolution methods and specialized SENSE reconstructions, are also compatible with SEA imaging and will be examined as future work and discussed further in the following chapter.

V.2 Using SEA in Three Dimensions

Three dimensional MR images are most commonly formed in one of two basic ways, depending on the application. Multi-slice MRI is simply two-dimensional MRI – with frequency encoding, phase encoding, and standard slice selection gradients – repeated for various slice offsets. True isotropic resolution, however, is obtained in 3D-MRI scans, in which a thick slice is selected with every excitation and phase encoding is actually performed in the depth direction. Both methods are time-consuming due to filling three dimensional data matrices, and both would benefit temporally from eliminating phase encoding in one direction.

Because the optimal phase compensation gradient changes with depth (discussed in Section V.1.1), multi-slice methods offer the benefit of highest-quality SEA imaging with every slice, since the compensation gradient can be changed with every slice selection. The set of SEA images formed at progressing depths shown in Fig. 5.7 represents the basic usefulness of such a multi-slice data set, with the only difference being that the implementation was not with a multi-slice sequence. Because SEA has such a small effective imaging region in the depth direction, gaining practical information (new information with each slice) in that dimension requires the phase encoding of 3D methods in order to distinguish the feature differences between very thin slices. The disadvantage of 3D-MRI implemented using SEA lies in the fact that a single compensation strength must be chosen for the entire phase encoded slab and therefore not every image in the set will be optimal. As was previously discussed, it is possible to form SEA images at different depths with the same compensation gradient strength without too great a signal loss for any given slice (see Fig. 5.2). To implement 3D-SEA, it is also necessary to examine the effect of the slice thickness on the optimal compensation gradient. Using the same quasi-static
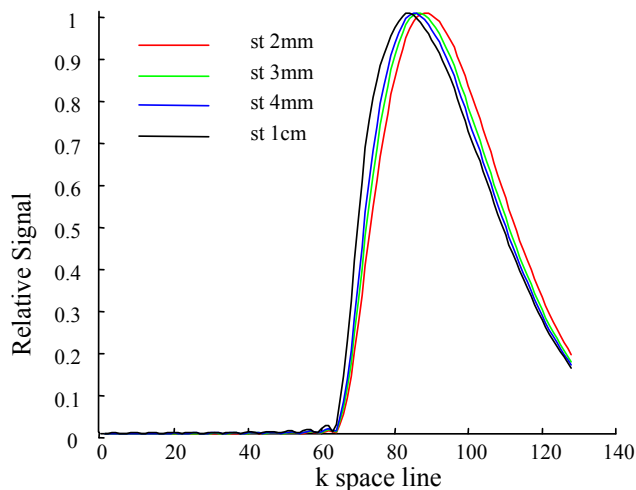

Fig. 5.12 Effect of slice thickness on choice of gradient compensation strength. The majority of the signal in SEA imaging is contributed from the first few millimeters. Therefore increasing slice thickness has little effect on the choice of compensation strength chosen.

program used throughout this work, the slice thickness was varied and the signal level calculated for each compensation gradient strength, or k-space line. Figure 5.12 shows the results. For a slice thickness that varied from 2mm to 1cm (changing the slice offset to keep the bottom of the slice directly over the coil) the difference in compensation strength was only five k-space lines. This is simply due to the fact that the majority of the signal is in the first few millimeters of the slab. While the thickness of the slab per se might not be the factor necessary to consider when selecting the compensation strength for 3D-SEA, the variation in phase from the top to the bottom of the slab does affect the compensation gradient strength enough to develop a standard method of implementation. In practice, if implementing true 3D-SEA with only a single echo received from each coil for each slice encoding line, the compromise k-space line would need to be pre-selected. The most logical approach is to find the compensation strength intersection point from the top of the slab and bottom of the slab. The selectable option in the SEA sequence that allows the k-space line to be changed and signal strength observed can be used to track the signal strength of the farthest slice as the k-space line is increased from its optimal value and the strength of the closest slice as the k-space line is decreased from its optimal value. The k-space line where the two have equal signal strengths represents the compromise point discussed in section V.1.1 and shown in Fig. 5.2. This procedure is complicated, however, by the fact that the resolution of a 3D image in the slice encoding direction will be much smaller than the smallest allowable slice thickness on an imaging system. The Matlab modeling program was used to verify that with the 3D testing parameters used and discussed below, a standard slice thickness could be used to reasonably indicate the intersection point of slice encoded slice thicknesses. Fig. 5.13 shows the results, with the intersection points specifying the compromise compensation strength from the top of the slab excited (5mm offset) and the bottom (1mm offset), when 16 slice encoding lines are used across the slab and 64 phase encoding lines are used. The compromise gradient strength occurred at k=47 for ¼ mm slice thicknesses (slice encoding equivalent thickness) and at k=43 for 2mm slice thicknesses (thickness used in practice to pre-determine the compensation strength). The difference was minimal, equivalent to a difference that could be caused by a shift in shim.

The same method in which SEA was first tested was applied to the testing of 3D-SEA: acquire fully encoded data sets from all coils to study the effects of phase (and slice, in this case) encoding. A microscopy/3D-SEA phantom was constructed in a 13cm dish containing spiraled compartments filled with 1g/L $CuSO_4$, as before. The 3D structures were ¼ mm thick stacked letters S-E-A-M-R-I and five 1mm thick stacked squares of progressively decreasing size. The standard 3D sequence on the 4.7T Omega in the MRSL was used to collect fully encoded 3D
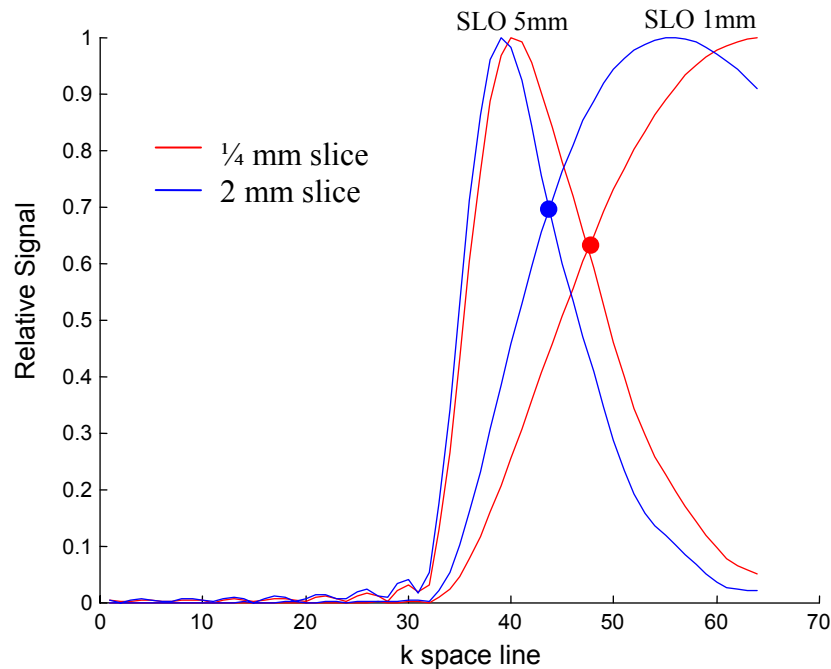
Fig. 5.13 Compromise compensation gradient strengths for a slice 1mm off the coil and a slice 5mm off the coil for two slice thicknesses: a ¼ mm slice (red intersection point at k=47) and a standard 2mm slice thickness (blue intersection point at k=43). The fact that they are close means that a standard slice thickness can be used in practice to effectively set the compromise strength for 3D-SEA.

data sets from all 64 coils simultaneously, where each set was *64 x 128 x 32 = N_{pe} x N_f x N_{se} = phase encoding x frequency encoding x slice encoding resolution*. It is standard procedure when 3D imaging to slice encode over approximately twice the slab thickness to prevent aliasing into the slices of interest. A 4mm slab was excited within an 8mm FOV that was phase encoded with 32 steps. The excited slab extended from a slice offset 1mm off the coil to 5mm off the coil, with 16 slice encoding lines through it. The effective resolution in the slice encoding direction, then, was 0.25mm.   To test using a standard slice thickness to select the compromise compensation strength, the signal strength vs. compensation gradient was measured for a 2mm thick slice 1mm off the coil and a slice 5mm off the coil. The results are shown in Fig. 5.14a-b, but were not as straightforward as would have been hoped due to the depth artifact discussed in V.1.1. The k-space data for a slice 5mm off the coil was so overwhelmed by the presence of the artifactual signal peak at the center of k-space that the intersection with the slice 1mm off the coil was meaningless, as Fig. 5.14a indicates. In order to at least verify the modeling, the artifact peaks (on both slices) were zeroed out and the curves renormalized, shown in Fig. 5.14b. The intersection point then falls at k=42.5, matching the model in the prediction for the compensation
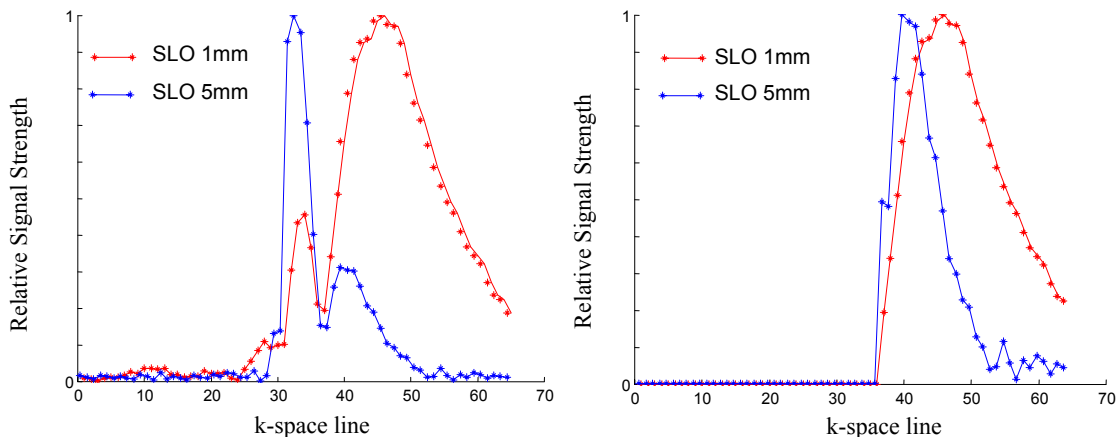
Fig. 5.14 Effect of artifact on choosing compromise compensation gradient. a) The measured signal strength vs. k-space line for a slice 1mm off the coil and 5mm off the coil. The artifactual peak that occurs at the center of k-space (discussed in V.1.1) overwhelms the coil peak for SLO=5mm. b) the measured signal strength vs. k-space line with the half of k-space containing the artifactual peak zeroed out and the curves re-normalized. The intersection then occurs at k=42.5, corresponding to the modeled prediction shown in Fig. 5.12 for a 2mm slice thickness.

gradient strength to provide overall optimal SEA images for the 16 slices in the slab. Four 3D-SEA images corresponding to slice offsets at 1.5mm, 2.5mm, 3.5mm, and 4.5mm, all formed using the compensation strength corresponding to k=43, are shown in Fig. 5.15a-d. For comparative purposes, the same slices are also shown in Fig. 5.15e-h, formed with different compensation strengths chosen for optimal quality (judged visually) in each slice. While some features were more visible in the "optimal" images, overall, the compromise compensation strength chosen with the modeling guidance seemed to be a good choice. For reference, all 16 conventionally phase encoded slices through the slab acquired with the volume coil are shown in Fig. 5.16. This set was acquired in 34 minutes with a TR of 1sec (long for signal) and TE of 20 msec. The SEA images were formed using only 32 lines of k-space (one phase encode line per 32 slice encode lines), representing a time savings of a factor of 64. Because of the ability of SEA to so dramatically decrease the imaging time for such a typically slow MR technique, it is well worth further investigation in the future, in particular using 3D techniques in conjunction with microscopy for high resolution imaging in all three dimensions over a large field-of-view.
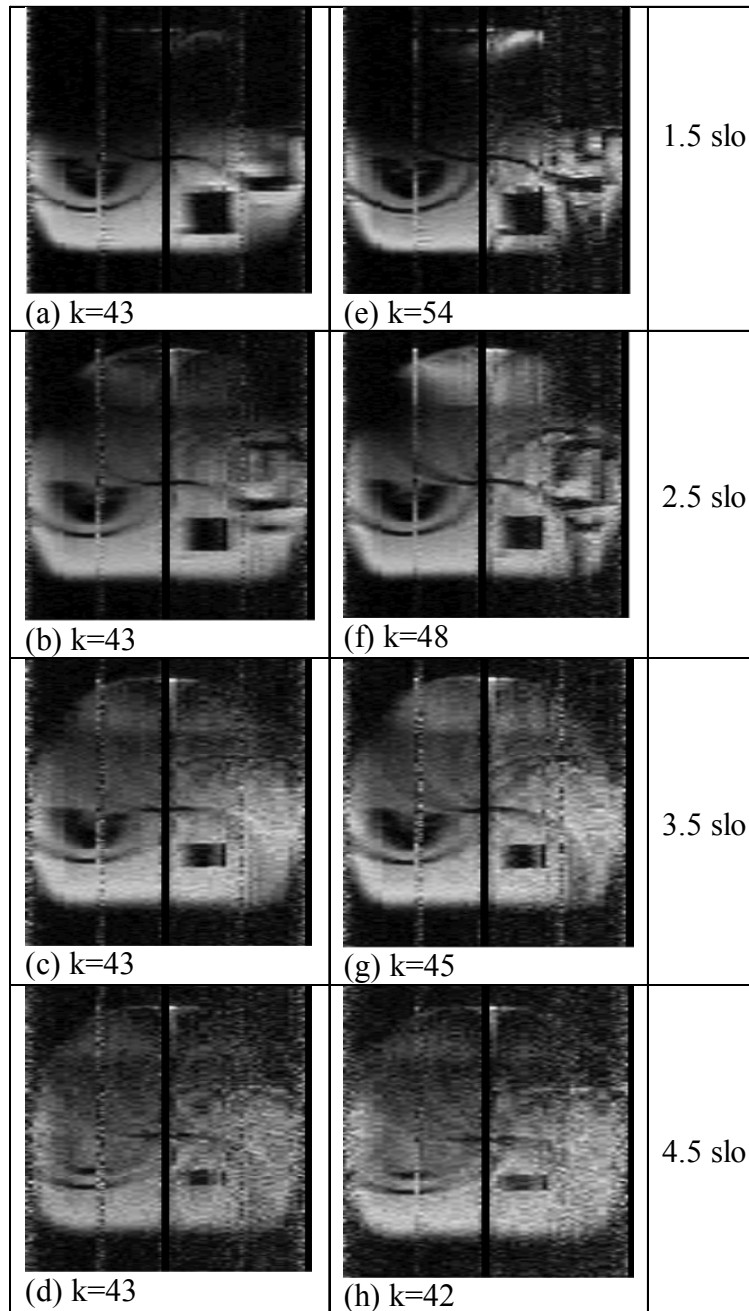
Fig. 5.15 Subset of a 3D-SEA imaging series. a-d: Four slices at offsets of 1.5mm, 2.5mm, 3.5mm, and 4.5mm, formed using the compromise compensation strength (k=43) predicted with modeling. e-f: The same four slices formed with individually chosen compensation gradient strengths.
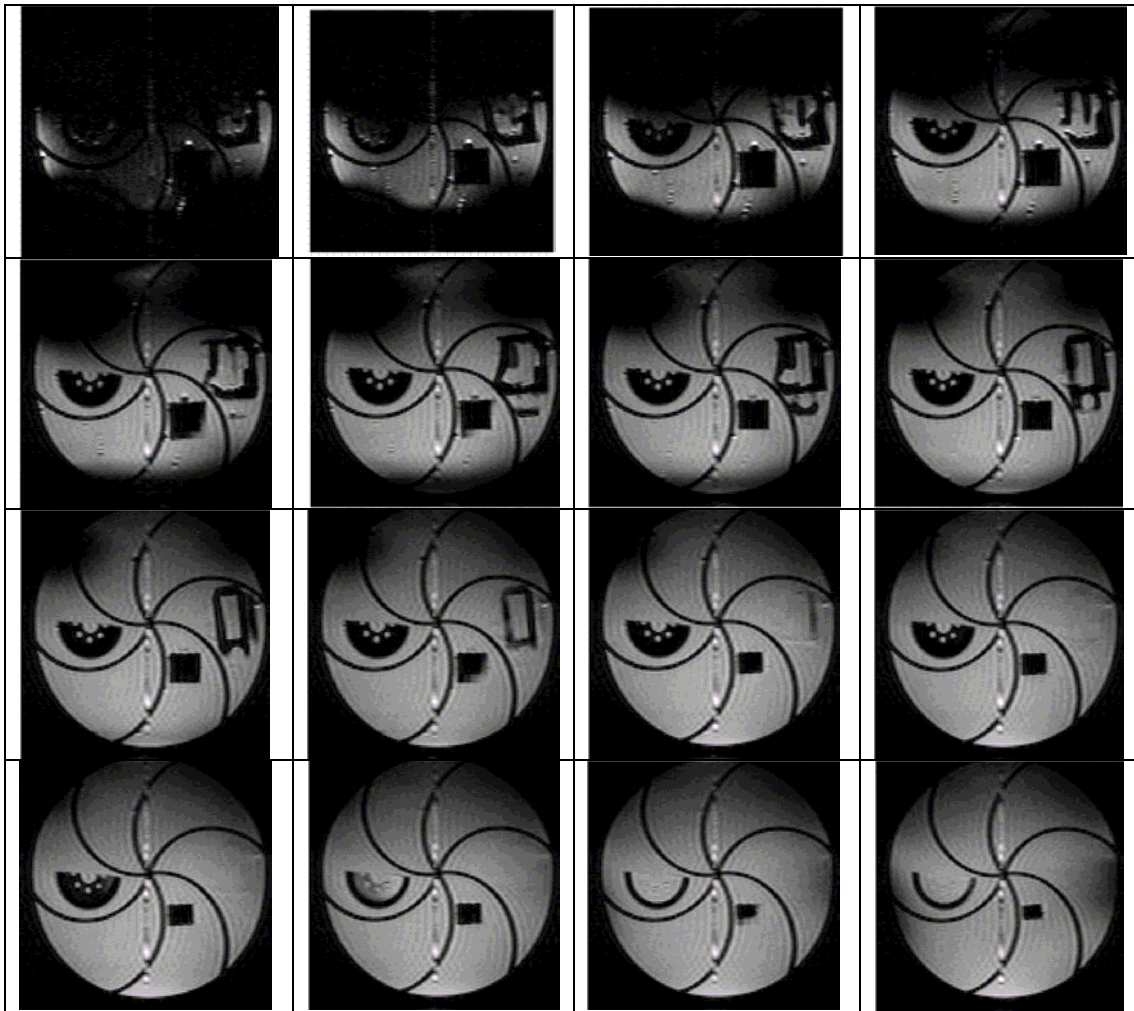
Fig. 5.16 Fully encoded 3D data set obtained from the volume coil. Sixteen ¼ mm slices are shown covering a 4mm slab. The third column corresponds to the four slices shown in Fig. 5.15.

V.3 Using SEA Array Coils for Microscopy Imaging

Microscopy is typically a very slow MR technique for several reasons: one, the voxel sizes are so small that it is necessary to acquire many averages to reach a reasonable SNR; two, if a field-of-view greater than a few centimeters is desired, then the number of samples necessary to acquire to avoid aliasing is very large. In order to increase the SNR in microscopy, small coils are used very close to the sample (91). An array of very small coils with spatially well-separated field patterns, then, lends itself nicely to implementing large-field-of-view microscopy.

In the time it takes to acquire a microscopy image with a single coil, 64 times the FOV of a single coil in the phase encoding direction would actually be acquired. Additionally, the 64 channel digital receiver offers FOV benefits in the frequency encoding direction. The digital receiver has a 1.25MHz bandwidth (where the Omega, for example, has 200kHz), allowing for effortless fast sampling of short echoes from a large field-of-view.

A single element of the 4.7T SEA array coil was used to obtain preliminary results through the Omega system (to eliminate data-handling and reconstruction complications associated with using the 64-channel receiver). A full 13cm field-of-view, 256x256 image and a zoomed 2.5cm x 2.5cm field-of-view over the "gear" structure are shown in Fig. 5.17, simply verifying that resolving small structures requires more than standard image resolution. The 2.5cm x 2.5cm field-of-view was then fully encoded with 256x256 points, yielding 100μm resolution in both dimensions, shown in Fig. 5.18. Sixty-four averages were taken, requiring a four hour imaging time. The gear was clearly resolved, and only a small amount of aliasing in the frequency encoding direction is visible (from imperfect filtering). The field of view in the frequency encoding direction was then increased to 10cm, a 15 msec echo time used, and the number of points increased to 256x1024 in order to capture the entire coil sensitivity region with 100μmx100μm resolution. While this is a close simulation of what will eventually be produced
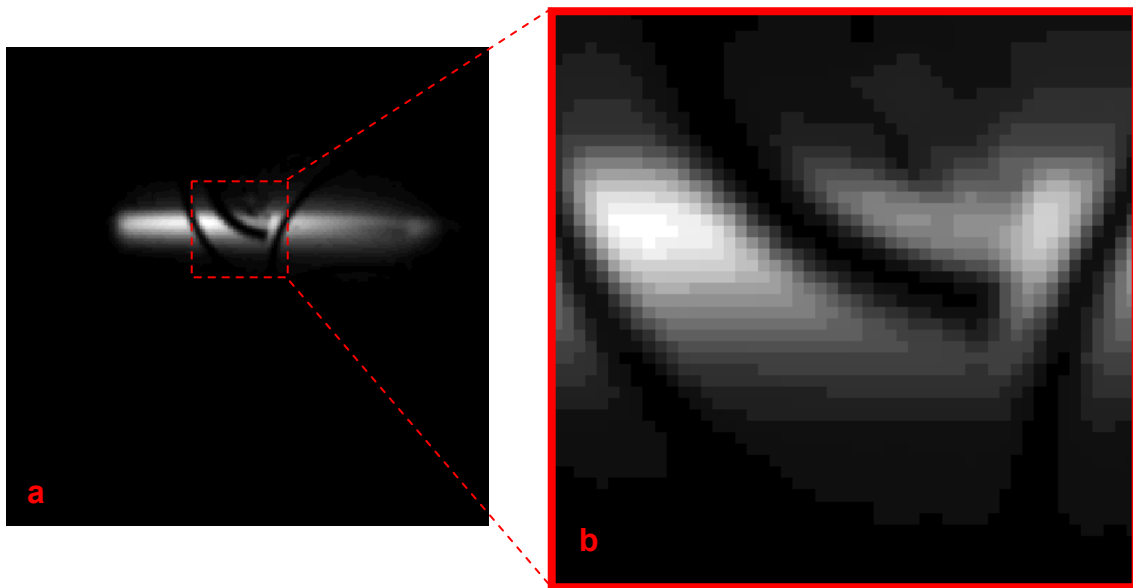
Fig. 5.17 a) Fully encoded 256x256 image of the entire sensitive region (13cm x 13cm) of an element of the 4.7T SEA array coil and b) a 2.5cm x 2.5cm zoomed region over a gear structure intended for microscopy imaging. To resolve the teeth on the gear, more than standard resolution imaging is required.
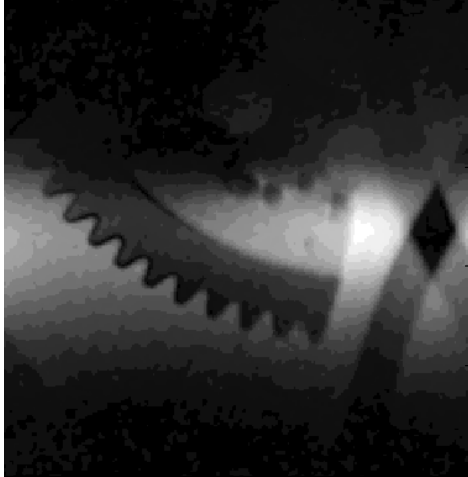
Fig. 5.18   256x256 image of 2.5cm x 2.5cm field of view, yielding 100μm resolution in both dimensions, clearly resolving the gear teeth not visible in Fig. 5.16b. A small amount of aliasing in the frequency encoding direction is visible due to imperfect filtering.

using the 64-channel receiver, the imaging parameters represented the limit of the capabilities of the Omega digitizer. A shorter echo time (often necessary in microscopy applications (92)) or larger field of view would not be possible. The full coil microscopy image is shown in Fig. 5.19. The image was made with 64 averages and took four hours to acquire. In that time, using the 64-channel receiver, all 64 such images will be simultaneously acquired, producing 100μm resolution over a 13cm x 8cm field-of-view – a area for immediate pursuance.

V.4 Non-Planar SEA Imaging

Because SEA (implemented with this coil design) is a method for surface imaging by nature, one of the more interesting questions to address when considering applications is whether or not the
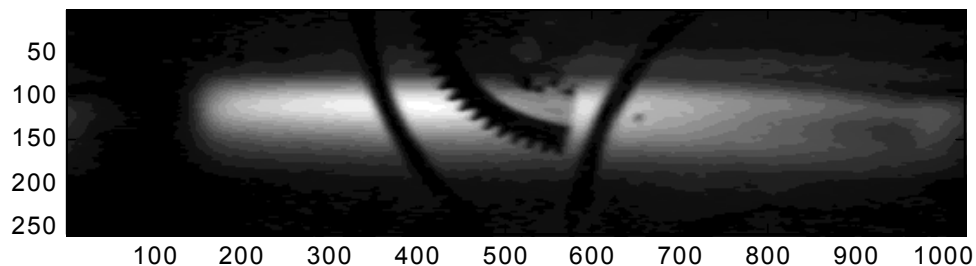
Fig. 5.19   256x1024 image over a 2.5cm x 10cm field of view. Using a 15msec echo time and producing an image very similar to that which would be produced easily by the digital receiver, the Omega reached the limits of its digitizers. The results are promising, however, for combining 64 such images into a 13cm x 8cm field-of-view image with microscopic resolution.

method can be readily applied to non-planar surfaces. Specifically, conforming a SEA array to a cylinder would permit the possibility of volume (inside the cylinder) or catheter (outside the cylinder) imaging, and conforming the array to any surface (for example, see Fig. 5.20 (93)) is a naturally ensuing extension of SEA that would vastly increase the potential for application of the method.

When the array is no longer planar, the first complication involves compensating for the effect of the phase of the elements, no longer constant across the array with respect to Cartesian coordinates, with a single pulse applied by gradient fields oriented along Cartesian axes. The most extreme case of cylindrical conformation was considered to study the possibilities. In the cylindrical array, the direction of the phase variation impressed by the coil rotates, unlike in the planar case. To more clearly illustrate the phenomenon, a "phase vector" notation is introduced in Fig. 5.21. The same phase magnitude and direction exist across every coil in the planar case, but the direction of every vector is different in the cylindrical case. Therefore, there is not a single optimal value for the compensating gradient strength (k-space line) as when the coils are planar. Instead, it would theoretically take a number of compensation pulses equal to the number of coils to perfectly correct for the coil phases, preventing true Single Echo Acquisition imaging. The quasi-static Matlab modeling program was modified to include the angle of the coil, and the same computations made in the planar case were performed: the signal strength versus compensation gradient strength was calculated, the strength translated to its k-space line equivalent, and the optimal strength observed for each of the eight coil positions labeled in Fig. 5.21 (79). A 32-channel array was modeled, as that was what would be used for testing purposes. It is worth remembering before discussion of the modeling results that by definition of SEA, a single compensation gradient can be applied before receiving a single echo, and the compensation gradient applied is in the phase encoding direction (x, in this case). The results are examined, then, with respect to the possibility of using a "compromise" gradient, as was
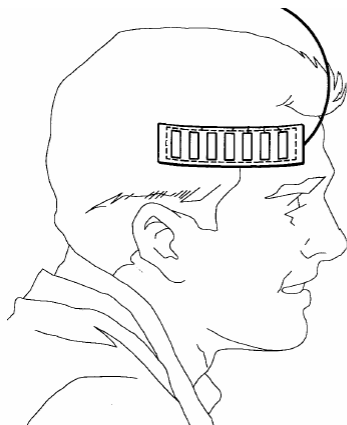
Fig. 5.20 Patent art depicting the possibility of conforming a SEA array to a surface to enable using the method on a non-planar sample.
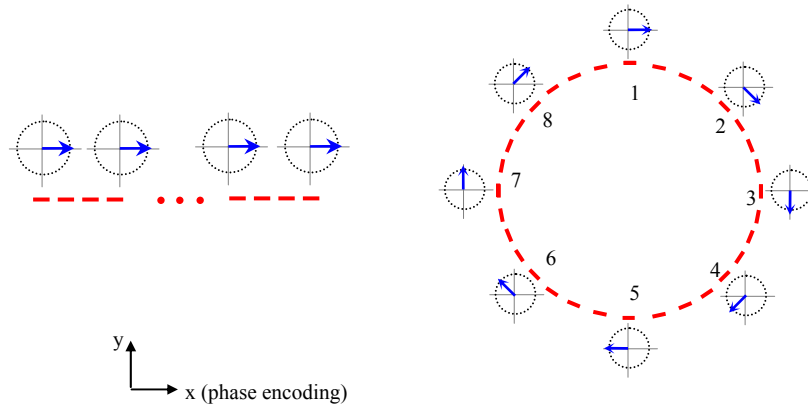
Fig. 5.21. Phase vectors (in blue) across two array configurations (coils in red): a planar array coil (left) and a cylindrical array coil (right). A single gradient pulse compensates for the phase across planar coils where it would take a number equal to the number of coils or a circular gradient to compensate in the cylindrical case. The eight sample coils used for modeling and imaging are numbered for future reference.   Reprinted with permission from (79) © 2004 IEEE

discussed when varying the slice offset. Figure 5.22 shows the results of modeling the signal strength for each of 256 phase gradient compensation values for each of the eight coils (79). There was symmetry about the k=0 line corresponding to the top-bottom sign difference (in the x direction) in the coil phases around the cylinder. Based on that characteristic alone, then, it is
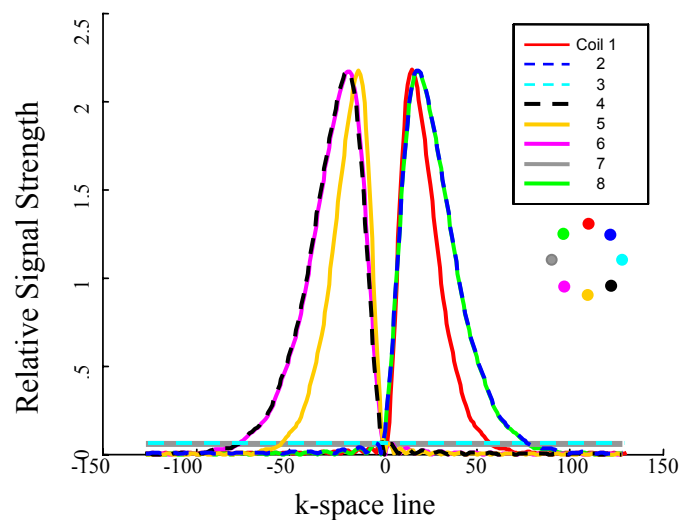
Fig. 5.22 The modeled relative signal strength versus k-space line for 8 coils in a cylindrical array. The symmetries and signal levels are explained fully in the text.   Reprinted with permission from (79) © 2004 IEEE

not possible to apply a single compromise gradient. Progression around a quadrant (i.e. from coil 1 to 3) caused the necessary x-directed compensation gradient [rad/cm] to get stronger (the peak signal to occur further out in k-space) because the coil phase change occurred over a smaller distance in x [cm]. The possibility of finding a compromise strength per quadrant is considered and discussed further below. For coils 3 and 7, which were vertical, the coil phase gradient was entirely in the y direction and could not be compensated with an x-directed phase compensation gradient. For this reason, the signal from coils 3 and 7 was nearly zero for all values of the phase compensation gradient, and would need a y-directed gradient to realize significant signal from them. Figure 5.23 further illustrates the progression of the coil phases with respect to an x-directed compensation gradient as the signal strength from each coil in the first quadrant is plotted versus k-space line. It can be seen from this figure that if a compromise strength per quadrant were chosen (disregarding the vertical coil) at the intersection of coil 1 and coil 8, that approximately half the signal would be lost from those coils and significant losses would also be suffered by coils 2 and 3. While using a single compensation strength was not a viable possibility, a coil was built to test the modeling and the possibility of finding the minimal number of echoes to create a cylindrical image.
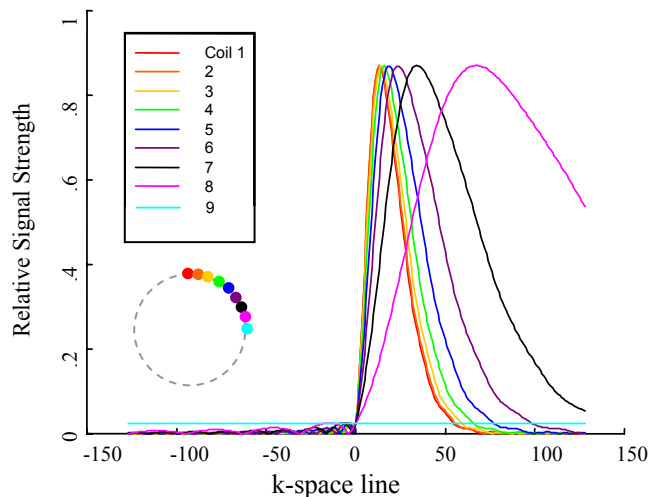
Fig. 5.23. Relative signal strength versus compensation gradient (k-space line) for the nine coils in the first quadrant of the cylindrical test array.

Fig. 5.24 32-channel SEA array fabricated on 10-mil thick RO3010, conformed around a 2.2-cm diameter test tube.

A 32-channel array of planar pair elements was fabricated on 10-mil thick RO3010 (Rogers) flexible substrate and then conformed around a 2.2-cm diameter test tube, and submerged in gelled relaxed solution (see Fig. 5.24). Three coils, 45° apart, were matched and tuned for testing. When trying to acquire images with the coils, an additional but unanticipated problem with using the cylindrical array in a similar manner to the planar array arose. The planar array is easily geometrically decoupled from a linear transmit coil, but the elements of the cylindrical array that were not aligned with the transmit field coupled noticeably. The transmit volume coil was changed from the parallel plate coil to an eight leg birdcage that was actively decoupled in receive-mode and passive diode decoupling across the tuning network of the three planar pair elements was added to detune them during transmit mode. Passive networks always leave some residual current, and very close to the element, where SEA imaging is performed, even that small current proved to be problematic. Decoupling in the array coil proved to be inadequate, then, with passive diode networks, and active networks may be too complex and space consuming for large arrays of voxel-sized coils; however this solution will be investigated as future work.

In the case of cylindrical coils for SEA (or even highly accelerated) imaging, the most viable option appeared to be a transmit/receive architecture, where the need for a phase compensation gradient is eliminated entirely since the phase imparted during the transmit pulse is compensated by the conjugate phase imparted during receive. The modeled and measured data for two coils in the array, 90° apart, acting in transmit/receive mode, are shown in Figure 5.25 (79). While the width of the peak in k-space varies due to the coil angle, the peak signal is always received at the k=0 line for a transmit/receive coil. Implementing a transmit/receive architecture seems to be the most promising method of implementation for using SEA on non-planar surfaces, but will require a complex interface to the scanner, worthy of significant investigation in future work.
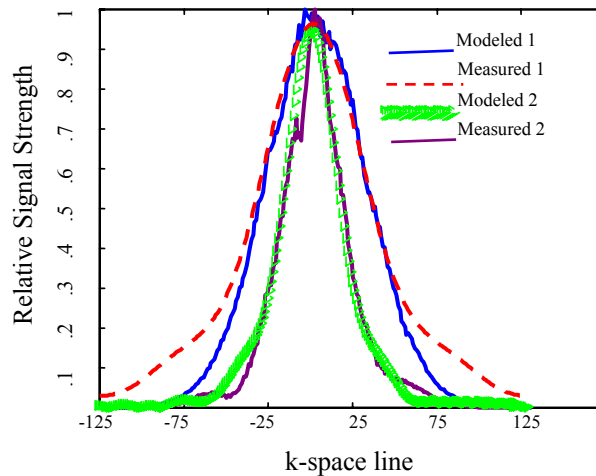
Fig. 5.25. Modeled and measured data for two coils, 90 degrees apart, operated in transmit/receive mode. The peak signal is then always received at the zero line of k-space.
Reprinted with permission from (79) © 2004 IEEE

V.5 SEA Imaging at Extremely High Frame Rates

The final application of SEA imaging to be discussed is the primary capability of the method to form MR images at a rate limited only by the time it takes to acquire an echo. Using echo trains, where the signal is refocused and an echo produced as often as every millisecond, imaging at 1000 frames/sec could be possible using the method. The relevance to science of being able to combine the capabilities of MR imaging with the ability to capture activity that occurs at 1000 frames/sec is most likely something that cannot be fully appreciated at this time. The tool, however, has been developed already at 125 frames/sec and moving to 1000 frames/sec will be the focus of work in the following months.

Implementing SEA to make movies was as much a matter of data manipulation as pulse sequence optimization. A gradient echo sequence was used with TR/TE = 8msec/4msec. An echo was acquired, then, every eight milliseconds for 128 acquisitions, giving an effective frame rate of 125 frames/sec and producing 100MB of data in one second – the limit of the capability of the digitizer boards currently in use. When the signals leave the receiver, they are at a 500kHz intermediate frequency, and are input to the two 32-channel ICS-645 digitizers (Interactive Circuits and Systems Ltd., Gloucester, Ontario), which have 1MB of onboard

memory. From the digitizers, the signals are offloaded to RAM (limiting the amount of data possible to collect) during the TR (limiting the speed at which it is possible to collect it) for later processing. These limitations are in the process of being eliminated, but are meanwhile providing restricting guidelines in this application area.

As a seemingly predictable first experiment, uncomplicated by external motion, an attempt was made to observe and measure the progression of distilled water and relaxed solution to steady state using two different tip angles. It was expected that both would have equal intensities in the first frame (fully relaxed magnetization being excited) and that the water would decay far more quickly (much longer T1) than the copper sulfate solution, with the signal loss occurring more quickly for a higher tip angle than for a low tip angle. A spiraled phantom similar to the one previously used was filled alternatingly with distilled water and 1g/L $CuSO_4$. The gradient echo sequence with a three degree tip angle and imaging parameters described above were used to acquire 128 SEA images in 1.024 seconds. Every fourth frame in the series is shown in Fig. 5.26. The compartments that remained bright were those filled with relaxed solution and the ones that grew dark were filled with distilled water. The same experiment was then repeated for a 45 degree tip angle. The signal levels frame-per-frame appear to behave as expected, with the water decaying and the relaxed solution remaining brighter, but when a region in two of the compartments was selected to average and plot the signal levels (see Fig. 5.27), the behavior was not consistent with the phenomenological contrast equations for MR. The decay of the water was not as fast as expected; there was no decay in the relaxed solution; the expected difference in the two tip angles was not present. The contrast equations assume the decay of all transverse magnetization between RF excitations and iteratively calculate the evolution of transverse magnetization (source of signal) given TR and T1 values. If TR $\ll$ T1 (or T2), then residual transverse magnetization would cause unexpected behavior such as that seen. In an effort to understand the results, straightforward experiments were performed to measure the respective T1 values at 4.7T of distilled water and 1g/L $CuSO_4$.

A series of gradient echo images were taken of two test tubes: one filled with 1g/L copper sulfate and one filled with distilled water. The TR was varied from 100msec to 10000msec, the relative signal level plotted as a function of TR, and the curve fit to the standard contrast equation where signal equals $C(1-e^{-T1/TR})$. The results are shown in Fig. 5.28 and 5.29, with the images set to a colormap to accentuate the signal growth, and the theoretical and measured signal curves versus TR shown. The T1 at 4.7T of water was found to be 4250msec, and the T1 at 4.7T of 1g/L CuSO4 was found to be 780msec. Both of the values were much longer than expected, probably contributing to at least a portion of the unanticipated results seen in the SEA movies.
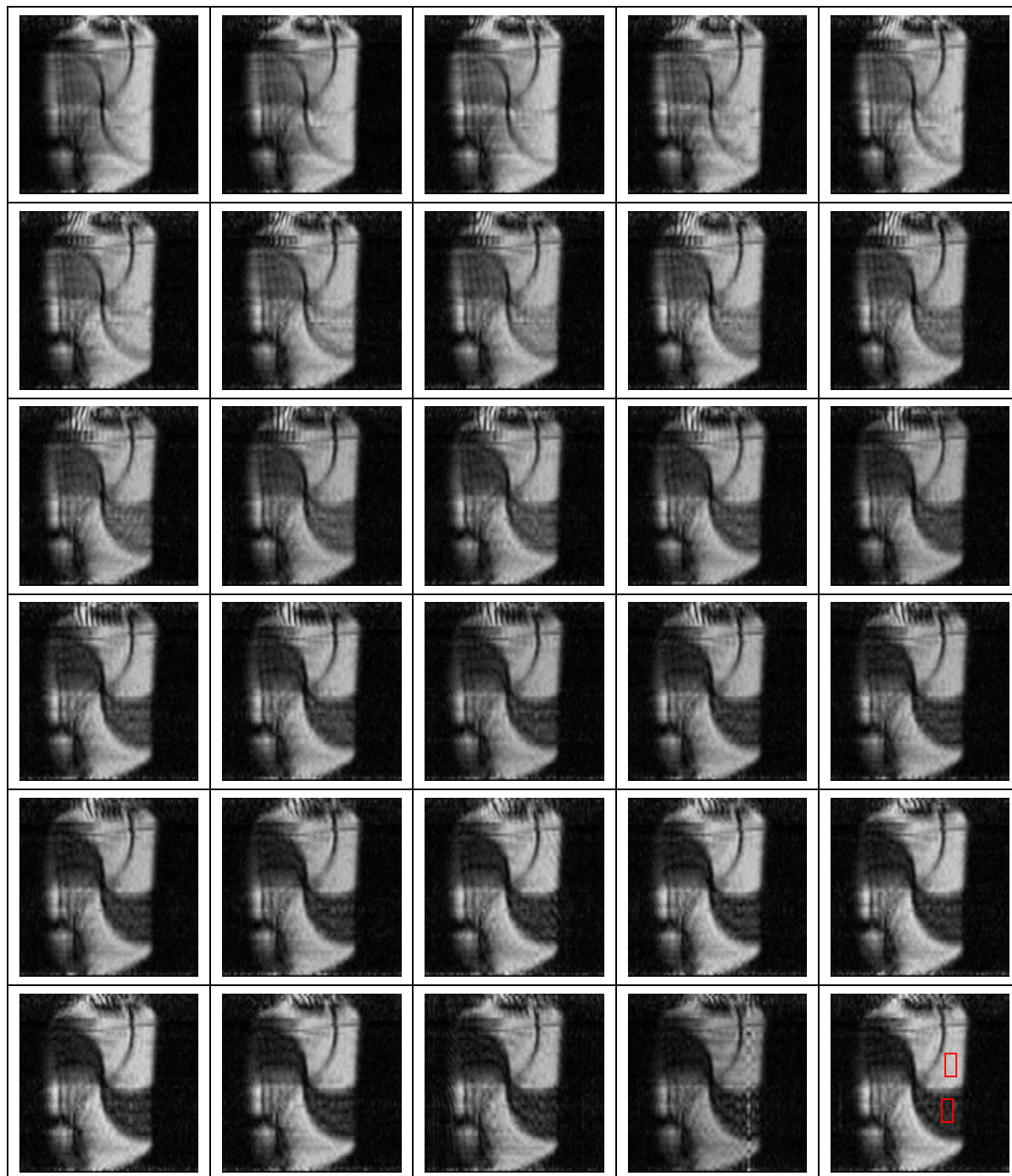
Fig. 5.26 Every fourth frame out of a series of 125 acquired in one second. The bright compartments are filled with relaxed solution and the dark ones are filled with distilled water. The regions for signal averaging in Fig. 5.26 are marked in the last frame. While the signals appear to decay and reach steady state as expected, actually tracking the signal strength over the 1 second time period revealed unexpected behavior, as is shown in Fig. 5.27.
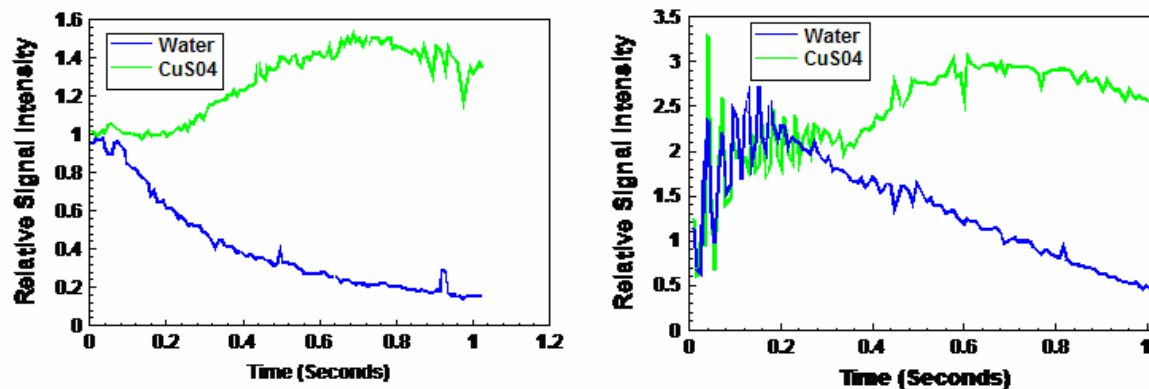
Fig. 5.27 Signal intensity vs. time for two compartments – one filled with water and one filled with relaxed solution – from image series with tip angles of 3 degrees (left) and 45 degrees (right). The averaging regions in the two compartments are shown in Fig. 5.25. The signal levels do not behave as expected according to MR contrast equations regarding magnetization. The oscillations in the signal in the plot on the right corresponded to bands circulating in the compartments.

a

b
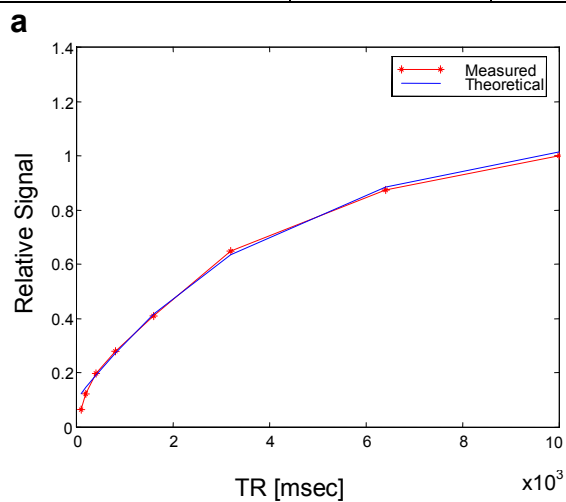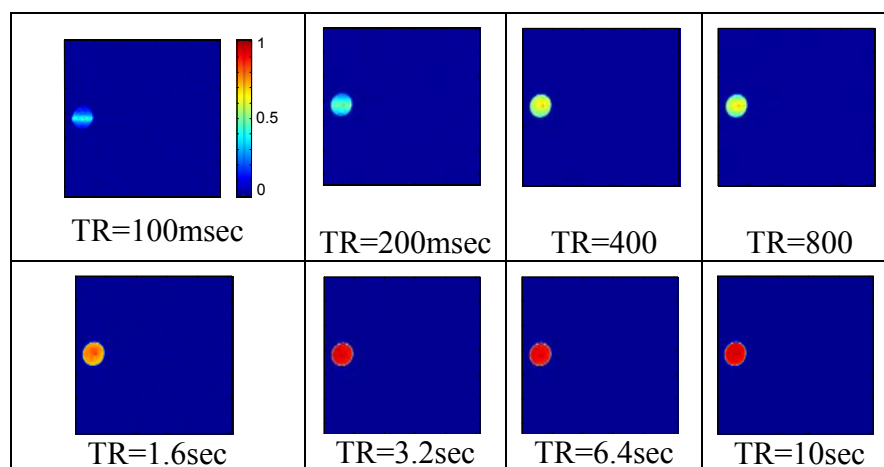
Fig. 5.28 Experimental data to determine T1 of distilled water. (a) Set of images formed of a test tube filled with distilled water. The TE was set to 20msec and the TR was varied as labeled. (b) The measured and theoretical signal curves vs. TR, indicating that T1=4250msec for distilled water at 4.7T.

a

b
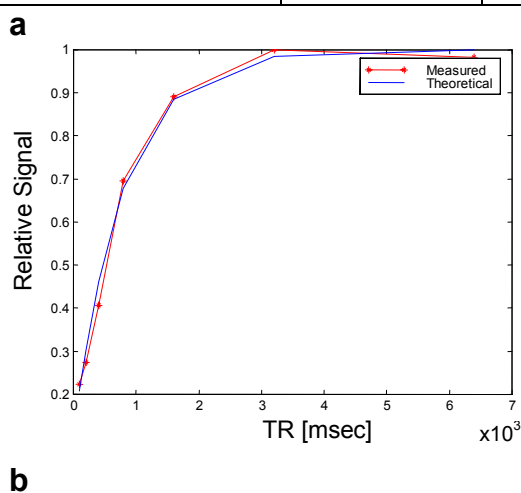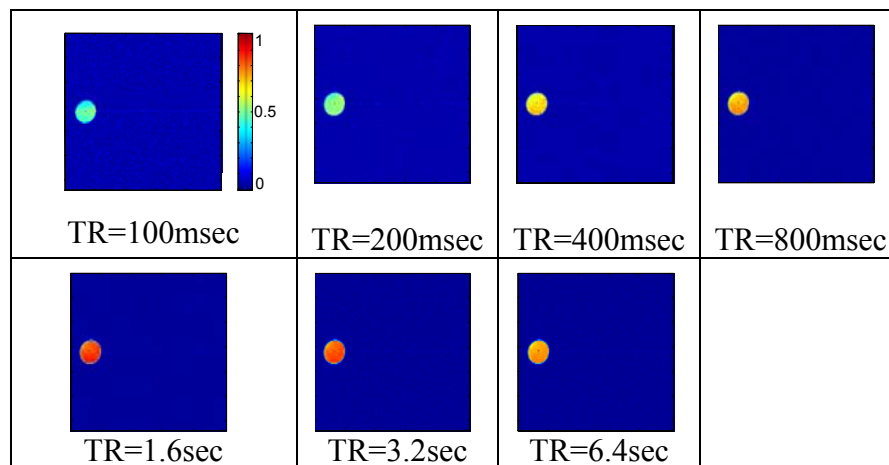
Fig. 5.29 Experimental data to determine T1 of relaxed solution. (a) Set of images formed of a test tube filled with 1g/L CuSO$_4$. The TE was set to 20msec and the TR was varied as labeled. (b) The measured and theoretical signal curves vs. TR, indicating that T1=780msec for this relaxed solution at 4.7T.

What was expected to be a relatively simple (and very fast) method to measure T1 in a sample actually indicated complex interactions that could be used to study magnetization development in pulse sequences or, with more accurate fitting equations, to obtain very rapid T1 and T2 maps.

To more clearly indicate the speed of SEA and its ability to image motion, a rotating phantom was constructed with a propeller submerged in relaxed solution run by a motor outside the bore of the magnet. It is pictured in Fig. 5.30, along with a fully encoded spin echo image of the slice used for fast frame images (94). Movies were made with the propeller rotating at approximately 60rpm and 360rpm using the same procedure as was used to study contrast. A gradient echo sequence with TE/TR=4/8msec was used to acquire 128 SEA images in 1.024sec, the fastest MR images made to date by nearly an order of magnitude. A primary advantage of using SEA to image motion is the lack of typical motion artifacts (which always occur in the phase encoding direction) because there is no phase encoding used. Every fourth frame from the two movies is shown in Figs. 5.31 and 5.32. With imaging at 125 frames/sec, there is no aliasing, and every frame shows a progression of significantly less than 90 degrees per blade. At
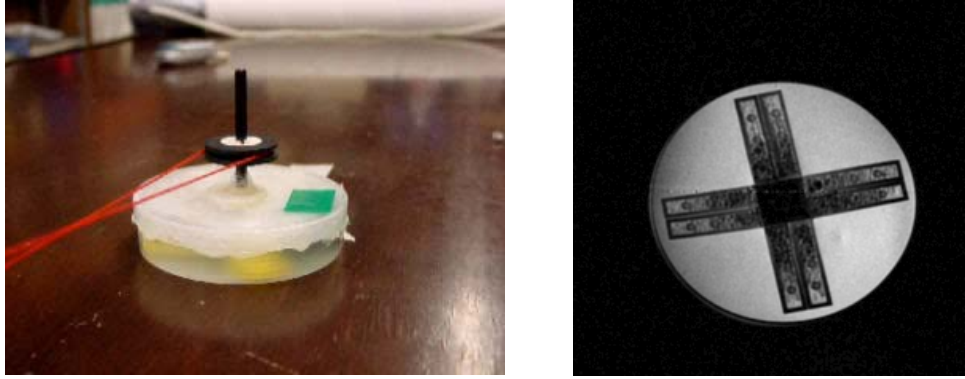
Fig. 5.30 Rotating phantom used for fast frame rate imaging – propeller submerged in relaxed solution, run with a motor outside the bore – and a 256x256 spin echo image of the slice at 0rpm.

60rpm (Fig. 5.31), the images appeared as anticipated, with reasonable SNR and the resolution expected of SEA (64x128). At 360 rpm (Fig. 5.32), the loss of signal seen in the center of the phantom was assumed to be due to total dephasing of the signal due to extremely high velocities. When the phantom was removed from the bore, however, it was realized that the insensitivity of SEA to motion artifacts had been underestimated. The lack of signal was, in fact, due to the solution being forced to the edges of the phantom by the speed of the propeller.

V.6 Concluding Remarks

This chapter has demonstrated methodologies for applying SEA and its variations. The study was not intended to be exhaustive for any given application, but instead to illustrate potential areas of interest as 64-channel (and higher) systems become more widely available. The final chapter will reiterate the current and potential value of this work, in the spirit of providing a basis for future research.
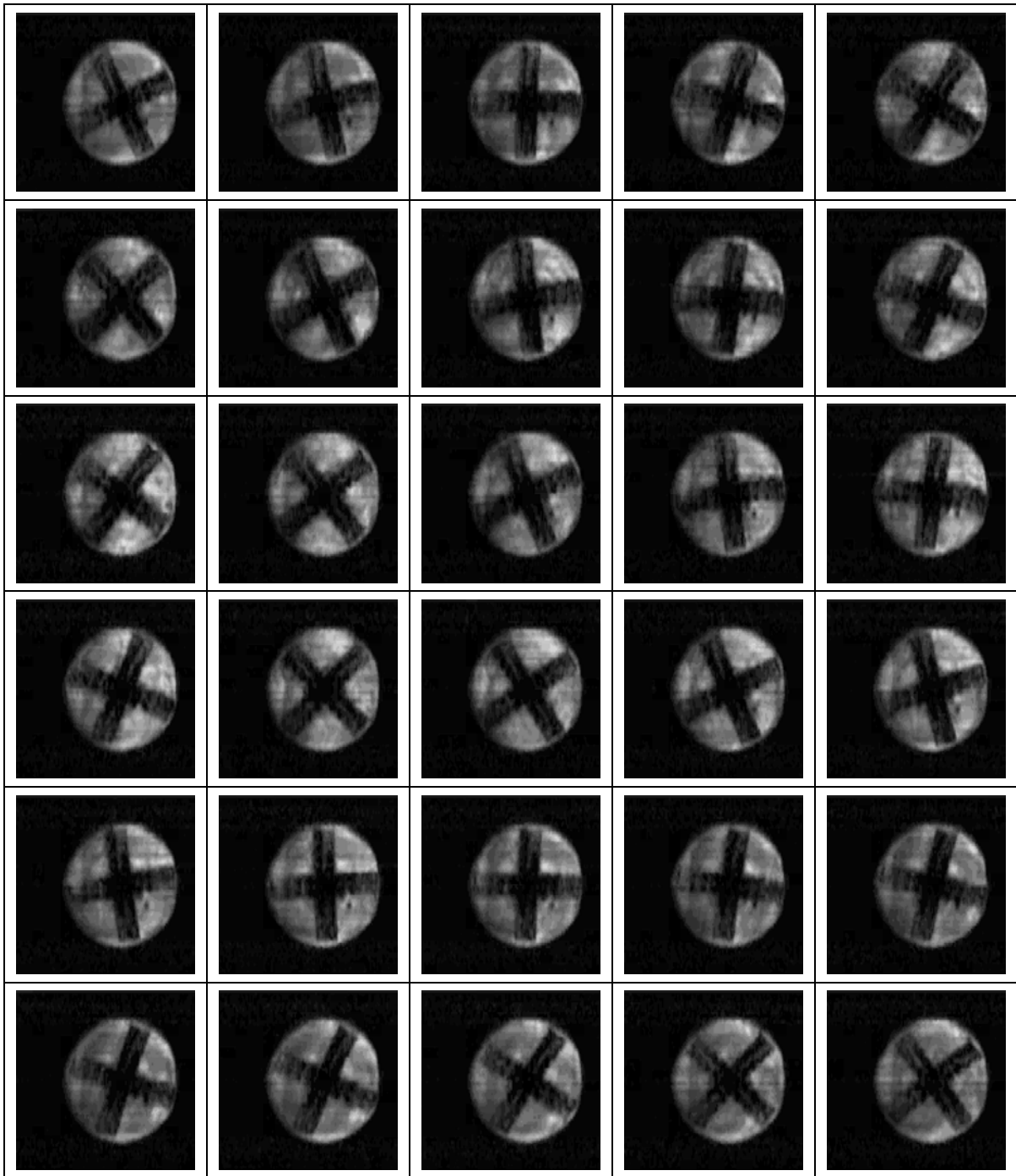
Fig. 5.31 Fast frame rate imaging of a propeller rotating at 60rpm (every fourth frame out of a series of 125 acquired in one second). The motion is imaged quickly enough using SEA to prevent all aliasing, with each frame depicting significantly less than 90 degrees rotation from the previous frame. Because SEA does not phase encode, motion artifacts are eliminated.
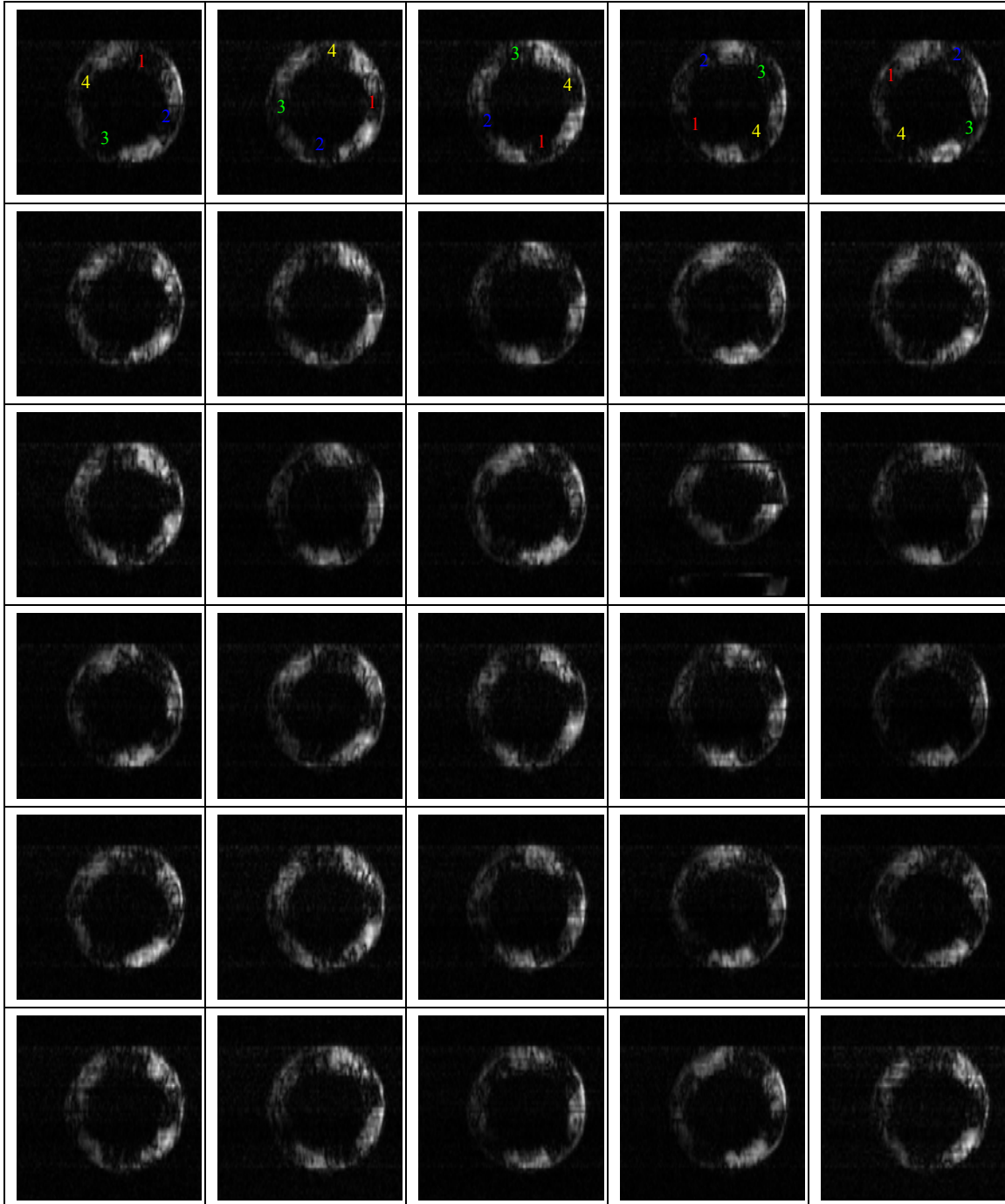
Fig. 5.32 Fast frame rate imaging of a propeller rotating at 360rpm (every fourth frame out of a series of 125 acquired in one second). The four propeller blades are labeled in the first four frames to clarify the motion. The rotation was fast enough that in four frames (32 msec), slightly less than 90 degrees of motion was covered by a blade. The lack of signal in the center of the phantom is due to what has been termed the "washing machine effect", where the solution was forced to the edges of the dish by the speed of the propeller.

CHAPTER VI

FUTURE WORK AND CONCLUSIONS

This work has described the first efforts in the field of MRI to form an image without using multiple echoes, an idea first proposed over fifteen years ago. To enable this new method, Single Echo Acquisition (SEA) MRI, new coil implementations were designed, constructed, and characterized, and new methodologies were developed specific to the coils and imaging goals. The method was then implemented and tested in several initial application areas, defining a large body of potential future work in the process.

The array coil designed and constructed to facilitate SEA was the first 64-channel coil ever made for MRI. The elements were long and narrow, closely spaced, parallel planar pairs, designed to provide spatial localization in the phase encoding direction. The prototype array was built for operation at 4.7T and was completely planar, with all matching and tuning elements removed from the coil by a half-wavelength and the need for decoupling elements removed by the choice in element design. This unusual characteristic was critical in later investigations regarding the ability to conform the array to a surface for imaging. The operative version of the 64-channel array coil was also unique in its use of ultrasound cabling (because of the large number of channels) with a reasonably low degradation in Q factor. A scaled version of the 4.7T 64-channel array coil was also designed and constructed for imaging at 1.5T, with the need for a specific decoupling mechanism arising with the scaling. A novel and effective implementation of single-capacitor decoupling realized as distributed capacitance on thin substrates allowed the "planar" characteristic of the array to remain intact.

With the array designed according to a set of parameters defined by the need to replace phase encoding steps, the first MR images acquired in a single echo were made. In its simplest form, the echo simultaneously received from each coil was 1-D Fourier transformed and stacked to form a SEA image with $64xN_{readout}$ resolution. In order to define a voxel width with their sensitivity patterns, the coils in the array were necessarily very small, seeing only a limited portion of the field-of-view. This circumstance led to the investigation and implementation of a gradient pulse in the SEA sequence to compensate for the phase across the coils, giving the means to recover the signal level in the images and/or offering unexpected control over the level of resolution in the images. This need for a compensation pulse across a coil was a previously unexplored topic in MRI, fundamental to SEA imaging in this implementation, irrespective of element design or other parameters. Using the SEA array, images were also obtained at

unprecedented acceleration factors using partially parallel imaging techniques, and the opportunity was used to clearly define current acceleration terminology, a point of discussion in the field of parallel imaging. The implementation of SEA in the form described is a method characterized by a shallow penetration depth and a resolution defined by the sensitivity pattern of a coil – and a method capable of imaging at unexplored rates, restricted only by the time it takes to acquire an echo. These limitations and powerful capabilities were the defining considerations when developing methodologies to apply SEA.

The ability of the method to operate in its most basic application, fast single slice imaging, was examined with respect to imaging depth and resolution. Modeling and verification was performed of the necessary adjustment of the phase compensation gradient with depth, and an artifact that appeared when imaging at increasing distances from the coil was examined closely. The artifact was eventually found to be a full wave effect originating from very slightly non-uniform currents on the legs. The effect of the artifact on SEA is seen in partial shading of the images with increasing depths, further contributing to the limited penetration depth. SEA imaging with 64 coils was compared to conventional 64, 128, and 256 phase encoded images, and the resolution found to be comparable to phase encoding with 64 lines, as would be expected. Since 128 and 256 phase encoding lines are standard in clinical practice, a straightforward resolution enhancement technique that did not sacrifice the speed of the method was examined. In addition to studying the in-plane resolution, the ability to obtain high through-plane resolution using 3D MR imaging techniques was examined. The first 3D-SEA images were successfully obtained, enabling 0.25mm slices and verifying that it is possible to choose a single compromise gradient compensation strength over a large excited slab. In another application that would benefit from reduced matrix sizes (and therefore reduced imaging time), the viability of implementing large field-of-view microscopy using the SEA coil was preliminarily studied. A naturally ensuing extension of SEA imaging is to make the arrays conformal, facilitating curved surface and volume or catheter imaging. Since gradients are applied along Cartesian axes, methods to overcome the need for a compensation gradient conformed to the surface of the array were modeled and examined. Finally, as a demonstration of the ultimate enablement of SEA, MR movies were taken at rates of 125 frames/second, the fastest MR images ever taken by almost an order of magnitude, and a number that could increase to as much as 1000 frames/second using recalled echoes. The value to science of combining the strengths of MRI with imaging at 1000 frames/second is most likely unanticipated at this time, but represents a potentially powerful tool.

Throughout this work, it has been recognized that a portion of the contribution was in the significant amount of future work that was being defined. Improvements can be made in the data acquisition system, the array coils, and the imaging methods, and the application areas are ripe for investigation.

The data acquisition system is already in the process of a significant upgrade, adding real-time DSP to remove the limits in data rates, storage, number of frames possible to acquire, length of TR, etc. In addition, better preamplifiers (higher gain, less sensitive to heat, more reliable connectors) have already been obtained from Siemens Medical Systems, but will need to be retuned, mounted, and connected to the current coil set-up. In a more long term goal, the data acquisition system would be upgraded to contain a 128-channel receiver.

The main area of immediate improvement in the array coil needs to be in correcting the current distribution to remove the presence of the artifactual null at deeper depths. This would best be studied in conjunction with an effort to implement loops instead of planar pairs in an overall effort to increase the penetration depth of the method, but also stands alone as a much needed improvement on the planar pair array. Taking the coils to a working cylindrical configuration is also an area for immediate investigation. This will require implementing a 64 channel transmit/receive architecture, and also, in order to maintain the Q of the coils, it would be desirable to realize the match and tune network on the coil using a method that maintains flexibility. Lower loss coil designs could be studied, including methods as straightforward as using thicker copper and as complex as using HTS (high temperature superconducting) materials. In addition to improving or altering the current design, NIH funding is already in place to also study different configurations for 64-channel coils, including 2D arrays.

The imaging system needs to be improved, though not necessarily urgently. Obtaining a larger, clinical-sized scanner would allow for the use of larger coils (more applications, more easily handled) on a regular basis in town. A more homogenous shim across the array would also be present then, making the compensation gradient used affect all coils equally. The shim in the 4.7T in the MRSL could be improved by purchasing a new combined shim/gradient set from a vendor such as Magnex Scientific or Resonance Research Inc. – a large but possibly worthwhile purchase, depending on the applications to be implemented using the system.

The potential application areas for SEA, variations on SEA, and the SEA array coils (some of which were mentioned above and in the text of Chapter V) are numerous, exciting, and pleading for attention. Not previously mentioned is the fact the upgrade to the new DSP system will facilitate the ability to conduct DCE (dynamic contrast enhanced) imaging animal studies at M.D. Anderson Cancer Center, where a protocol has already been approved.

The greatest contribution of a work is in its existence as a building block. By definition of its newness, this work has defined projects for many future students. The areas in which the greatest contributions will be made, however, are hopefully unanticipated and even unimaginable at this time.

REFERENCES

1.   Haacke EM, Brown RW, Thompson MR, Venkatesan R. Magnetic resonance imaging : physical principles and sequence design. New York: J. Wiley & Sons; 1999. 914 p.

2.   Knopp MV, Giesel FL, Marcos H, von Tengg-Kobligk H, Choyke P. Dynamic contrast-enhanced magnetic resonance imaging in oncology. Top Magn Reson Imaging 2001;12(4):301-308.

3.   Miller SL, Hoffer FA, Reddick WE, Wu S, Glass JO, Gronemeyer SA, Haliloglu M, Nikanorov AY, Xiong X, Pappo AS. Tumor volume or dynamic contrast-enhanced MRI for prediction of clinical outcome of Ewing sarcoma family of tumors. Pediatr Radiol 2001;31(7):518-523.

4.   Taylor JS, Tofts PS, Port R, Evelhoch JL, Knopp M, Reddick WE, Runge VM, Mayr N. MR imaging of tumor microcirculation: promise for the new millennium. J Magn Reson Imaging 1999;10(6):903-907.

5.   Evelhoch JL. Key factors in the acquisition of contrast kinetic data for oncology. J Magn Reson Imaging 1999;10(3):254-259.

6.   Knopp MV, von Tengg-Kobligk H, Choyke PL. Functional magnetic resonance imaging in oncology for diagnosis and therapy monitoring. Mol Cancer Ther 2003;2(4):419-426.

7.   Nitz WR. Fast and ultrafast non-echo-planar MR imaging techniques. Eur Radiol 2002;12(12):2866-2882.

8.   Pettigrew RI, Oshinski JN, Chatzimavroudis G, Dixon WT. MRI techniques for cardiovascular imaging. J Magn Reson Imaging 1999;10(5):590-601.

9.   Sakuma H, Takeda K, Higgins CB. Fast magnetic resonance imaging of the heart. Eur J Radiol 1999;29(2):101-113.

10.   Jolesz FA. Interventional and intraoperative MRI: a general overview of the field. J Magn Reson Imaging 1998;8(1):3-7.

11.   Lardo AC. Real-time magnetic resonance imaging: diagnostic and interventional applications. Pediatric Cardiology 2000;21(1):80-98.

12.   Kollias SS, Bernays R, Marugg RA, Romanowski B, Yonekawa Y, Valavanis A. Target definition and trajectory optimization for interactive MR-guided biopsies of brain tumors in an open configuration MRI system. J Magn Reson Imaging 1998;8(1):143-159.

13.   Manke C, Nitz WR, Lenhart M, Volk M, Geissler A, Djavidani B, Strotzer M, Kasprzak P, Feuerbach S, Link J. [Stent angioplasty of pelvic artery stenosis with MRI control: initial clinical results]. Stentangioplastie von beckenarterienstenosen unter MRT-kontrolle: erste klinische ergebnisse. Rofo Fortschr Geb Rontgenstr Neuen Bildgeb Verfahr 2000;172(1):92-97.

14.   Lin W, Celik A, Paczynski RP. Regional cerebral blood volume: a comparison of the dynamic imaging and the steady state methods. J Magn Reson Imaging 1999;9(1):44-52.

15.   Cohen MS. Real-time functional magnetic resonance imaging. Methods 2001;25(2):201-220.

16.   Gunther M, Oshio K, Ruppert K, Feinber D. Comparison of ultrafast full-brain 3D-imaging techniques: 3D-GRASE, EVI, 3D-EPI and 3D-PRESTO. In: Proc 10th Annual Meeting ISMRM, Honolulu, 2002. p 10.

17.   Hardy CJ. Real-time large-FOV MRI with a massively parallel 32-channel MRI system and detector array. In: Proc 11th Annual Meeting ISMRM, Toronto, ON, Canada, 2003. p 471.

18.   Heid O. The limitations of gradient-based MRI. In: Proc ISMRM Workshop on Limits of Detection in NMR, Berkeley, CA, 2001. p 33.

19.   Hamm B, Fischer E, Taupitz M. Differentiation of hepatic hemangiomas from metastases by dynamic contrast-enhanced MR imaging. J Comput Assist Tomogr 1990;14:205-216.

20.   Takehara Y. Fast MR imaging for evaluating the pancreaticobiliary system. Eur J Radiol 1999;29:211-232.

21.   Outwater EK. Ultrafast MR imaging of the pelvis. Eur J Radiol 1999;29:233-244.

22.   Yen YF, Han KF, Daniel BL, Heiss S, Birdwell RL, Herfkens RJ, Sawyer-Glover AM, Glover GH. Dynamic breast MRI with spiral trajectories: 3D versus 2D. J Magn Reson Imaging 2000;11(4):351-359.

23.   Constable R, Anderson A, Zhong J, Gore J. Factors influencing contrast in fast spin-echo MR imaging. Magnetic Resonance in Medicine 1992;10:497-511.

24.   Constable R, Gore J. The loss of small object in variable TE imaging: implications for FSE, RARE, and EPI. Magnetic Resonance in Medicine 1992;28:9-24.

25.   Roschmann P. Radiofrequency penetration and absorption in the human body: limitations to high-field whole-body nuclear magnetic resonance imaging. Med Phys 1987;14(6):922-931.

26.   Wildermuth S, Dumoulin CL, Pfammatter T, Maier SE, Hofmann E, Debatin JF. MR-guided percutaneous angioplasty: assessment of tracking safety, catheter handling and functionality. Cardiovasc Intervent Radiol 1998;21(5):404-410.

27.   Wildermuth S, Erhart P, Leung DA, Gohde S, Schoenenberger A, Debatin JF. [Active instrumental guidance in interventional MR tomography: introduction to a new concept]. Aktive instrumentenfuhrung in der interventionellen MR-tomographie: einfuhrungen in ein neues Konzept. Rofo Fortschr Geb Rontgenstr Neuen Bildgeb Verfahr 1998;169(1):77-84.

28.   Gould SW, Lamb G, Lomax D, Gedroyc W, Darzi A. Interventional MR-guided excisional biopsy of breast lesions. J Magn Reson Imaging 1998;8(1):26-30.

29.   Zhang B, Yen YF, Chronik BA, McKinnon GC, Schaefer DJ, Rutt BK. Peripheral nerve stimulation properties of head and body gradient coils of various sizes. Magn Reson Med 2003;50(1):50-58.

30.   Brand M, Heid O. Induction of electric fields due to gradient switching: a numerical approach. Magn Reson Med 2002;48(4):731-734.

31.   Kimmlingen R, Gebhardt M, Schuster J, Brand M, Schmitt F, Haase A. Gradient system providing continuously variable field characteristics. Magn Reson Med 2002;47(4):800-808.

32. Vogt F, Ladd M, Mateiescu S, Hebrank F, Zhang B, Goehde S. Impact of increased dB/dT on peripheral nerve stimulation in clinical MRI. In: Proc 10th Annual Meeting ISMRM, Honolulu, HI, 2002. p 708.

33. Roemer PB, Edelstein WA, Hayes CE, Souza SP, Mueller OM. The NMR phased array. Magn Reson Med 1990;16(2):192-225.

34. Carlson JW. An algorithm for NMR imaging reconstruction based on multiple RF receiver coils. J Magn Reson 1987;74:376-380.

35. Hutchinson M, Raff U. Fast MRI data acquisition using multiple detectors. Magn Reson Med 1988;6(1):87-91.

36. Kwiat D, Einav S, Navon G. A decoupled coil detector array for fast image acquisition in magnetic resonance imaging. Med Phys 1991;18(2):251-265.

37. Kelton JR, Magin RL, Wright SM. An algorithm for rapid image acquisition using multiple receiver coils. In: Proc 8th Annual Meeting SMRM, Amsterdam, Netherlands, 1989. p 1172.

38. Ra JB, Rim CY. Fast imaging using subencoding data sets from multiple detectors. Magn Reson Med 1993;30(1):142-145.

39. Pruessmann KP, Weiger M, Scheidegger MB, Boesiger P. SENSE: sensitivity encoding for fast MRI. Magn Reson Med 1999;42(5):952-962.

40. Griswold MA, Jakob PM, Nittka M, Goldfarb JW, Haase A. Partially parallel imaging with localized sensitivities (PILS). Magn Reson Med 2000;44(4):602-609.

41. Carlson JW, Minemura T. Imaging time reduction through multiple receiver coil data acquisition and image reconstruction. Magn Reson Med 1993;29(5):681-687.

42. Sodickson DK, Manning WJ. Simultaneous acquisition of spatial harmonics (SMASH): fast imaging with radiofrequency coil arrays. Magn Reson Med 1997;38(4):591-603.

43. Kyriakos WE, Panych LP, Kacher DF, Westin CF, Bao SM, Mulkern RV, Jolesz FA. Sensitivity profiles from an array of coils for encoding and reconstruction in parallel (SPACE RIP). Magn Reson Med 2000;44(2):301-308.

44. Lauterbur PC. Image formation by induced local interactions: examples employing nuclear magnetic resonance. Nature 1973;242:190-191.

45. Enderle JD, Blanchard SM, Bronzino JD. Introduction to biomedical engineering. San Diego: Academic Press; 2000. 1062 p.

46. Haacke EM, Brown RW, Thompson MR, Venkatesan R. Magnetic resonance imaging : physical principles and sequence design. New York: J. Wiley & Sons; 1999. 914 p.

47. Cho ZH, Jones JP, Singh M. Foundations of medical imaging. New York: Wiley; 1993. 586 p.

48. Jin J-M. Electromagnetic analysis and design in magnetic resonance imaging. Boca Raton, FL: CRC Press; 1999. 282 p.

49. Liang Z-P, Lauterbur PC, IEEE Engineering in Medicine and Biology Society. Principles of magnetic resonance imaging : a signal processing perspective. New York: Wiley-IEEE Press; 1999. 416 p.

50. Kumar I, Welti D, Ernst R. NMR Fourier Zeugmatography. J Magn Reson 1975;18(69).

51. Edelstein WA, Hutchison JM, Johnson G, Redpath T. Spin warp NMR imaging and applications to human whole-body imaging. Phys Med Biol 1980;25(4):751-756.

52. Sodickson DK. Spatial encoding using multiple rf coils: SMASH imaging and parallel MRI. In: Young I, editor. Methods in biomedical magnetic resonance imaging and spectroscopy. Chichester: John Wiley & Sons Ltd; 2000. p 239-250.

53. Macovski A. Noise in MRI. Magn Reson Med 1996;36(3):494-497.

54. Sodickson DK, Griswold MA, Jakob PM, Edelman RR, Manning WJ. Signal-to-noise ratio and signal-to-noise efficiency in SMASH imaging. Magn Reson Med 1999;41(5):1009-1022.

55. Wang Y. Description of parallel imaging in MRI using multiple coils. Magn Reson Med 2000;44(3):495-499.

56.   Sodickson DK, McKenzie CA. A generalized approach to parallel magnetic resonance imaging. Med Phys 2001;28(8):1629-1643.

57.   Griswold MA, Jakob PM, Heidemann RM, Nittka M, Jellus V, Wang J, Kiefer B, Haase A. Generalized autocalibrating partially parallel acquisitions (GRAPPA). Magn Reson Med 2002;47(6):1202-1210.

58.   de Zwart JA, Ledden PJ, van Gelderen P, Bodurka J, Chu R, Duyn JH. Signal-to-noise ratio and parallel imaging performance of a 16-channel receive-only brain coil array at 3.0 Tesla. Magn Reson Med 2004;51(1):22-26.

59.   Porter JR, Wright SM, Reykowski A. A 16-element phased-array head coil. Magn Reson Med 1998;40(2):272-279.

60.   Brown DG, McDougall MP, Wright SM. Receiver design for parallel imaging with large arrays. In: Proc 10th Annual Meeting ISMRM, Honolulu, HI, 2002. p 863.

61.   Bankson JA, Wright SM. Simulation-based investigation of partially parallel imaging with a linear array at high accelerations. Magn Reson Med 2002;47(4):777-786.

62.   Reykowski A, Wright SM, Porter JR. Design of matching networks for low noise preamplifiers. Magn Reson Med 1995;33(6):848-852.

63.   Hyde JS, Froncisz W, Jesmanowicz A, Kneeland JB. Planar-pair local coils for high-resolution magnetic resonance imaging, particularly of the temporomandibular joint. Med Phys 1986;13(1):1-7.

64.   Hyde JS, Jesmanowicz A, Grist TM, Froncisz W, Kneeland JB. Quadrature detection surface coil. Magn Reson Med 1987;4(2):179-184.

65.   Lo YT, Wright SM, Navarro JA, Davidovitz M. Handbook of RF/microwave components and engineering, 2nd edition. Chang K, editor. New York: Wiley; 2003.

66.   Pruessmann KP, Weiger M, Wiesinger F, Boesiger P. An investigation into the role of coil coupling in parallel imaging. In: Proc 10th Annual Meeting ISMRM, Honolulu, HI, 2002. p 196.

67. McDougall MP, Wright SM, Brown DG. A 64-channel planar RF coil array for parallel imaging at 4.7 tesla. In: Proc 11th Annual Meeting ISMRM, Toronto, ON, Canada, 2003. p 472.

68. McDougall MP, Wright SM. A 64-channel array coil for Single Echo Acquisition (SEA) MRI. Magn Reson Med Submitted 2004.

69. Pozar DM. Microwave engineering. Reading, MA: Addison-Wesley Publishing Company; 1990. 726 p.

70. McDougall MP, Wright SM. Decoupling of planar-pair RF coil arrays using printed capacitance. In: Proc 11th Annual Meeting ISMRM, Toronto, ON, Canada, 2003. p 2374.

71. Jevtic J. Ladder Networks for capacitive decoupling in phased-array coils. In: Proc 9th Annual Meeting ISMRM, Glasgow, Scotland, UK, 2001. p 17.

72. Lee RF, Giaquinto RO, Hardy CJ. Coupling and decoupling theory and its application to the MRI phased array. Magn Reson Med 2002;48(1):203-213.

73. Jevtic J, Pikelja V, Menon A, Seeber D, Tatum N, Johnson W. Design guidelines for the capacitive decoupling networks. In: Proc 11th Annual Meeting ISMRM, Toronto, ON, Canada, 2003. p 428.

74. Wright SM, McDougall MP, Brown DG. Single echo acquisition of MR images using RF coil arrays. In: Proc 2nd Joint EMBS/BMES Conference, Houston, TX, 2002. p 1181-1182.

75. Wright SM, McDougall MP, Brown DG. Single Echo Acquisition (SEA) MR imaging. In: Proc 11th Annual Meeting ISMRM, Toronto, ON, Canada, 2003. p 23.

76. McGibney G, Smith MR, Nichols ST, Crawley A. Quantitative evaluation of several partial Fourier reconstruction algorithms used in MRI. Magn Reson Med 1993;30(1):51-59.

77. Jesmanowicz A, Froncisz W, Hyde JS. A complication in prescan strategy when using surface coils. Magn Reson Med 1987;5(4):318-322.

78.   McDougall MP, Wright SM. Coil phase compensation for Single Echo Acquisition (SEA) imaging. In: Proc 12th Annual Meeting ISMRM, Kyoto, Japan, 2004. p 330.

79.   McDougall MP, Wright SM. Overcoming phase effects of voxel-sized coils in planar and cylindrical arrays. In: Proc 26th Annual International Conference IEEE-EMBS, San Francisco, CA, 2004. p 1060.

80.   Blackband SJ, Bui JD, Buckley DL, Zelles T, Plant HD, Inglis BA, Phillips MI. MR microscopy of perfused brain slices. Magn Reson Med 1997;38(6):1012-1015.

81.   Shepherd TM, Thelwall PE, Blackband SJ, Pike BR, Hayes RL, Wirth ED, 3rd. Diffusion magnetic resonance imaging study of a rat hippocampal slice model for acute brain injury. J Cereb Blood Flow Metab 2003;23(12):1461-1470.

82.   Song HK, Wehrli FW, Ma J. In vivo MR microscopy of the human skin. Magn Reson Med 1997;37(2):185-191.

83.   Ozeki T, Kose K, Haishi T, Hashimoto S, Nakatsubo S, Nishimura K. Three-dimensional snow images by MR microscopy. Magn Reson Imaging 2003;21(3-4):351-354.

84.   Mirrashed F, Sharp JC. In vivo morphological characterisation of skin by MRI micro-imaging methods. Skin Res Technol 2004;10(3):149-160.

85.   Bock NA, Konyer NB, Henkelman RM. Multiple-mouse MRI. Magn Reson Med 2003;49(1):158-167.

86.   McDougall MP, Wright SM, Brown DG. A low-pass trombone birdcage coil with broad tuning range. In: Proc 9th Annual Meeting ISMRM, Glasgow, Scotland, UK, 2001. p 1092.

87.   Wright SM, McDougall MP, Brown DG, Hazle JD. Arrays of birdcage coils for imaging multiple samples. In: Proc 9th Annual Meeting ISMRM, Glasgow, Scotland, UK, 2001. p 18.

88.   Riederer SJ, Tasciyan T, Farzaneh F, Lee JN, Wright RC, Herfkens RJ. MR fluoroscopy: technical feasibility. Magn Reson Med 1988;8(1):1-15.

89. van Vaals JJ, Brummer ME, Dixon WT, Tuithof HH, Engels H, Nelson RC, Gerety BM, Chezmar JL, den Boer JA. "Keyhole" method for accelerating imaging of contrast agent uptake. J Magn Reson Imaging 1993;3(4):671-675.

90. Wright SM, McDougall MP. Resolution enhancement in Single Echo Acquisition (SEA) MR imaging. In: Proc 11th Annual Meeting ISMRM, Toronto, ON, Canada, 2003. p 2493.

91. Ciobanu L, Seeber DA, Pennington CH. 3D MR microscopy with resolution 3.7 microm by 3.3 microm by 3.3 microm. J Magn Reson 2002;158(1-2):178-182.

92. Song HK, Wehrli FW. Variable TE gradient and spin echo sequences for in vivo MR microscopy of short T2 species. Magn Reson Med 1998;39(2):251-258.

93. Wright SM, Brown DG, McDougall MP; The Texas A&M University System, assignee. Magnetic Resonance Imaging Using a Reduced Number of Echo Acquisitions. United States patent US 6,771,071 B1. 2004 Aug.3,2004.

94. Wright SM, McDougall MP. Single Echo Acquisition (SEA) imaging at 125 frames per second. In: Proc 12th Annual Meeting ISMRM, Kyoto, Japan, 2004. p 533.

VITA

Mary Preston McDougall was born in New Orleans, Louisiana on October 22, 1974 to Bob and Margaret Preston. She graduated magna cum laude from Texas A&M University in May 1997 with her Bachelor of Science in Electrical Engineering. She received a National Science Foundation Graduate Research Fellowship and continued to Johns Hopkins University for graduate work. She graduated in May 1999 with her Master of Science in Engineering in Electrical and Computer Engineering from Johns Hopkins University, and returned to Texas A&M University for her doctoral studies. At present, she is concluding her doctoral research, with an expected graduation date of December 2004. She currently resides with her husband and five children in College Station, Texas. She expects to continue her work in academia, with research interests focused on magnetic resonance imaging technology and applications.

For further information, the author can be contacted at the address below:

5947 Vanderbilt
Dallas, TX 75206
Office Phone: 979-458-1146